Escola de Camins
Escola Tècnica Superior d'Enginyeria de Camins, Canals i Ports
UPC BARCELONATECH

TREBALL FINAL DE MÀSTER

Computational models of mammalian brains in transient dynamics.

Treball realitzat per:
Carles Duñó Nosas

Dirigit per:
Pablo Saez Viñas

Màster en:
Mètodes Numèrics en Enginyeria

Barcelona, 11 maig 2018

Departament d'Enginyeria Civil i Ambiental

Acknowledgements

First of all, I would like to thank Folco C. Georgios V. and Martin L. who enabled me to investigate in this topic in such a prestigious center as the JRC Ispra in Italy that allowed me to gather lots of nice memories.

I would like to express my sincere gratitude to my advisor Dr. Pablo Saez Viñas for always supporting me.

I thank my fellow labmates in LaCáN for aiding me whenever necessary, for all the dinners and coffeebreaks together and for all the fun we had in this brief experience.

And last but not least, I would like to thank my parents and brother for encouraging me during all the master.

Contents

Abstract

To date, the brain remains the most intriguing and unexplored organ in mammals. Although the vast majority of research is focused on understanding the way the brain functions at different cognitive scales, an accurate characterization of the mechanical behavior is fundamental for analyzing it. That is because even if mechanical stimuli has small relevance under physiological conditions, mechanics do have importance in pathological settings including brain deformation or swelling, such as brain injury or tumor and can be useful as well with brain surgery.

The objective of this thesis is to model the mammalian brain in fast transient dynamics, impact or blast, and to analyze the effect of size, shape boundary conditions and material.

keywords *Finite element method, Biomechanics, Hyperelastic modeling, Dynamics.*

Chapter 1

Introduction

The brain has been one of the subjects of extensive investigation over the last decades. It is often considered the most vulnerable part of the body, meaning that the injuries to it have severe consequences or are even life-threatening. Understanding its mechanical behavior is crucial for the study of brain diseases involving deformation or swelling such as brain tumor, strokes, or the phenomena of Traumatic Brain Injury (TBI).

To develop preventive strategies for these injuries, or to provide doctors with valuable information for the fast and accurate diagnosis of damage, the Finite Element (FE) simulations are unique tools to evaluate injury mechanisms and provide a better understanding of the mechanics. Thus accelerating the development of both protective, diagnostic, and treatment strategies [27].

Therefore, the FE modeling has been used through the decades to asses the bio-mechanics of the head injury mechanism, proving to be a cost-effective alternative to experimental techniques in living animals in estimating the internal bio-mechanical responses. For the correct function of these computational tools, well calibrated and validated mathematical models of bio-mechanics and neurobiology are crucial, which should be complemented with *in vitro* and *in vivo* experiments.

Modeling the brain tissue is a big challenge by itself; proof of it is that the scientific community has not reached a general consensus on how to model it for the last three decades. This is due to the high complexity of the brain. It is not only made by multiple structures marked by different mechanical properties, but also because the response varies depending on which level is considered, the macroscopic level (organ), mesoscopic (tissue), microscopic (cell) and the nanoscopic (molecule) ones [57]. Understanding the correlation between the internal structure of the tissue and its macroscopic mechanical properties is therefore important, especially because loads applied to the brain turn into stresses and strains depending on the local morphology and composition. For that, a complete and accurate picture of the mechanical properties of the brain is needed.

With all those complexities, the damage or probability of injury cannot be predicted with only the typical stress strain rate criterion. Even more, the relation between the mechanical strain and cells death is much more complex than it might be thought.

This study is focused on the dynamic behavior and on the analysis of deformations, stretches, strains, strain rates, pressures and stresses; these variables play a crucial role in modulating both brain form and function. We also analyze the effect of size, shape, boundary conditions or material on the mammalian brain. We will not focus on the electro-chemical interactions, or in slow motions as the tumor growing in the brain, which are the main focuses of most of the current research efforts.

The prototype example of the pathologies studied is the Traumatic Brain Injury TBI: a complex injury associated with a broad spectrum of symptoms and disabilities caused by an external mechanical stimulus to the head, such as a high acceleration, an impact or a shock-wave (blast). The effect of this pathology embraces a local damage of the brain tissue to a widespread axonal injury [67, 68].

One of the most common and complex pathological features of the TBI is the Diffuse Axonal Injury (DAI). It occurs in the white matter of brain at a cellular level which is not visible with conventional medical imaging modalities, making it difficult to diagnose especially in the first stages.

Traumatic Brain Injury remains as a leading cause of death and disability all over the world. Specifically 1.7 million people sustain a TBI annually only in the United States, representing one-third of all motor vehicle related deaths. It is also accounted to be the cause of death for approximately 40% of the road fatalities of the European Union. Also the blast-induced TBI (bTBI) is one of the most common injuries seen in the US military personnel returning from Irak or Afghanistan. Even if it is hard to calculate, the bTBI has been estimated to be as high as 18% among all US combat veterans [4]. The bTBI analysis can be used not only for military purposes, but also for risk assessment or damage prevention on soft targets (undefended citizens or structures) in societies vulnerable to blast terror attacks.

Computational models can help detecting the damage in a smaller area, and also understanding the level of lethality. Even more importantly, since in some cases the symptoms can appear days or even weeks after the affection, the simulation can reveal if some damage not seen in the preliminary tests is to be expected, in case the symptoms are yet to appear.

1.1 Motivation

This project, realized in collaboration with the European Commission - Joint Research Center (JRC), aims to create a valid mechanical model for the brain under dynamic loads, in order to assist head injury, which is one of the causes of death or permanent disability in everyday life and continues to remain as a major health problem. In this document we study the brain under extreme loading conditions such as blast waves or impacts.

The use of mathematical modeling tools may reduce the need of trial and error tests involving laboratory animals, and yet provide a capability to study brain injury mechanisms, accelerating the development of neuroprotective strategies.

Blast terror attacks have been increasing in number in recent years, remember for example the ones in Madrid, London and Moscow. Normally they focus on the unarmored and undefended targets (soft targets) [41] resulting in explosions on urban terrain.

On blast wave events three potential insults are classified as depicted in figure 1.1.1: primary blast insult due to the shock wave, secondary blast insult due to debris fragments, and tertiary blast insult due to human body translation by blast load and resulting on a impact on rigid objects. In this project we focus on the events that do not imply penetration of the human body, meaning the first and the third blast insults.

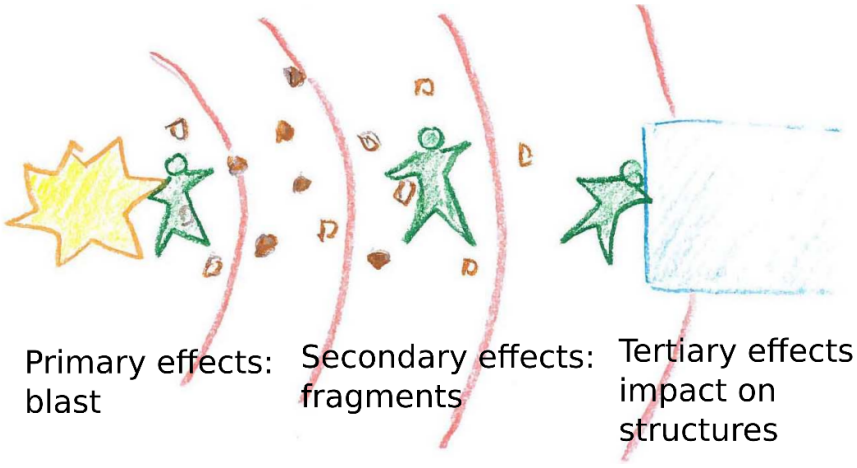

Figure 1.1.1: Types of blast insults to the human body.

Nowadays some empirical formulas for the risk evaluation already exist [35, 17, 40]. But such direct estimation, which does not take into account the effects in confined spaces, must be ameliorated. As presented by Leibovici et al. [36], detonations inside confined structures have a higher mortality rate than in open-air.

A Finite Element model will be developed in order to correlate the second and third reflected blast waves in confined spaces, enabling to perform realistic risk assessment on fast transient dynamics.

1.2 Anatomy of a mammal head

A general knowledge of the anatomy and physiology of the head is helpful in understanding the functioning and the natural protective mechanisms of the brain.

Brain is the body control center, including automatic reflects as well as sensory perception and motor function. Different tissue layers such as the skull bone and the Cerebrospinal fluid (CSF), cover the brain as depicted in figure 1.2.1. .

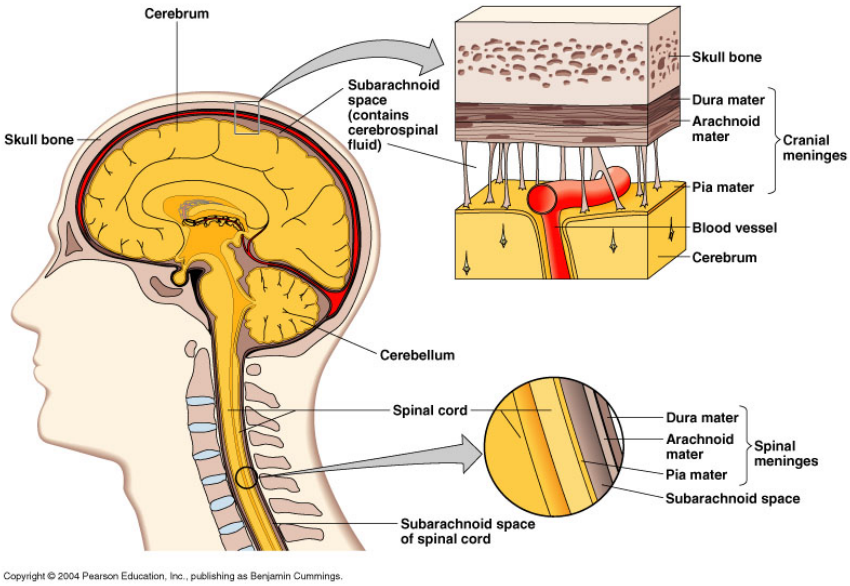

Figure 1.2.1: Layers in the human head

First of all, there is the **skull** that provides a hard protective shell around the brain. It can be viewed as a three-layered sandwich structure, with an inner and outer table of compact bone and a dipole of spongy bone sandwiched between them as a core. The skull is formed by a bone network molded and fitted to brain, eyes, ears, nose and teeth. The base of the braincase is an irregular plate of bone containing depressions and ridges plus small holes (foramen) for arteries, veins, and nerves, as well as the large hole (the foramen magnum) that is the transition area between the spinal cord and the brainstem.

Next, with the function of softening the interface between the brain and the skull, and confining the central nervous system, there are three membranes that envelop the brain and spinal cord. In mammals, the **meninges** are composed of three layers as seen in figure 1.2.1: the dura mater, the arachnoid, and the pia mater.

The *dura mater* is a thick membrane, attached to the skull that envelops the arachnoid mater and surrounds the large dural sinuses carrying blood from the brain towards the head.

The middle element of the meninges is the *arachnoid mater*, so named because of its spider web-like appearance. It cushions the central nervous system. This thin,

and transparent membrane is composed of fibrous tissue and is covered by flat cells thought to be impermeable to fluid.

The *pia mater* is a very delicate membrane. It is the meningeal envelope that firmly adheres to the surface of the brain and spinal cord, following all of the brain contours. It is a very thin membrane composed of fibrous tissue covered on its outer surface by a sheet of flat cells also thought to be impermeable to fluid. The pia mater is pierced by blood vessels directed to the brain and spinal cord, and its capillaries nourish the brain.

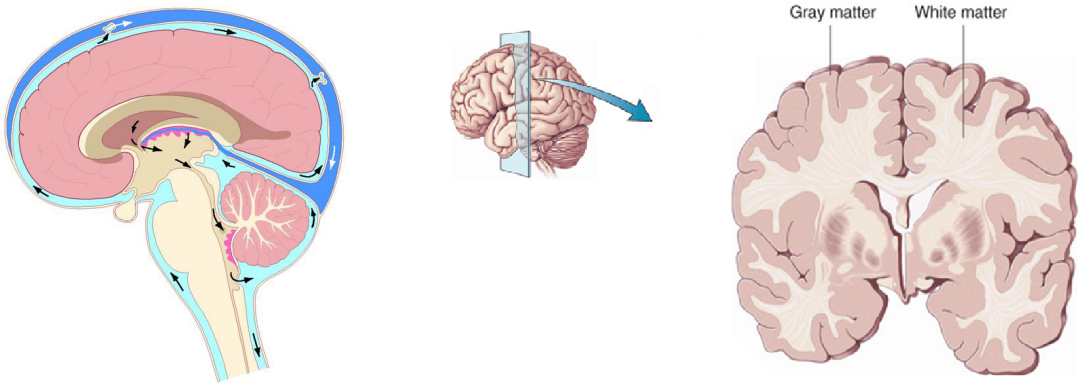

(a) Circulation of CSF on the head.

(b) White and gray matter.

Figure 1.2.2: Generic groups of the mammals head.

The **Cerebrospinal fluid (CSF)** is a clear, colorless body fluid found in the brain and spinal cord, which acts as a cushion or buffer for the brain against impacts with the wall of the skull during everyday head movements, providing basic mechanical and immunological protection. At the same time it serves a vital function in cerebral auto-regulation of blood flow.

The CSF occupies the sub-arachnoid space, between the arachnoid and the pia mater as can be seen in figure 1.2.2a. It fills the ventricles of the brain, as well as the central canal of the spinal cord.

The **Brain** is located within the skull surrounded by the cerebro-spinal fluid (CSF), which allows the relative motion between them. It is the organ that serves as the center of the nervous system in all vertebrate and most invertebrate animals, being the most complex organ in a vertebrate body, having the same texture and consistency as gelatin. In a human, it contains over 83 billion nerve cells called neurons, it fills 40% of the head volume and consumes the 94% of the oxygen.

Visually, the interior of the brain consists of an outer layer of the so-called gray matter, being the major component of the central nervous system, and an inner core of white matter as depicted in figure 1.2.2b.

The *gray matter* is composed of dendrites with short unmyelited axons, consisting mainly of areas with high densities of neuron cell bodies. The real processing of information is done in the gray matter. Without having myelined axons, the neurons of the gray matter do not prolong themselves long.

The *white matter* is a web of neurons that is formed by an organized arrangement of neural axons wrapped in a fatty insulating sheath of myelin, which serves to greatly increase the speed of signal propagation. It compounds different structures of the brain as the thalamus or the hypothalamus. It serves the function of communicating or wiring from and to the gray matter, and from the gray matter to other parts of the body. It also governs body functions, as temperature, arterial pressure, and cardiac frequency. The release of hormones and the automatic reflexes to emotions are added functions of the white matter.

1.2.1 Scalability between species

Most of the animal *in vivo* experiments are performed on rodents, this is because there are many advantages to it such as the cost-effectiveness, logistical convenience (eg. housing, handling, transportation), comparability of results across different forms of damage and the existing neurobehavioral tests tailored to rodents [34]. Furthermore there is availability of genetically modified animals that enables the study of the role specific genes in the TBI [62].

However, using rodent brains for the study of TBI has also some disadvantages regarding the usefulness of the results due to the obvious differences between the rodent and human brain [63]. Those characteristics are not only related to the brain size or the maturation, but also on the organization of it. The rodent brain has a lissencephalic, or smooth surface of the brain typical of small mammals, while the human has a gyrencephalic, or convoluted surface of the brain shared with other big mammals like the Porcine, Bovine or other Primates. This organization is important since there is evidence that blast waves and impacts interact differently with gyrencephalic than in lissencephalic brains [63] [2].

The differences in size, organization and maturation between rat and human brain affect its biomechanical response, making the conclusions from rats experiments hard or impossible to scale to human brain. The reason is that a significant change in large areas of the lissencephalic rodent brain may only translate into small effects in the gyrencephalic human, or vice versa [55, 39].

1.3 Clinical Effects

1.3.1 Damage at cell level

As the brain and its cells are so fragile, sudden rapid movements of the head can cause injuries. One of those injuries, called coup-contra-coup or acceleration-deceleration injury, makes the brain bounce back and forth the bonny interior wall of the skull. As the brain moves, it cruises against the inside of the skull sending stress waves through the brain. This stress-waves stretch or can even tear the axons of some neurons, which causes a trauma called Axonal Shearing or Diffusive Axonal Injury (DAI).

Effects of mild - moderate DAI covers a big spectrum of symptoms depending on the area of the brain injured including loss of consciousness, impaired long term memory, reducing problem solving abilities and problems with attention and perception. If we take into account the severe cases of DAI, the effects could be as serious as the comma or the persistent vegetative state.

Brain damage can continue to occur for hours or days after the initial injury damage to the axons, that can lead to a breakdown of communication among neurons on the brain. The thorn axons quickly degenerate releasing toxic levels of chemicals into the extracellular space, and at the end many of the surrounding neurons begin to die over the next 24 - 48 hours worsening the initial effects of the injury.

After a mild Injury, where most of the axons have been stretched but not thorn, the cell will start slowly to recover (7-10 days) trying to regain balance, while in this state the cell does not have enough energy for the correct function. Meanwhile the damaged axon structure impedes the neurotransmission having a heightened vulnerability to more damage, before the complete recovery of the cell means the problems are exacerbated, the axon damage worsens and neurotransmission is further hindered and the recovery length is extended.

1.3.2 Threats of Blast waves

After an artifact explodes, the effects of it can be decoupled into some sequential phases. The start of all is the detonation, which is a rapid chemical reaction that releases energy and generates high pressures and temperatures. The expansion of gases after detonation compresses the surrounding air into a pressure wave, shock that propagates at supersonic speed in all directions. But in confined spaces, when some reflective surfaces such as walls appears, it produces second or third reflected waves and highly complex time history pressure patterns.

When blast waves encounter objects with higher density such as the human body, they reflect from it, diffract around it, and pass through it as elastic and shear waves. Furthermore, in confined spaces were reflected waves could come from various directions and taking into account that each successive trauma exacerbates the damage (section 1.3.1), the blast injuries may be more serious. On the primary insult there are several paths for the energy to enter the brain [27],

- Skull micro deformation or vibration, creates a stress wave within the brain.
- Movement or Rotation of the head causes compression/traction/shear waves within the brain.
- Pressure wave entering directly via various foramens (ocular, ears, foramen magnum, or vascular foramina).
- Elastic wave propagation along the blood vessels propagated from the torax.

The primary cause of damage of biological structures is the sudden increase of pressure followed by a similar rapid decrease of it. These energy waves behave differently with quasi-incompressible fluids like CSF of blood than for soft viscous materials like the brain. Therefore it is important to model the brain and its parts accurately.

1.4 Brain Mechanics

Problems including deformation of soft tissues are among the most challenging in applied mechanics, and not only because they undergo large strains, but also because they exhibit nonlinear time dependent behavior similar to the viscoelastic materials [21]. Moreover, biological tissues are not simple passive materials like the concrete, steel, etc, but rather they actually contract, grow and self-repair.

In biomechanics it is complicated to get the constitutive relations that link deformation and stress because of the nonlinearity, the complex geometries, and the composite nature of the biological tissues. Together with the previous, determining an effective constitutive relation that describes the behavior of the soft tissues, remains a subject of intensive research even nowadays. In order to get these relations, two different ways can be considered: the micro-structural and the phenomenological approaches.

In the micro-structural approach, the geometric and mechanical properties of individual tissue components are measured directly. Then a macroscopic constitutive relation for the composite tissue is derived from it. Having huge advantages in the final model, this approach has faced a limited success until today, as judged by the predicted response in comparison to experimental measurements.

In the phenomenological approach, the macroscopic constitutive equations are determined directly by fitting experimentally measured stress-strain curves. This usually involves postulating a functional form and determine the parameters while minimizing the error between the measured and the computed data. This approach is mathematically simple but does not take into consideration micro-structure.

Due to its simplicity and because of its consistency with the experimental data, the phenomenological approach will be taken from here on.

In this document several nonlinearities are considered. The *Material nonlinearity* which appears due to the nonlinear stress-strain relationship of soft tissue, given by the empiric curve, and the *Geometrical nonlinearity* which accounts for geometric nonlinearities that occur in models with large displacements or rotations, large strain, or a combination of them.

Chapter 2

Mechanical behavior of the head

Even with multiple and different geometries of the heads in the scope of the project (Rat, monkey and human) all of them havee the same main structures and therefore it will be treated in exactly the same way.

2.1 Skull

First of all, protecting the brain there is the skull, a hard layer which thickness can vari depending on the individual. This layer will only be implemented in the blast loading condition, since while modeling the impact a displacement will be imposed in the exterior part of the CSF.

During the blast loading condition, where a pressure will be imposed on the exterior this hard layer distributes the external pressure field to the soft hyper-elastic brain tissue. The modeling of the skull has been long studied and agreed that behaves like a linear elastic material. The treatment of the skull is a bit different between studies, some like [12, 26, 33] consider that it is necessary to separate the outer and inner bones from the dipole, while other studies just take a value for the whole layer [10].

For the sake of simplicity, the second approach is taken using a uniform layer with a single value of elastic modulus, Poisson and density as displayed on table 2.4.1.

2.2 Brain

Regarding the material parameters, the brain matter changes all its properties as we switch the area we are looking. Also it is known that there exist some changes on experimenting on different animals.

In this document, even knowing all this variety on the brains, a unique set of material parameters will be considered. The reason for this is mainly because the meshes we have does not have discretized all the parts also, and due to the lack of information in the bibliography for all parts of the brain, for all animals and also for a considerable set of strain rates.

2.2.1 Hyper-elasticity

For many materials, linear elastic models are not appropriate for accurately describe biological tissues, in those cases a large deformation hyperelastic model, must be taken into account. This type of materials result especially useful when the difference between the deformed and undeformed shapes is large enough that they cannot be treated the same, and when the relation between stress and strain becomes nonlinear as deformation increases (see figure 2.2.1).

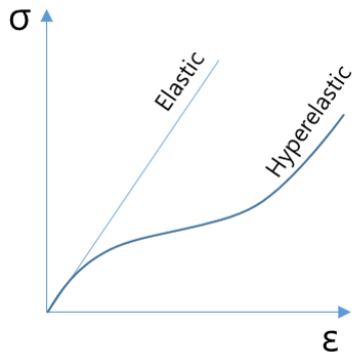

Figure 2.2.1: Hyperelastic material

Those models assume that the material behavior can be described through a strain energy density function Ψ, from which the stress-strain relationships can be derived. In the finite strain range, such theories are particularly appropriate for the analysis of rubber-like solids, which in many cases show excellent agreement with experiments involving strains over 700% depending on the specific hyperelastic model used [19].

It should be pointed that the load-deformation/stress-strain curve of brain tissue deviate significantly from the behavior of other biological tissues. For instance, the brain tissue is unique since it shows a completely nonlinear load-deformation curve without any linear parts [29].

Recent experimental evidence [46] shows that biological tissues such as the brain, liver, fat, etc. have some unusual mechanical properties, that the constitutive equations must be able to reproduce, and for instance the Neo-Hookean, Fung, or Gent models do not satisfy. For this document and in accordance with the bibliography [61] the Mooney-Rivlin and Ogden hyperelastic material models will be used in this document comparing its functionality.

The most used method to get the hyperelastic parameters is by means of fitting the computational stress-strain curve to the experimental. And so, there is a lot of information for this in the literature [23, 18, 11], but the paper from Pervin [54] is the selected one for this thesis because it shows the great impact of the strain rate effect depicting a curve for all of them. This is important since it allows us to choose freely the material that is best suit to the impact experiment an also for the explosion. And as we said before the hypothesis that there is no significant difference in the parameters across animals is taken, since a bovine animal is used in order to get the curves.

2.2.2 Viscoelasticity

Being part of the brain material characterization, there is no accordance in which viscoelastic method or parameters to use, and the behavior varies in the brain as we switch areas. For this reasons, this part will study the effects of three different sets of parameters given in the bibliography.

Table 2.2.1: Viscoelastic parameters of the brain matter.

Materials	g_i	k_i	τ_i
Kleiven [33]	0.7685	0.0	1.E-6
"visc1"	0.1856	0.0	1.E-5
	0.0148	0.0	1.E-4
	0.019	0.0	1.E-3
	0.0026	0.0	1.E-2
	0.007	0.0	1.E-1
Garimella et al. [22]	0.65425	0.0	0.006694
"visc2"	0.0149	0.0	0.15642
makoshi et al. [38]	0.6313	0.0	0.0012
"visc3"	0.1607	0.0	0.16
	0.0988	0.0	2.75

2.3 Cerebrospinal fluid

The CSF has been one of the most problematic points in how to model the head due to different factors. First, being that as its name says is a fluid so it should be treated as such.

Most of the FEM models in the bibliography treat the CSF as a solid with fluid properties allowing a contact with slip interfaces between the CSF, skull, and brain. This hypothesis is invalid for larger deformations or for large periods of time [27].

2.3.1 Mie-Grüneisen

To implement an hydrodynamic material which would take into account this different effects. Being used a lot in the bibliography the equation of state Mie-Grüneisen is chosen [22, 12], which was written in a new subroutine from scratch in the software EUROPLEXUS.

$$p = \frac{\rho_0 C_0^2 \chi}{(1 - s\chi)^2} + (\Gamma_0 E) \quad with \qquad \chi := 1 - \frac{\rho_0}{\rho} = 1 - \frac{V}{V_0} \tag{2.3.1}$$

where p is the absolute pressure, ρ_0 the initial density, ρ the current density, V the current volume, V_0 the initial volume, E the internal energy per unit volume, s and Γ_0 are dimensionless parameters. Values that are assumed to be water-like and taken directly from the literature [22]

Once implementing this material a problem surged, being that in the Mie-Grüneisen, the velocity of propagation of the sound in the material was too high. This reduces the time step by one order of magnitude, making the computation much slower.

2.3.2 Elastic solid

Another approach of the treatment of the CSF is to model a solid. For this, a linear an a nonlinear elastic material strategies will be tested checking the affections of the CSF modeling into the brain material, approximations also found in the literature [6, 7, 12, 65].

In this case for the elastic approximations two sets of linear parameters will be taken from [65]. For the nonlinear elastic, the same material is used but with a higher bulk modulus, making it less compressible.

2.3.3 Material parameters

Once defined the material models that will be used, the values to the parameters have to be obtained. For this most of the data is obtained through different papers [38, 65, 27].

For the CSF three different materials are analyzed, the fist of them is the more simple and the oldest used in the bibliography that is modeling this confined fluid as an almost incompressible linear elastic material [65]. The second one is the consideration of the CSF as a soft and also incompressible hyper-elastic solid strategy also used in the literature [66]. And the last discretization is the Mie-Grüneisen equation of state (MIEG), known to be the one with the more accurate behavior in fast dynamics, equation explained in section 2.3.1 and the parameters used are those from watter [22] summarized in table 2.3.1.

In the case where the Mie-Grüneisen equation of state is used, since the transmission between the CSF and the brain is too sudden that the brain mesh is highly deformed, the pia matter (see section 2.4) is modeled to act as a protector layer.

2.4 Meninges

During the modeling of the CSF as a fluid, the problem arises that the Lagrangian fluid material deforms too much in the contact of the soft hyperelastic matter. In order to solve this issue, the intermediate layer between the CSF and the brain is introduced, the Pia-matter. This layer is considered a hard tissue and modeled as a linear elastic material as the brain. Its parameters are extracted from the literature [26, 33], table 2.4.1.

Table 2.3.1: Parameters of all the models considered for the CSF in impact regime.

Materials	*Velocity of sound*$[m/s]$	*Parameter* S[-]	*Parameter* Γ_0[-]	viscosity η [-]
CSF-MIEG-vis	1489	1.79	1.65	0.001
CSF-MIEG	1489	1.79	1.65	
	$C_{10}[Pa]$	C_{20} $[Pa]$	$D_1[Pa^{-1}]$	
CSF-Hype	860.0	816.75	0.0	
	$E[Pa]$	$\nu[-]$		
CSF-lin1	2.19E+6	0.489		
CSF-lin2	10	0.499		

Table 2.3.2: Parameters of all the models considered for the CSF in blast regime.

Materials	α_1 [-]	α_2[-]	α_3[-]	$\mu_1[Pa]$	$\mu_2[Pa]$	$\mu_3[Pa]$	$K[Pa]$
Gray matter	-8.79	11.0	-	586.94	29868.0	-	1.025E+6
White Matter	8.10	8.85	8.10	3.16E+3	40.50E+3	33.80E+3	1.0E+6
	Velocity of sound$[m/s]$			*Parameter* S[-]		*Parameter* Γ_0[-]	
CSF-MIEG	1489			1.79		1.65	

Table 2.4.1: Material parameters of the linear elastic materials

	$\rho[kg/m^3]$	$E[MPa]$	$\nu[-]$
Skull	1800	1500	0.21
Pia-matter	1130	11,5	0.45

Chapter 3

Methods

3.1 Balance equations

The governing equation used for a structural domain is the conservation of momentum, (i.e. equilibrium in a dynamic sense)

$$\int_V \rho \underline{\ddot{x}} \delta \underline{x} + \int_V \underline{\sigma} D(d\underline{x}) dV - \int_V \rho \underline{f} \delta \underline{x} dV - \int_{S_1} \underline{t} \delta \underline{x} dS = 0 \tag{3.1.1}$$

3.1.1 Analysis type

The analysis of this document will be carried in transient dynamics regime with geometric non-linearity. To treat this phenomena a decision must be made on which type of analysis (Implicit or Explicit) has to be carried.

Each analysis type has its own advantages and drawbacks. For a dynamic analysis, the following general governing equation is used:

$$M\mathbf{a} + C\mathbf{v} + K\mathbf{d} = f^{ext} \tag{3.1.2}$$

where the primes indicate a time differential, M, D and K are the mass, damping, and stiffness matrices, respectively, f_{ext} is the vector of externally applied loads, and $\mathbf{d}$, $\mathbf{v}$ and $\mathbf{a}$ are the displacement, velocity, and acceleration vectors of the discrete nodes on the structure [13]. Making one of the first differences that the implicit method solves for the displacement vector $\mathbf{d}$ and the explicit solves for the accelerations $\{\mathbf{a}\}$.

The implicit method, as said above uses the Euler Time Integration to solve for $\mathbf{d}$ vector, and in order to do so the inverse of the stiffness matrix needs to be calculated, and the calculation of the inverse is a computationally intensive step, especially in non linear problems where the same stiffness matrix will become a function of $\mathbf{d}$. In return, this method is *unconditionally stable*, which means that does not matter which time increment it takes, the solution will always be stable.

On the other hand, the Explicit method instead of solving for **d** it solves for **a**, meaning that the inversion of the stiffness matrix is not needed, and only the Mass matrix which usually is a diagonal matrix has to be inverted, calculation that is easily done. But, since it does not use the Euler Time integration the method is only *conditionally stable*, which means that the time steps must be smaller than the Courant time step (the time it takes a sound wave to travel across an element).

Another factor that must be taken into account is how the nonlinearities are treated in each method, which as we said in the previous paragraph, in the Implicit method the inversion of the stiffness matrix is more difficult making each step more expensive. Also, in this method the solution of each step requires series of trial solutions (iterations) to establish equilibrium within a certain tolerance. In explicit analysis, no iteration is required as the nodal accelerations are solved directly.

Which means that explicit analysis handles nonlinearities with relative ease as compared to implicit analysis. This would include treatment of contact and material nonlinearities.

With all that some conclusions can be extracted,

Explicit Method

- Easier to consider nonlinearities
- No iterations needed
- Faster steps
- Limitations with time step (conditional stability)

Implicit Method

- Nonlinearities more difficult to include
- Iterations (possible convergence issues)
- Steps more expensive
- Can use larger steps

In the explosion or blast regime, since it is a high speed dynamic problem, the solution time is comparable to the time required for the wave to propagate through the structure. For this cases, the number of steps required with the explicit method is not excessive. If the Implicit method uses a similar time step it will be be much slower and if it were to use a much larger time step it would introduce other solution errors since it would not be capturing the pertinent features of the solution (even if it remains stable). Hence, the explicit method is the optimal choice.

For the case of the impact, which cannot be classified as either high-speed dynamic or low speed (solution spans a period of time considerably longer than the time it takes the wave to propagate through the element), both solution methods are comparable.

The analysis types in our case can be summarized as depicted in figure 3.1.1. And since the duration of the considered impact is short enough the Explicit Time Integration will be used.

3.1.2 Explicit Time Integration

Once determined the analysis type that will be carried, it is useful to recall the governing equations at the base of the transient explicit formulation. As explained in section 2 only the Lagrangian description will be used, which is suitable for the treatment of purely structural applications.

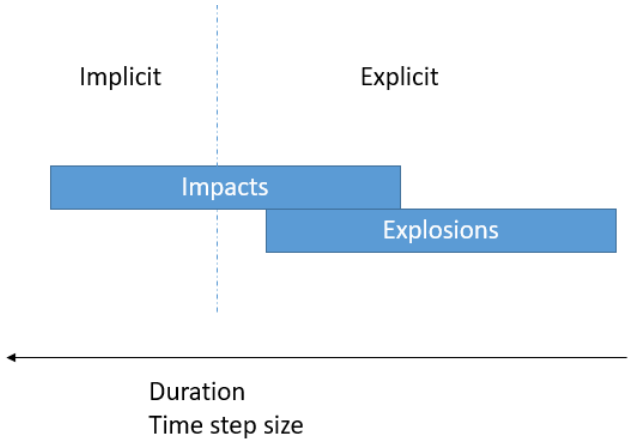

Figure 3.1.1: Summary of the determination of the problem type.

Explicit finite element (FE) codes have been developed, validated and used over more than three decades to model fast transient dynamic phenomena, ranging from explosions to impacts and to crashes. They are now routinely applied for simulations in such broad areas as nuclear safety, transportation, pipelines, marine and offshore, to name just a few.

3.1.2.1 Central Difference scheme

Time integration of 3.1.2 is achieved via the so-called Central Difference (CD) scheme. In this method the acceleration and velocity are approximated in terms of the displacements using the finite different expression and substituted in the equation of motion to solve for the displacement at that time step. Thus, it can be seen that the solution at time $n+1$ is determined from the solution at time n without using the equation of motion at time $n+1$. In particular, the elastic and damping forces can be determined explicitly using known displacements and velocities.

$$\begin{aligned} \mathbf{v}^{n+1} &= \mathbf{v}^n + (\Delta t/2)(\mathbf{a}^n + \mathbf{a}^{n+1}) \\ \mathbf{d}^{n+1} &= \mathbf{d}^n + \Delta t[\mathbf{v}^n + (\Delta t/2)\mathbf{a}^n] \end{aligned} \tag{3.1.3}$$

where $\mathbf{v}$ are the nodal velocities, $\mathbf{d}$ are the nodal displacements, the upper suffix n denotes a quantity at time t^n and $n+1$ denotes a quantity at time $t^{n+1} = t^n + \Delta t$, Δt being the time increment or time step used in the discretization process.

The time integration scheme 3.1.3 is implemented as follows in a typical explicit code. We want ultimately the acceleration in terms of displacements at time steps n and $n+1$, therefore first, an intermediate velocity at mid-step is introduced at time step $n+1/2$ using central difference expressions and then displacements at these steps.

$$\mathbf{v}^{n+1/2} = \mathbf{v}^n + (\Delta t/2)\mathbf{a}^n \tag{3.1.4}$$

This is the constant velocity that would transform configuration n into $n+1$ over a time interval t. In fact, from the second of 3.1.3 the new displacements are given by

$$\mathbf{d}^{n+1} = \mathbf{d}^n + \Delta t \mathbf{v}^{n+1/2} \tag{3.1.5}$$

On the new configuration induced by these displacements

$$\mathbf{x}^{n+1} = \mathbf{x}^n + \Delta t \mathbf{v}^{n+1/2} = \mathbf{x}^0 + \mathbf{d}^{n+1} \tag{3.1.6}$$

3.1.2.2 Numerical stability

The main counterpart of the explicit methods is that the CD scheme is only conditionally stable. For this the well-known Courant-Friedrichs-Levy (CFL) stability condition must be satisfied as a severe restriction on the time step size.

$$\Delta t \leq \Delta t^{crit} \tag{3.1.7}$$

where Δt^{crit} is the critical value of the time increment, beyond which the scheme is numerically unstable. The value of Δt^{crit} for each element in the mesh may be estimated according to the following relation

$$\Delta t_i^{crit} \approx (\Delta L_i)/c_i \tag{3.1.8}$$

where ΔL_i is the minimum distance among the nodes of the element and c_i is the speed of sound in the material. Meaning that Δt^{crit} is the time needed for a stress wave to traverse the element. Since the estimation of c_i is always an approximation, a stability safety factor (security coefficient) $0 < C_s \leq 1$ is used for prudence to somewhat reduce the time increment, which typical range is between 0.5 and 0.8.

$$\Delta t = C_s \Delta t^{crit} \tag{3.1.9}$$

3.1.2.3 Physical meaning of the stability limit

As it is well known, the status of the modeled system and its evolution is ruled by the wave propagation phenomena, stress waves in solids or pressure waves in fluids, meaning that if an external load is suddenly applied at one end of a bar, its effects are "transported" element by element at each time step following the pressure wave, thats why the Δt cannot be greater than the Δt^{crit}, because between one time step and the following the stress wave would skip elements. Which is a great difference respect to the implicit method that imposes equilibrium in the system, that makes that the effects of any sudden applied load is instantly felt for the rest of the structure.

Since the scheme considers each element and node separately the propagation wave it is transmitted directly numerically only to its neighbors in a one element distance during each time step.

3.2 Kinematic equations

For biological tissues, including the brain, it is difficult to uniquely identify an undeformed, stress-free reference configuration since the tissues are prestressed in the physiological state[60]. With that, the reference configuration chosen is the physiological prestressed state. Strains and stresses are not directly related to the deformation mapping $\boldsymbol{\varphi}$ but to its tangent, the deformation gradient $\mathbf{F}$.

For an arbitrary displacement of a body with reference coor-dinate, $\mathbf{X}$, and current configuration $\mathbf{x}$ with a mapping function $\boldsymbol{\varphi}$ between reference and current configuration we have:

$$\mathbf{x} = \varphi(\mathbf{X}), \qquad \mathbf{F} = \frac{d\boldsymbol{\varphi}}{d\mathbf{X}} = \frac{d\mathbf{x}}{d\mathbf{X}} = \nabla x \boldsymbol{\varphi} \tag{3.2.1}$$

And the Jacobian or volume ratio defined as:

$$J = det(\mathbf{F}) = \lambda_1 \lambda_2 \lambda_3 = \frac{V}{V_0} \tag{3.2.2}$$

where "λ" are the stretch ratio (or simply stretch), to define the deformation the three principal stretches are used. The definition for the uniaxial tension as:

$$\lambda = \frac{L}{L_0} = \frac{L + \Delta u}{L_0} = 1 + \varepsilon_E \tag{3.2.3}$$

with "ε_E" being the engineering strain

To account for the characteristic quasi-incompressible behavior of soft biological tissues, a volumetric isochoric decomposition of the deformation gradient $\mathbf{F}$ is adopted. The overbar is associated to the prefix isochoric and denotes the volume-preserving part, $(J = 1)$. Accordingly, $\bar{\mathbf{F}}$ denotes the isochoric deformation gradient.

$$\mathbf{F} = \mathbf{J}^{1/3}\bar{\mathbf{F}} \quad with \quad det(\bar{\mathbf{F}}) = 1 \tag{3.2.4}$$

Likewise

$$\bar{\lambda_p} = \mathbf{J}^{-1/3}\lambda_p \qquad (p = 1, 2, 3) \tag{3.2.5}$$

The deformation gradient introduces the right Cauchy-Green deformation tensor $\mathbf{C}$, note that due to symetry is the same working with the right Cauchy-Green deformation tensor $\mathbf{C}$ or the left $\mathbf{B}$.

$$\mathbf{C} = \mathbf{F}^T \cdot \mathbf{F} = J^{2/3}\bar{\mathbf{C}} \quad with \quad \bar{\mathbf{C}} = \bar{\mathbf{F}}^T \cdot \bar{\mathbf{F}} \tag{3.2.6}$$

In order to discretize some energy density functions it is also convenient to introduce the invariants I_1, I_2 and I_3 in terms of the right Cauchy-Green tensor and in terms of the principal stretches.

$$\begin{aligned} I_1 &= tr(\mathbf{C}) && with && \partial I_1/\partial \mathbf{C} = \mathbf{I} \\ I_2 &= \frac{1}{2}[tr^2(\mathbf{C}) - tr(\mathbf{C})] && with && \partial I_2/\partial \mathbf{C} = I_1\mathbf{I} - \mathbf{C} \\ I_3 &= J^2 = det(\mathbf{C}) && with && \partial I_3/\partial \mathbf{C} = I_3\mathbf{C}^{-1} \end{aligned} \tag{3.2.7}$$

And their elastic, isochoric counterparts $\bar{I}_1, \bar{I}_2$ and $\bar{I}_3$ in terms of the right Cauchy-Green tensor and in terms of the isochoric principal stretches.

$$\begin{aligned} \bar{I}_1 &= tr(\bar{\mathbf{C}}) && = J^{-2/3}I_1 = \bar{\lambda}_1^2 + \bar{\lambda}_2^2 + \bar{\lambda}_3^2 \\ \bar{I}_2 &= \frac{1}{2}[tr^2(\bar{\mathbf{C}}) - tr(\bar{\mathbf{C}})] && = J^{-4/3}I_2 = \bar{\lambda}_1^{-2} + \bar{\lambda}_2^{-2} + \bar{\lambda}_3^{-2} \\ \bar{I}_3 &= det(\bar{\mathbf{C}}) && = J^{-6/3}I_3 = 1 \end{aligned} \tag{3.2.8}$$

3.3 Hyperelastic framework

In order to describe an hyperelastic behavior of a material a constitutive equation is obtained directly from the Clausius-Planck form of the second law of thermodynamics.

$$\mathcal{D}_{\text{int}} = \frac{1}{2}\mathbf{S} : \dot{\mathbf{C}} - \dot{\Psi} - \mathsf{S}_0\,\theta = [\mathbf{S} - 2\partial_{\mathbf{C}}\Psi] : \dot{\mathbf{C}} - \mathsf{S}_0\,\theta \geq 0 \tag{3.3.1}$$

where $\mathcal{D}_{int}$ is the dissipation of internal energy, $\mathbf{S}$ is the second Pila-Kirchoff stress tensor, $\dot{\mathbf{C}}$ is the time derivative of the right Cauchy-Green strain tensor, $\dot{\Psi}$ is the time derivative of the strain energy density function (SEDF) and $\mathsf{S}_0\,\theta$ is the material form of the internal dissipation and the entropy respectively. Note that for the purpose of this project, a purely mechanical theory is used, then the thermal effects are ignored (S_0 and θ are omitted) as a perfectly elastic material is considered [30], leading to the degeneration of the inequality into:

$$(\mathbf{S} - 2\partial_{\mathbf{C}}\Psi) : \dot{\mathbf{C}} = 0. \tag{3.3.2}$$

As $\mathbf{C}$ and hence $\dot{\mathbf{C}}$ can be different to zero, the expression in parenthesis should be null, and the well known expression for the second Piola-Kirchoff is retrieved.

$$S = 2\frac{\partial \Psi(\mathbf{C})}{\partial \mathbf{C}} \tag{3.3.3}$$

Since some materials behave quite differently in bulk and shear it is most beneficial to split the deformations into a local *volumetric* (or dilational) elastic part and an *isochoric* (or distortional) elastic response represented also with a "bar" on top.

$$\Psi(\mathbf{C}) = \Psi_{vol}(J) + \Psi_{iso}(\bar{\mathbf{C}}) \tag{3.3.4}$$

And combining equations 3.3.4 in 3.3.3, the second Piola-Kirchoff can be easily separated in the additive decomposition.

$$S_{vol} = \frac{\partial \Psi_{vol}(J)}{\partial \mathbf{C}} = J\frac{d\Psi^{\infty}_{vol}(J)}{dJ}\mathbf{C}^{-1} = Jp\mathbf{C}^{-1} \tag{3.3.5}$$

$$S_{iso} = \frac{\partial \Psi_{iso}(\bar{\mathbf{C}})}{\partial \mathbf{C}} = J^{-\frac{2}{3}}Dev(\bar{S}) = J^{-\frac{2}{3}}\mathbb{P} : \bar{S} \tag{3.3.6}$$

$$Dev(\cdot) = (\cdot) - \frac{1}{3}[(\cdot) : \mathbf{C}]\mathbf{C}^{-1} = \mathbb{P} : (\cdot) \tag{3.3.7}$$

Here, "$\mathbb{P}$" is the fourth order projection tensor $\mathbb{P} = \mathbb{I} - \frac{1}{3}\mathbf{C} \otimes \mathbf{C}^{-1}$ and with the constitutive equations for the hydrostatic pressure "p" and the fictitious second Piola-Kirchoff stress "$\bar{S}$" defined by

$$p = \frac{d\Psi_{vol}(J)}{dJ} \qquad and \qquad \bar{S} = 2\frac{\partial \Psi_{iso}(\bar{\mathbf{C}})}{\partial \bar{\mathbf{C}}} \tag{3.3.8}$$

It is important to notice that, although sometimes it may be useful to think of the function "p" as being equivalent to the hydrostatic pressure, this terminology has been a source of confusion in the biomechanics literature. Several authors have associated "p" with a "tissue pressure" that can be measured with an appropriate transducer. In fact, that function does not have a direct physical interpretation. Rather, it is a Lagrange multiplier that is needed to enforce the incompressibility constraint.

All the equations have been worked in terms of the second Piola-Kirchoff stress tensor. However, the Cauchy stress (or true stress) and the Kirchhoff can be easily obtained using a full push-forward operation as indicates in 3.3.9.

$$\sigma = J^{-1}\tau = J^{-1}\chi_*(\mathbf{S}) = J^{-1}\mathbf{F}\mathbf{S}\mathbf{F}^T \tag{3.3.9}$$

Decoupling the function as seen in eq. 3.3.3 and having that $\mathbf{C}^{-1} = \mathbf{F}^{-1}\mathbf{F}^{-T}$ the volumetric part that describes the hydrostatic pressure can be obtained as

$$\sigma_{vol} = 2J^{-1}\mathbf{F}\frac{\partial \Psi_{vol}(J)}{\partial \mathbf{C}}\mathbf{F}^T = J^{-1}\mathbf{F}(Jp\mathbf{C}^{-1})\mathbf{F}^T = p\mathbf{I} \tag{3.3.10}$$

and using the equation 3.3.6 and the kinematic relation from eq. 3.2.4 the isochoric Cauchy stress contribution can be found

$$\begin{aligned}\sigma_{iso} = 2J^{-1}\mathbf{F}\frac{\partial \Psi_{iso}(\bar{\mathbf{C}})}{\partial \mathbf{C}}\mathbf{F}^T &= J^{-1}\mathbf{F}(J^{-\frac{2}{3}}\mathbb{P} : \bar{S})\mathbf{F}^T \\ &= J^{-1}\bar{\mathbf{F}}(\mathbb{P} : \bar{S})\bar{\mathbf{F}}^T\end{aligned} \tag{3.3.11}$$

3.3.1 Invariant based method

As the Mooney-Rivlin function has been defined in terms of principal invariants, we apply the chain rule and obtain

$$\frac{\partial \Psi(\mathbf{C})}{\partial \mathbf{C}} = \frac{\partial \Psi}{\partial I_1}\frac{\partial I_1}{\partial \mathbf{C}} + \frac{\partial \Psi}{\partial I_2}\frac{\partial I_2}{\partial \mathbf{C}} + \frac{\partial \Psi}{\partial I_3}\frac{\partial I_3}{\partial \mathbf{C}} = \sum_{a=3}^{3}\frac{\partial \Psi}{\partial I_a}\frac{\partial I_a}{\partial \mathbf{C}} \tag{3.3.12}$$

The derivatives respect of the invariants with respect to $\mathbf{C}$ as needed above can be find it in 3.2.7 That after substituting it into the constitutive equation gives the most general form of a stress relation in terms of the three strain invariants, which characterizes isotropic hyperelastic materials at finite strains

$$\mathbf{S} = 2\frac{\partial \Psi(\mathbf{C})}{\partial \mathbf{C}} = 2\Big[\Big(\frac{\partial \Psi}{\partial \bar{I}_1} + I_1\frac{\partial \bar{\Psi}}{\partial \bar{I}_2}\Big)\mathbf{I} - \frac{\partial \Psi}{\partial I_2}\mathbf{C} + I_3\frac{\partial \Psi}{\partial I_3}\mathbf{C}^{-1} \tag{3.3.13}$$

Either Neo-Hookean and the Mooney-Rivlin models fails to represent the behavior of rubbery materials at very large strains [49]. To overcome those cases the most general form of principal stretches based strain-energy function should be used. On the other hand, the Invariants based models are much cheaper computationally, which gives them a important role at the small strain domain.

3.3.2 Stretched based methods

Let $[\bar{\lambda_1}, \bar{\lambda_2}, \bar{\lambda_3}]$ be the principal isochoric stretches, related to the principal stretches λ_i as in equation 3.2.5 that can also be seen as:

$$\bar{\lambda_i} = \frac{\lambda_i}{J^{\frac{1}{3}}} = \frac{\lambda_i}{(\lambda_1\lambda_2\lambda_3)^{\frac{1}{3}}} = \lambda_i^{\frac{2}{3}}(\lambda_j\lambda_k)^{\frac{-1}{3}} \tag{3.3.14}$$

where (i, j, k) are cyclic permutations of (1,2,3). The corresponding constitutive function for the potential relation with the Kirchoff stress tensor is

$$\tau_i = \lambda_i\frac{\partial \Psi_{iso}}{\partial \lambda_i} \qquad \text{(no summation on index i)} \tag{3.3.15}$$

With the above strain-energy function, we have

$$\tau_i = \lambda_i\Big(\frac{\partial \Psi_{iso}}{\partial \bar{\lambda_i}}\frac{\partial \bar{\lambda_i}}{\partial \lambda_i} + \frac{\partial \Psi_{iso}}{\partial \bar{\lambda_j}}\frac{\partial \bar{\lambda_j}}{\partial \lambda_j} + \frac{\partial \Psi_{iso}}{\partial \bar{\lambda_k}}\frac{\partial \bar{\lambda_k}}{\partial \lambda_k} + \frac{\partial \Psi_{vol}}{\partial J}\frac{\partial J}{\partial \lambda_i}\Big) \tag{3.3.16}$$

where again no summation is implied on repeated indices and (i, j, k) are permutations of (1,2,3).

3.3.3 Wave propagation in Hyperelastic Materials

While using the Software EUROPLEXUS is noticed that the computation of the wave speed is giving incorrect results. This parameter is directly related to the stability and is crucial for the explicit method, and so it will be developed.

The equations of motion of the wave propagation in a solid are those of a small "incremental" deformation superimposed on a large deformation [37]. Which equation of motion of a compressible wave is:

$$\nabla \cdot \Sigma = \rho \mathbf{x}'' \tag{3.3.17}$$

where

$$\Sigma = \mathbf{A}_0 \nabla \mathbf{x} \qquad and \quad \mathbf{A}_0 = \frac{\partial^2 \Psi}{\partial F \partial F} \tag{3.3.18}$$

In homogeneous plane waves the unit $\mathbf{n}$ is real and defines the direction of propagation of the wave, where $\mathbf{m}$ is the polarization vector, and c is the wave speed

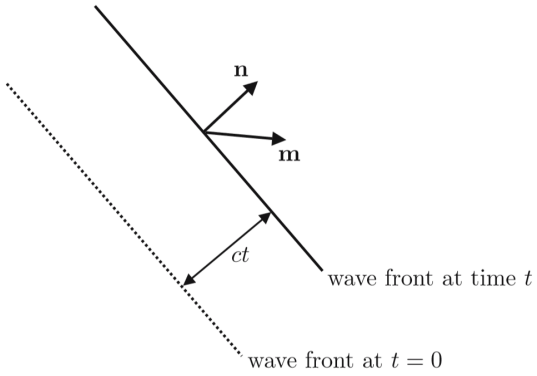

Figure 3.3.1: plane wave with unit normal n and polarization m

From [49] we can extract the following equation of the incremental plane wave, where easily can be deducted the speed of sound.

$$\rho c^2 = [\mathbf{Q}_0(\mathbf{n})\mathbf{m}] \cdot \mathbf{m} = \mathcal{A}_{0\text{piqj}} n_p n_q m_i m_j \tag{3.3.19}$$

where $\mathcal{A}_0$ is the push forward of $\mathcal{A}$, which is the elasticity tensor and with $\rho c^2 > 0$.

3.4 Constitutive hyperelastic equations

From the previous section we have learned that the stress response of hyperelastic materials is derived from a given strain-energy function φ. Numerous specific forms

of strain-energy functions to descrive the elastic properties have been proposed in the literature and more or less efficient new specific forms are published on a daily basis.

The aim of this section is to specify two forms of strain-energy functions which are widely used within soft tissue discretization and particularly the brain, which describe isotropic hyperelastic materials. In particular the Ogden and the Mooney-Rivlin models are presented in a Incompressible formulation, and also some particular forms which are able to describe compressibility.

3.4.1 Ogden material

One of the most used hyperelastic material for modeling brain tissues is the Ogden form, one of the characteristics of this formulation is that since is basen on principal stretch ratios directly, and it may be more accurate and may provide better data fitting than other simpler models, however is more computationally expensive. In general can be applied for strains up to 700%.

One curiosity found in this hyperelastic form is that there are different expressions for the strain-energy density depending which source is consulted. In case to use as reference the classical model found in [30, 19] it makes reference to the equation 3.4.1, and if some commercial softwares are checked like Abaqus [1] it is seen that it uses equation 3.4.2 which is slightly different.

$$\Psi_{iso} = \sum_{i=1}^{N} \frac{\mu_i}{\alpha_i} [\bar{\lambda}_1^{\alpha_i} + \bar{\lambda}_2^{\alpha_i} + \bar{\lambda}_3^{\alpha_i}] \tag{3.4.1}$$

$$\Psi_{iso} = \sum_{i=1}^{N} \frac{2\mu_i}{\alpha_i^2} [\bar{\lambda}_1^{\alpha_i} + \bar{\lambda}_2^{\alpha_i} + \bar{\lambda}_3^{\alpha_i}] \tag{3.4.2}$$

In any case, both formulations would be treated the same way as long as are stretch ratio based strain energy functions. Now the particular solution of the Ogden model Cauchy stress tensor will be deducted.

The final expression for the principal Kirchoff stress for the classical strain-energy function 3.4.1 reads

$$\tau_{iso,i} = \sum_{p=1}^{N} \mu_p J^{-\alpha/3} \Big[\lambda_i^{\alpha_p} - \frac{1}{3} \big(\lambda_1^{\alpha_p} + \lambda_2^{\alpha_p} + \lambda_3^{\alpha_p} \big) \Big] \tag{3.4.3}$$

3.4.2 Mooney-Rivlin material

As a particular case of an Ogden material, the invariant based MooneyRivlin model is obtained by setting $N = 2$, $\mu_1 = 2C_1$, $\mu_2 = 2C_2$ and $\alpha_1 = 2$, $\alpha_2 = 2$, also note that the standard neo-Hookean material is recovered with $N = 1$, $\mu_1 = 2C_1$ and $\alpha_1 = 2$. Being an invariant based material means that is simpler and cheaper computationally, but also that cannot undergo strains as large as a stretch based model as could it be the ogen. This models are widely used for its simplicity or as a first approximation of an hyperelastic material.

Using the strain invariants in a deviatoric form $\bar{I}_1$, $\bar{I}_2$ as presented in equation 3.2.8 we find that

$$\Psi_{iso} = \frac{1}{2}c_1[\bar{\lambda}_1^2 + \bar{\lambda}_2^2 + \bar{\lambda}_3^2 - 3] + \frac{1}{2}c_2[\bar{\lambda}_1^{-2} + \bar{\lambda}_2^{-2} + \bar{\lambda}_3^{-2} - 3] \tag{3.4.4}$$

$$= \frac{1}{2}C_{10}[\bar{I}_1 - 3] + \frac{1}{2}C_{01}[\bar{I}_2 - 3] \tag{3.4.5}$$

This strain-energy function involves a couple of parameter only and provides a mathematically simple and reliable constitutive model for the nonlinear deformation behaviour of isotropic materials. It relies on phenomenological considerations and includes typical effects known from nonlinear elasticity within the small strain domain.

3.4.3 Lagrange multiplier for volumetric variations

Biological materials are often slightly compressible and associated with minor dilatational deformations. Compressibility is accounted for by the addition of a strain energy Ψ_{vol}, describing purely the volumetric elastic response. As stated previously 3.3.4 we use the decoupled representation of the strain energy function $\Psi(\lambda_1, \lambda_2, \lambda_3) = \Psi_{vol}(J) + \Psi_{iso}(\bar{\lambda}_1, \bar{\lambda}_2, \bar{\lambda}_3)$.

For rubber-like hyperelastic materials, Ogden [48, 30] proposed a volumetric response function of the volume ratio J of the following form:

$$\Psi_{vol}(J) = K \cdot \beta^{-2}\left[\beta \cdot ln(J) + J^{-\beta} - 1\right] \tag{3.4.6}$$

where β is a constant to be defined. The strain energy above satisfies the normalization condition, $\Psi_{vol}(1) = 0$. Usual values for β could be $\beta = -2$ or $\beta = -1$.

Regularized models of the above type are frequently used to emulate incompressibility in finite element analyses.

It has been noted that in the bibliography [19] that other methods are used to compute the compressibility part, it is accounted that the incompressible limit (where J = 1) is approached as $K \to \infty$. In this case, the bulk modulus K may be seen as a penalty factor that penalizes volumetric deformations.

$$\Psi_{vol}(J) = \frac{1}{2}K(ln(J))^2 \tag{3.4.7}$$

Note also that other formats of volumetric (penalty) contribution to the strain-energy function may be adopted in this context, for example the formulation of Abaqus or Ansys 3.4.8 that accounts for a computationally cheaper equivalent model.

$$\Psi_{vol}(J) = \sum_{k=1}^{N} \frac{1}{2}K(J-1)^{2\cdot k} \tag{3.4.8}$$

for instance, is also frequently adopted (see, among others, Crisfield 1997) in the finite element analysis of nearly incompressible materials.

Lets Remark that this section is taking the hypothesis of quasi-incompressibility, in modeling materials whose compressibility is an important feature of the overall response, the functional form of the volumetric contribution to the strain-energy function should be determined on the basis of experimental evidence rather than just postulated as above.

3.4.4 Consistency with linear theory

In order to be able to compare the phenomenological nonlinear elastic parameters, that do not hold any physical interpretation, to experimental studies there is a need of a correlation between them.

On comparison the hyperelastic with the linear theory we obtain the consistency condition that relates the Ogden parameters with the classical shear modulus.

$$\begin{aligned} 2\mu &= \sum_{i=1}^{N} \alpha_p \mu_p && \text{refers to the classical formulation, equation 3.4.1} \\ \mu &= \sum_{i=1}^{N} \mu_i && \text{refers to the "Abaqus" formulation, equation 3.4.2} \end{aligned} \tag{3.4.9}$$

this relation can be found also in the case of the Mooney-Rivlin material model.

$$\mu = 2(C_1 + C_2) \tag{3.4.10}$$

By using the bulk modulus which is determined constant during all the calculation and the shear modulus obtained form the equations above, the Poisson coefficient can be computed easily.

$$\nu = \frac{3 \cdot \frac{K}{\mu} - 2}{6 \cdot \frac{K}{\mu} + 2} \tag{3.4.11}$$

And to finish, most of the commercial softwares use a different way to define the bulk modulus (K), using the parameter (D_1) which have a trivial transformation between them.

$$K_0 = \frac{2}{D_1} \tag{3.4.12}$$

3.5 Time Dependent: Viscoelasticity of large strains

The viscoelasticity is the property that adds the effects of time dependency to the elastic response. Unlike other properties we will not talk of linear viscoelasticity when there is a linear response, but when the function can be separated in both creep response and load. While the nonlinear viscoelasticity is when the function is not separable, which It usually happens when the material changes its properties under deformations.

For the current problem in this document linear viscoelasticity will be used.

3.5.1 Prony series

Large-strain visco-hyperelasticity is based on the formulation proposed by Simo [64], amended here to take into account the viscous volumetric response and the thermorheological simplicity. Simo's formulation is an extension of the small strain theory. Again, the viscoelastic behavior is specified separately by the underlying elasticity and relaxation behavior.

To accurately model this phenomena in the brain and to be able to add it to the hyperelastic term, a $n-order$ Prony series is proposed, which has already ben shown to be a powerful method for numerical modeling of soft tissue [11, 23]. In this method, time dependent stresses are added to the hyperelastic stress tensor as it follows:

$$\mathbf{S}(t) = \int_0^t \left[g_\infty + \sum_i g_i e^{(-((t-\tau)/\tau_i))} \right] \frac{\partial \mathbf{S}_e^d}{\partial \tau} d\tau \tag{3.5.1}$$

where $\mathbf{S}_e^d$ is the deviatoric elastic second Piola-Kirchoff stress tensor as the volumetric behavior is assumed to be time independent. τ represents the time variable, g_∞ is the long term parameter shearing relaxation moduli recovering the role of G in a dimensionless form ($g_i = G_i(t)/G_0$), and τ_i are the time decay constants.

3.6 Head geometries and FEM meshes

With the geometries previously obtained, see table 3.6.1, some of the principal parameters that defines the mesh and its quality and table 3.6.2 for its bounding box. Starting from half a million elements to several millions 3D linear tetrahedral, this meshes are computationally expensive. For the quality parameters, apart form the number of elements, the initial time step and the aspect ratio are shown.

The aspect ratio is the geometrical parameter that relates the longest and shortest edge on an element. While the time step relates the shortest edge with the material of that element, having direct influence to the computation time of the model.

In an explicit time integration method, having elements with one or more edges larger than the other can be considered a waste of computational power since it reduces the time step. For this, in the human mesh and since the , having an aspect ratio of almost 24 means that a few elements are dragging the computation enormously.

Table 3.6.1: Definition of the meshes

Mesh	*Nº Elem*	Element *Type*	Initial *Time Step*	*Aspect ratio: Average / Worst*
Rat	480.227	Tetr.	1,56E-8	1.59 / 5.08
Monkey	1.200.000	Tetr.	1,49E-7	1.33 / 3.73
Human	5.300.000	Tetr.	2,60E-8	1.46 / 23.96

Table 3.6.2: Bounding box of every mesh

Mesh	*X*	*Y*	*Z*
Rat	-1.18E-2 $\leq x$	-1.80E-2 $\leq y$	1.44E-3 $\leq z$
	$x \leq$-4.66E-4	$y \leq$ -1.36E-3	$z \leq$ 9.18E-3
Monkey	-2.91E-2 $\leq x$	-3.74E-2 $\leq y$	-2.31E-2 $\leq z$
	$x \leq$ 2.91E-2	$y \leq$ 3.74E-2	$z \leq$ 2.31E-2
Human	-6.98E-2 $\leq x$	-9.88E-2 $\leq y$	-5.97E-2 $\leq z$
	$x \leq$ 7.02E-2	$y \leq$ 6.92E-2	$z \leq$ 7.50E-2

3.6.1 Rat geometry

The *Rat* is the smallest mammal used on the study and therefore, giving the smallest mesh regarding to the size and number of elements as seen in table 3.6.1.

The geometry of the rat brain, as we can observe in figure 3.6.1, seems quite simple without any notorious foldings or big discontinuity as we can find in other, "more evolved" mammals like the monkey or the human.

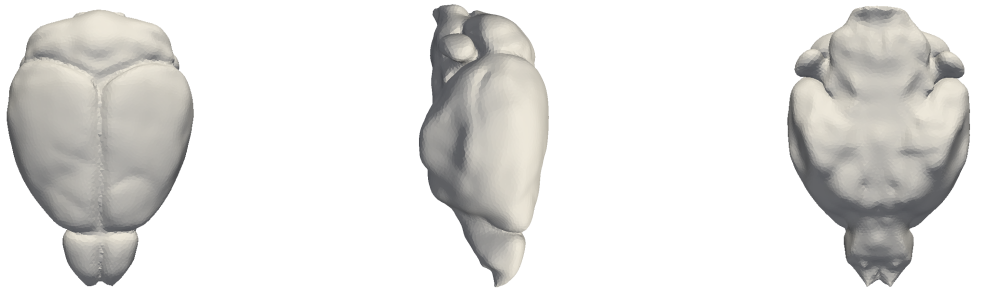

(a) Top view (b) Side view (c) Bottom view

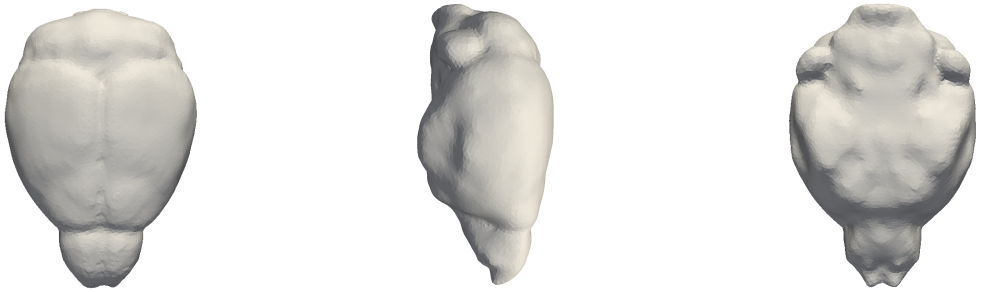

(d) Top view (e) Side view (f) Bottom view

Figure 3.6.1: On the top row there is the Brain mesh of the rat brain in different views, and in the bottom row there is depicted the outer boundary of the CSF mesh where the initial velocity is imposed.

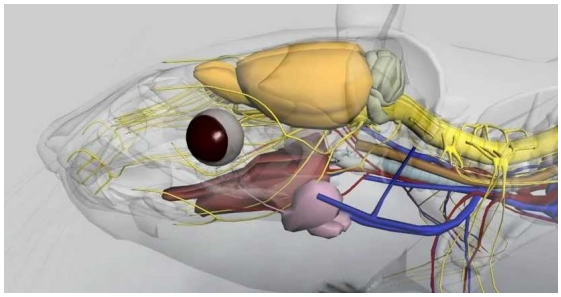

Figure 3.6.2: Real rat head with the model of the the brain obtained from the webpage in [69]

In figure 3.6.1 bottom row (d-f) represents the mesh outer boundary also modeled as the "skull" in the blast loading case. But as seen in figure 3.6.2 and even if the whole head has a lot of other components that are not taken into account, the model of the brain is accurate.

3.6.2 Monkey

The *monkey* is the mammal which brain is the closest to the human see figure 3.6.3, and therefore making a perfect candidate to study prior to dealing with the human. This model starts having more geometrical parameters involved, since it clearly have two hemispheres and the cerebellum is in the same position as in the human. The

foldings that defines a gyrencephalic brain exists all over the surface and also are perfectly visible to naked eye having a clear affection to the results.

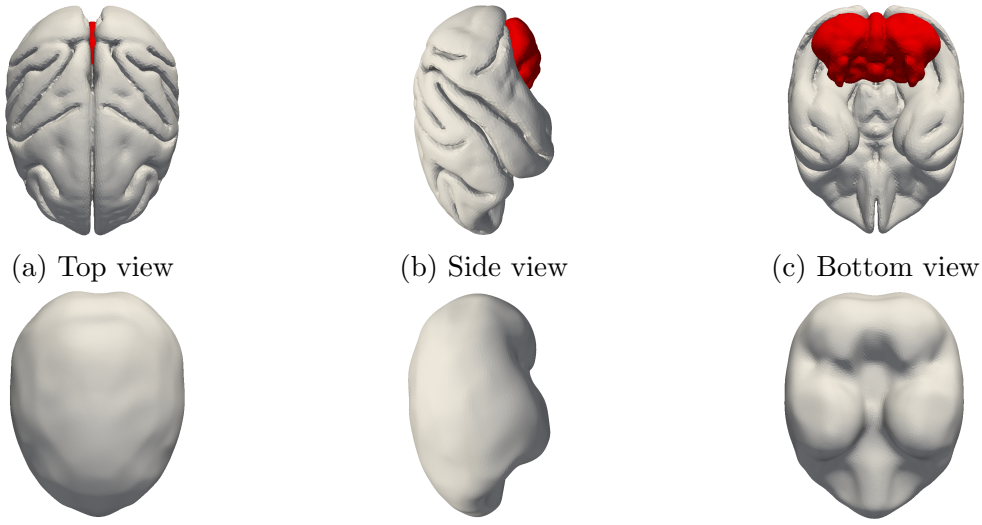

(a) Top view (b) Side view (c) Bottom view

(d) Top view (e) Side view (f) Bottom view

Figure 3.6.3: Centered scaled monkey brain (top row) and "skull" (bottom row) surface meshes.

Even with all the complexity of the monkey brain, this model will be the one selected as reference where the majority of the analysis are going to be carried. The main reason being that this geometry is the fastest of all as can be understood in Table 3.6.1. Here it shows the importance of the time step previously stated, since it makes that a model with 2,5 times more elements be several times faster than the others.

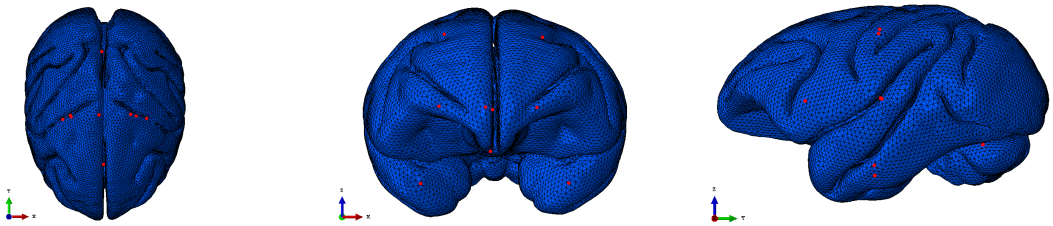

(a) Top view (b) Side view (c) Bottom view

Figure 3.6.4: Representative points for the monkey mesh for the treatment of the time dependent part of the outputs

3.6.3 Human

The human brain is the most complex of all mammals, see figure 3.6.5. A mesh that is ready to be launched for the full problem is still on ongoing development see, [8], but some attempts have been made using an available mesh demonstrating that even if there are some features that need refining it still can be used.

If we compare that mesh with the previous two, we can se clearly that the complexity of the surface is much higher that any of the other geometries in study. Also in our case the human mesh includes the definition of two sets, the gray and the white matter, allowing the heterogeneity consideration.

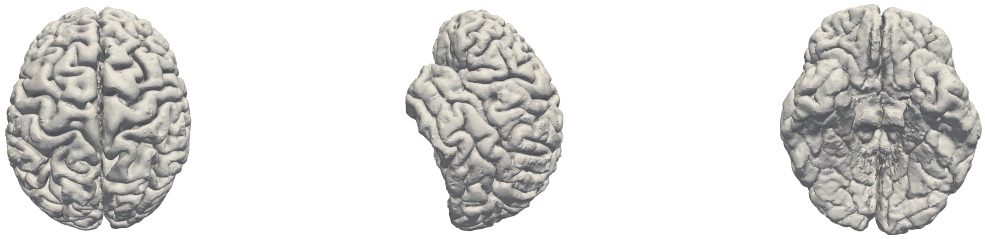

(a) Top view (b) Side view (c) Bottom view

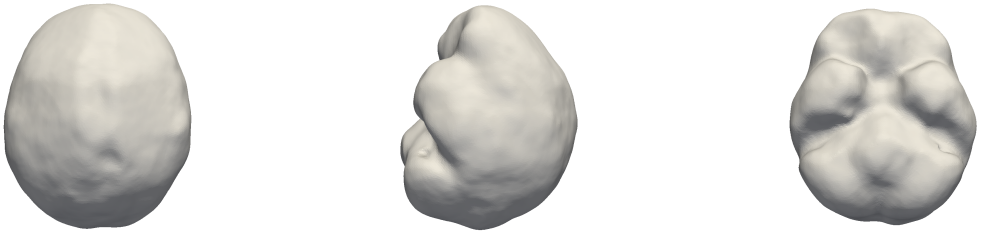

(d) Top view (e) Side view (f) Bottom view

Figure 3.6.5: On the top row, views of the human brain mesh and on the bottom row the outer boundary surfaces that are modeled as the skull.

3.7 Load

3.7.1 Shock-wave

To mimic the effect of explosive blast exposure a shocktube should be used, it recreates a cut-out segment of the open field blast wave enabling high reproducibility. In experimentation the animal should be placed inside the tube to be affected from overpressure, if placed outside or near the aperture the only affections would be due to the blast wind that would only reproduce a coup contracoup injury.

The validation of the model will be done with the simulation of the experiment of Evan Calabrese et al. [4] consisting in a blast generated with a shock-tube, with a Rat tautly secured in a coarse net 75cm within the mouth of the expansion chamber, see picture 3.7.1.

For the modeling of this experiment, even if a full 3D fluid structure interaction could be used, a more simplistic and computationally cheaper solution will be developed. Being that solution to decouple the Eulerian computation (the shock-tube experiment) from the Lagrangian calculation (Brain).

Using EUROPLEXUS and with the help of G. Valsamos (JRC) the FE model of the shock-tube used in the experiment is performed, getting the pressure curve that

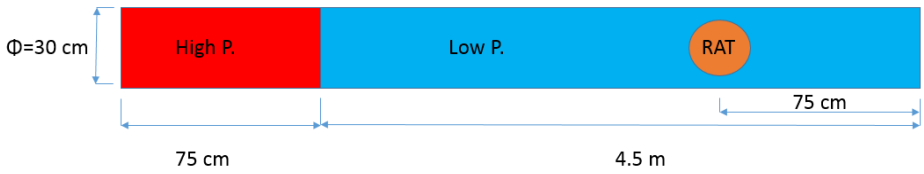

Figure 3.7.1: Pressure curve got form the shock-tube

will be applied in the brain computed (figure 3.7.2). This pressure will be applied uniformly to half of the head in the lateral axis and the atmospheric pressure to the other half of the head, view subsection 3.8, which is a close approximation of the real behavior of the shock-wave even if it does not take into account the variation of pressures over the surface, absolutely neglecting the load propagated in the opposite face of the head, neither it takes into account the angle of application of the pressure.

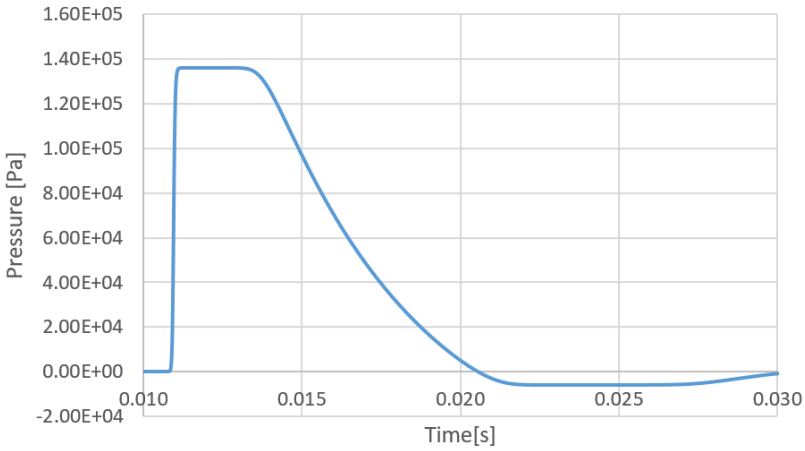

Figure 3.7.2: Pressure curve got form the shock-tube

It has been checked that the software is able to solve the real fluid structure interaction problem giving the exact load at each node of the skull, but since it is a preliminary study that aims to know what happens in the interior of the head, this approximation of the blast effect is considered valid as long as it is consistent in all the models.

3.7.2 Impact

As we saw in the previous chapter in figure (1.1.1) the direct damage caused by the shock-wave is just one of the possible causes of injury in the human head, leaving the secondary effects (debris) apart, since it produces puncture and penetration damage mainly. Leaving another big group, the tertiary effects or the impact against surrounding structures will be also studied. Note that this section could also be used in any other field apart from tertiary effects of explosions, i.e. car accidents, boxing, American football, etc.

In this section the load considered will be a linear deceleration with initial velocity $V_0 = 0.1m/s$ at the initial time $t_0 = 0s$ down to $0.0m/s$ at $t_1 = 25ms$, followed by an imposed zero velocity until the chosen final time of $t_f = 50ms$.

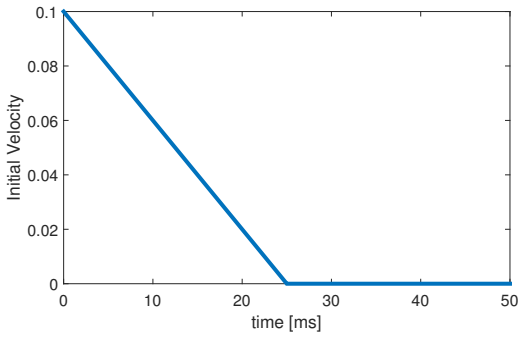

Figure 3.7.3: Time evolution of the skull velocity

3.8 Boundary conditions

Being able to simulate an explosion or an impact to the head, the question on how to fix the model remains. Ideally, one should be able to model the full neck and its rotational effects which effects proved very important into the final results [16]. Or in case of the verification experiment [4], the net that fix the rat head into the shock-tube would be needed.

For the case of the impact, a uniform velocity is applied in all the nodes that belong to the outer surface or the CSF, making a straight trajectory with a predefined displacement.

The blast, as a preliminary approach, and since the load is applied as an external pressure, a series of springs has been designed at the exterior part of the skull as it is displayed in figure 3.8.1 both for the rat and the monkey.

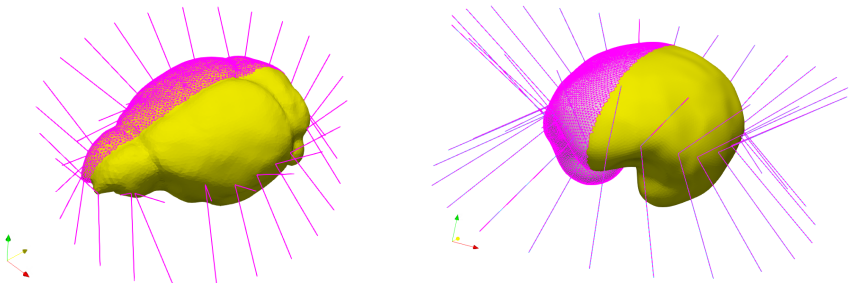

(a) Rat Brain (b) Monkey brain

Figure 3.8.1: Boundary condition on the blast geometries.

In this images, the half of the brain that is highlighted is where the pressure, from figure 3.7.2 is applied while the cables that are around the brain are the springs that fix it on its place.

Table 3.8.1: Material parameters of the spring

	$\rho[kg/m^3]$	$E[MPa]$	$\nu[-]$	Elastic limit $[MPa]$	Rupture strain
Spring	1800	3	0.21	30	10

The properties of this springs are related to their number and the mass of the brain, calibrated in order to allow an acceptable movement of around 10 cm, table 3.8.1. The material used for modeling this springs is an specialized cable material of EUROPLEXUS "FUNE", that represents an elastoplastic cable with no resistance in compression.

3.9 Parallelization

Since the models that we are working with have in the order of millions of elements, some way to speed up the calculation must be used. The most usual form and the one that either EUROPLEXUS and Abaqus uses is the domain decomposition. This method allow nonconforming meshes along the interfaces between sub-domains, parallelization of the memory partition (SMP) it creates relatively localized modifications in the program. The distribution of the work is done at the level of the various calculation tasks, all accessing the entire memory.

The implementation of the reference OpenMP is presented in the form of directives to be inserted in the sequential reference code to control the parallel options, for example to distribute the iterations of a FOR loop on the simultaneous processes assigned to the program or threads

In our case, the representation of the sub-domains on both meshes (Rat and monkey) can be appreciated in figure 3.9.1 using 32 threads. while in table 3.9.1 the speed up per millisecond of calculation while using the parallel method is shown.

Table 3.9.1: Speed up of the calculation per millisecond of the rat brain using parallel method

	CPU cost $[hours]$	Speed up
Sequential	70 h (2.9 days)	-
32 procs	3.6 h	19
64 procs	2.1 h	33

3.9.1 Spatial Partitioning

The spatial partitioning is a technique existing in EPX [9] that it distributes the elements among various "partition levels" depending on the their own time step.

Mainly if there are different materials with different c_i or if there is a big dispersion in element size

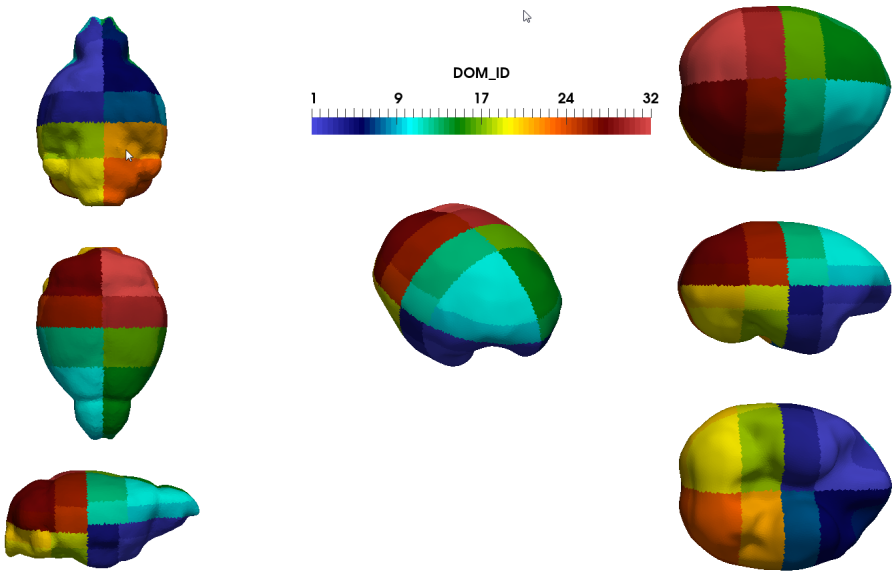

(a) Rat Brain (b) Monkey brain

Figure 3.9.1: Partition of the meshes into sub-domains by EUROPLEXUS

In this way, the code integrates more frequently the elements with smaller time step, while the elements with its time step much higher than the critical are integrated less frequently.

For the interested reader on going more into detail of this method it is recommended to check the previously stated paper from Folco Casadei [9].

This method will be tried and failed its use, which would give us important information regarding that the software way of computing the wave speed propagation is wrong and has to be reformulated.

3.10 Anisotropy in the model

As it is well known the brain has a very anisotropic behavior, for this end two approaches could be taken to add the anisotropy to the model. On one hand, and the one used in most of the studies (like [11, 23]) is to adopt a diffusion tensor imaging to inform anisotropic material models representing brain tissue.

On the other hand, and the approach taken in this paper is to add the anisotropy superposing a mesh of 1D fibers (which are the wires of white matter that connect the different parts and lobes of the brain) as a reinforcement to the base isotropic material, since it is deduced that this is closer to reality.

3.10.1 Tractography of the monkey

As stated previously in section 3.10 this thesis prepared the anisotropy to be implemented by the superposition of a 1D fiber mesh to the 3D isotropic brain material.

The mesh of fibers to be superposed in the monkey brain is ready, as can be observed in figure 3.10.1, and fitted in the monkey brain, figure 3.10.2. As commented also previously, there were problems with the hierarchy of the objects of the fibers mesh in the software EUROPLEXUS, due to that no analysis could be carried with anisotropy during this thesis.

(a) +X View (b) +Y View (c) +Z View

Figure 3.10.1: Set of fibers of the monkey brain.

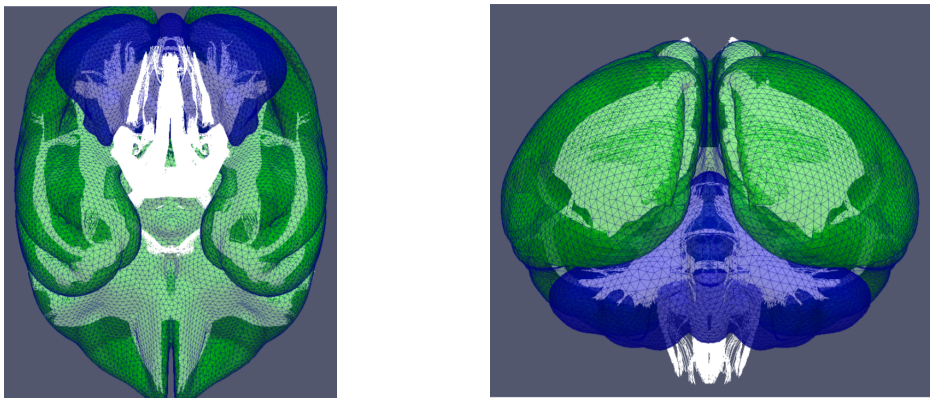

(a) Top view (b) Side view

Figure 3.10.2: Fibers fitted in the monkey brain

3.10.2 Axon distribution

The approach that will be considered in this thesis for the anisotropy, as commented previously, will be to implement the diffusion tractography models as explicit fiber network model.

Since the Tractography obtained is extremely detailed, having tens of millions of elements, some refinement had to be done. For the interested reader, the procedure is explained in the paper that is being prepared for publication together with this document [8].

The idea of how the filtering is done is, first of all, since the precision of the tractography is too small and though the distance of the 1D nodes too short, a minimum element length is imposed and merged the bar elements until the min length (l = 0,5 mm) was met, being that length the usual 3D element size of the brain material. With this the number of elements is reduced by a factor seven in the process.

After that, an un-refinement of the fibers is done, and since there are parts where the fibers are too close one with the others, a merging of the close nodes and elements is done. The procedure is very simple and explained in detail in the same document previously stated. First, the nodes that are too close with each other, $d = 0,5mm$ same distance as the element length, are localized and merged as displayed in figure 3.10.3 (b).

Then, as a consequence of the elimination of nodes there will be a lot of superimposed elements, that is elements that share the same nodes that has been merged. To overcome this issue being consequent in the mechanical behavior, the thickness of the fiber that remains will be increased proportionally to the number of eliminated elements as depicted in figure 3.10.3 (c).

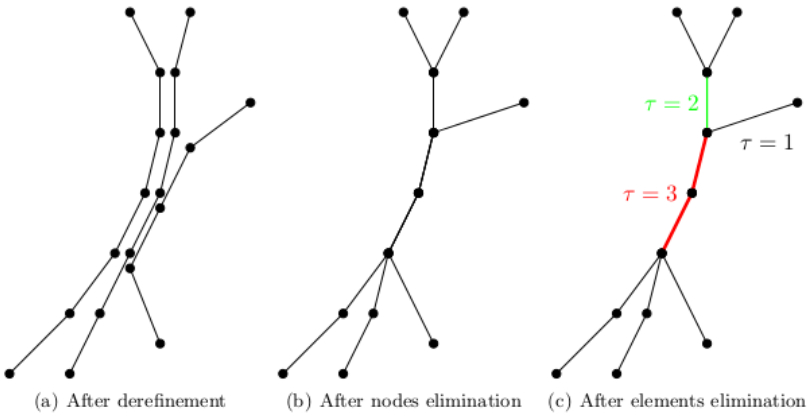

Figure 3.10.3: Un-refining strategy for the fibers [8]

Once we have the 1D mesh reduced and ready to use, the only feature that remains to apply to have the mesh ready is the already existing capability of superimposing two meshes by embedding the fiber of EUROPLEXUS "ARMAT".

For the material model to be used in this mesh of 1D tracts, in the bibliography can be found three alternatives, either using a basic linear elastic model for the axons (tracts) which values can be foun in the literature [25] or either use an hyperelastic approach, which seems more accurate since the tracts are also made of tissue.

While using the hyperelastic approach two opportunities are presented, either use the hyperelastic model presented by Chatelin et all [11] or as it has been done in the Brain tissue to use the strain-stress curves to get the parameters of a more generic model to be used i.e. Mooney-Rivlin or Ogden [31]. Which use in 1D is possible in EUROPLEXUS thanks to the addition of the plane stress, plane strain and uniaxial stress in all the new hyperelastic subroutines.

Since there has been problems in the core of the software EPX about definition hierarchy of the new mesh objects, and it is on the way of being solved by the developers of the software, therefore this method could not be tested during this thesis even if all the foundation has been settled.

The "ARMAT" directive in EUROPLEXUS, allows to link the displacements of the nodes belonging to continuum-like elements, with those of bar-like elements, usually used for structures made of reinforced concrete.

What it does could not be simpler, it simply checks if a node of the bar element is inside the 3D continuum element and if it is, it creates a rigid link between the nodes of the 3D element and the node embedded inside it.

The decoupled treatment of this link also exists and consists in introducing a penalty spring between the reinforced position of the fiber node in the corresponding continuum element and its actual position. This decoupled version it allows some relative movement of the bar node, but never sliding.

The default spring stiffness in the decoupled form is obtained from the continuum element through the formula:

$$k = GL \tag{3.10.1}$$

with G being the bulk modulus of the continuum element material and L is the radius of the sphere whose volume equals the 3D element volume.

Chapter 4

Numerical simulations

Once the problem has been defined, in this chapter some simulations of the models are presented. In section 4.1 the material parameters not taken from papers are computed, in particular the hyperelastic fitting. In sections 4.2 and 4.3 an study of the different loading conditions will be carried.

4.1 Fitting of material parameters

In this section a fitting of the hyper-elastic materials is done using the procedure in subsection 2.2.1. First a stress-strain curve extracted from [54] is set, depicted in figure 4.1.1. As stated previously, we observe that there is a considerable difference between the quasi-static and dynamic loading of about two orders of magnitude.

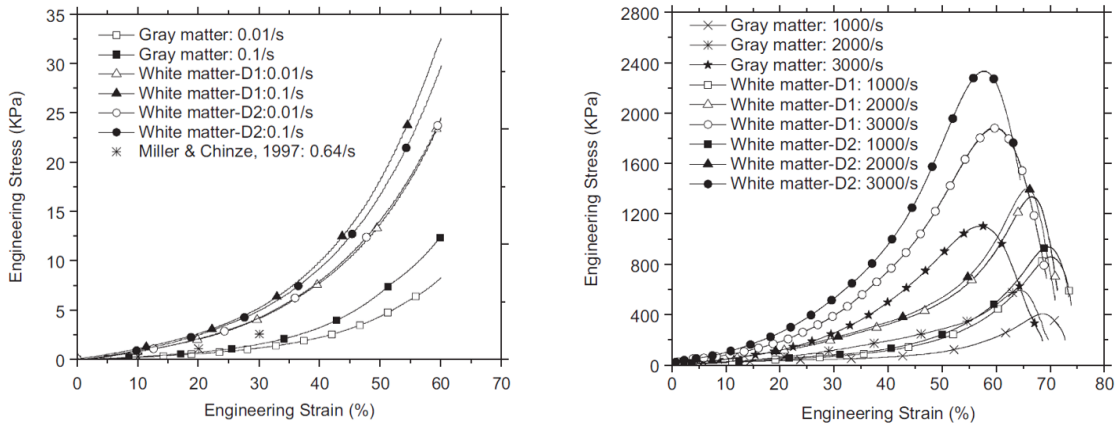

(a) quasi-static strain rates

(b) dynamic strain rates

Figure 4.1.1: Average compressive stress-strain curve of gray and white matter strain rates [54].

Then, with the almost incompressibility constraint $\nu = 0.49$ for wet brain tissue [61], we fit all the experimental curves to obtain material parameters.

Once we got all the parameters for all the curves, a simulation with each material is done, the aim of this is to calibrate the strain rate of the results with the experimental curves. With this we select the curve of 0.1 s^{-1} for the impact and 1000 s^{-1} for the blast case.

As it is depicted in figure 4.1.2a both the Mooney-Rivlin and Ogden materials fit the experimental curve. In figure 4.1.2b the Ogden model with two terms gives the best fit of all the experimental data, so this will be the one used. The damage part of the experimental dynamic curve is not taken into account for the fit since a damage model has not been used. It is not the scope of this study to go to such strains.

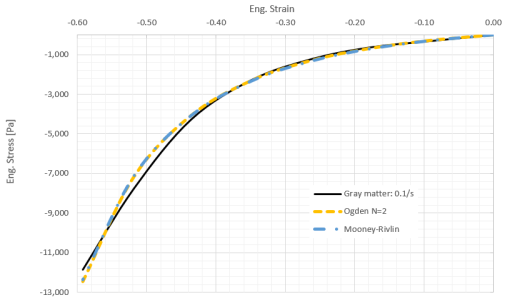

(a) Curve fitting of the Gray matter 0.1/s

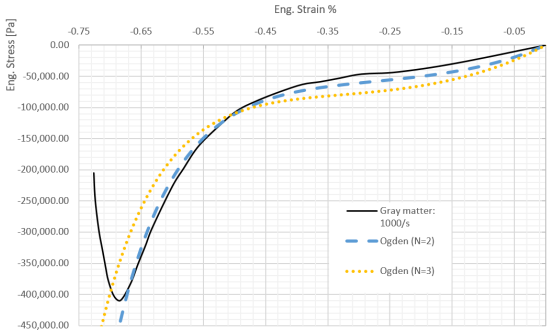

(b) Curve fitting of the Gray matter 1000/s

Figure 4.1.2: Example of curve fitting for gray matter in different strain rates.

Using the same methodology as explained for the gray matter, the parameters for the white matter are also computed. The final values taken for the quasi-static regime in brain matter are shown in table 4.1.1.

Table 4.1.1: Parameters of the brain material for Impact.

Materials	$C_{10}[Pa]$	$C_{20}[Pa]$	$D_1[Pa^{-1}]$
Gray matter	860.00	816.75	3.00E-5
White matter	-26.69	460.85	1.17E-4

The values are modeled in the same way for the dynamic case, the gray matter gives a best fit with a Ogden N=2 and the white matter with a Ogden N=3 is used as seen in table 4.1.2. For the CSF an hyper-elastic of the same form as in the brain is used, but in this case with a higher bulk modulus for making it almost incompressible.

Table 4.1.2: Parameters Hyper-elastic brain material for Blast.

Materials	α_1[-]	α_2[-]	α_3[-]	$\mu_1[Pa]$	$\mu_2[Pa]$	$\mu_3[Pa]$	$K[Pa]$
Gray matter	-8.79	11.00	-	586.94	29868.0	-	5.0E+6
White Matter	8.10	8.85	8.10	3.16E+3	40.50E+3	33.80E+3	1.0E+6

4.1.1 Adjusting springs boundary conditions

For the blast modeling, as explained in figure 3.8, a set of springs are needed for simulate the effect of the neck. The adjustment done will be simplified by using a constant elastic modulus for all the springs that will allow the brain to move around a 10% of its bounding box.

Table 4.1.3: Elasticity parameters for the skull, springs and pia matter.

Materials	$E[Pa]$	ν[-]	$\rho[Kg/m^3]$
Springs	3.0E+6	0.21	1800
Stiffer Springs	6.0E+6	0.21	1800
Weaker Springs	1.5E+6	0.21	1800

4.2 Impact simulations

For the next analysis, in this section a special emphasis will be placed in the monkey brain. It is the fastest model and also incorporates the family of the gyrencephalic,having a complex surface as it has the human one.

To compare the results, a histogram format will be used since is the most accurate representation of the distribution of numerical data in our case. On the histograms the bin-width will be considered constant only in each figure and relative to the dispersion of the results, giving consistent graphics that can be easily compared. In general terms the histogram bin-width will be set to 3.0E-4 for the monkey and human stresses, 3.0E-5 for the strains and for the rat a fifth of the other models will be used, but it will be adapted according to the distribution in each case.

In the case of different meshes, with diverse number of elements, will be compared and since an histogram would not give valuable information, probabilistic plot of the density function with 'Kernel' statistical distribution, which give the best fit to our data, are used.

A Kernel distribution is a nonparametric representation of the probability density function (PDF) of a random variable. It is also defined by a smoothing function and a bandwidth value, which controls the smoothness of the resulting density curve. This distribution is computed by an existing function in a Matlab library.

The reason for using a different approach in comparing diverse meshes is that on the histograms the y-axis represents the number of elements that have a given value, whereas the PDF gives us the relative probability of having that value in the model, regardless of the total number of elements. Also notice that only the brain matter values will be plotted in the results.

All the values shown in this section will be the maximal experimented for each element during all the simulations, also called the "historical maximum", with the

only exception of the graphics with respect to time, but since it was not possible to get the values of each iteration to create the maximum at every increment, we compute an approximation based on the field report outputs.

In this section, the legends of the distribution images or views, will have a specific nomenclature relating the "Max. Principal Logarithmic Strains" with "LEPri", the "Max. Principal Stresses" with "SMaxP", and the "Max. Pressure" with "SPress".

4.2.1 Simulation cases

Table 4.2.1 summarizes all the simulations launched for this chapter, and it is organized as follows. The first column shows the spices that each mesh represents. The second shows the name for that specific simulation will be referenced, which it is prepared to be auto-explicative and easy to relate. The next column represents respectively the direction in which the impact loading is applied, "L" goes for lateral, "F" for Frontal and "Lb,Fb" for Lateral or Frontal but from the back. Next, we have the magnitude of the initial velocity, representing the severity of the impact. And at last the material parameters used in the modeling of each part.

Notice that, as said before, the name of the model summarizes the overall characteristics for quick identification (i.e. "monkey-L01-sca" references to the monkey mesh, with "L" lateral loading, "01" stands for $v_0 = 0.1$, and "sca" means that the mass scaled model to equal the mass of the human brain).

In table 4.2.2 it is shown a representative value of the computational cost of all the simulations launched.

Table 4.2.1: Summary of the Impact simulations launched for this document.

				Parameters	
Spices	*Name*	*Direction*	v_{ini}	Brain	CSF
Monkey	monkey-L001	Lateral	-0.01	Gray	CSF-Hype
	monkey-L01	Lateral	-0.1	Gray	CSF-Hype
	monkey-L1	Lateral	-1	Gray	CSF-Hype
	monkey-L5	Lateral	-5	Gray	CSF-Hype
	monkey-L10	Lateral	-10	Gray	CSF-Hype
	monkey-F01	Frontal	-0.1	Gray	CSF-Hype
	monk-L01-sca	Lateral	-0.1	Gray	CSF-Hype
	monk-L01-visc1	Lateral	-0.1	Gray + Visco1	CSF-Hype
	monk-L01-visc2	Lateral	-0.1	Gray + Visco2	CSF-Hype
	monk-L01-visc3	Lateral	-0.1	Gray + Visco3	CSF-Hype
	monk-L01-lin1-visc1	Lateral	-0.1	Gray + Visco1	CSF-Lin1
	monk-L01-lin1-visc2	Lateral	-0.1	Gray + Visco2	CSF-Lin1
	monk-L01-lin1-visc3	Lateral	-0.1	Gray + Visco3	CSF-Lin1
	monk-L01-MIEG	Lateral	-0.1	Gray	CSF-MIEG
	monk-L01-MIEG-vis	Lateral	-0.1	Gray	CSF-MIEGvis
	monk-L01-lin1	Lateral	-0.1	Gray	CSF-Lin1
	monk-L01-lin2	Lateral	-0.1	Gray	CSF-Lin2
	monkey-L01b	Lateral	+0.1	Gray	CSF-Hype
	monkey-F01b	Frontal	+0.1	Gray	CSF-Hype
	monkey-L01b-lin1	Lateral	+0.1	Gray	CSF-Lin1
	monkey-F01b-lin1	Frontal	+0.1	Gray	CSF-Lin1
Human	human-L01	Lateral	-0.1	Gray	CSF-Hype
	human-L1	Lateral	-1	Gray	CSF-Hype
	human-F01	Frontal	-0.1	Gray	CSF-Hype
	human-L01-wh	Lateral	-0.1	Gray + White	CSF-Hype
	human-L1-wh	Lateral	-1	Gray + White	CSF-Hype
	human-F01-wh	Frontal	-0.1	Gray + White	CSF-Hype
	human-L01-lin	Lateral	-0.1	Gray + White	CSF-Lin1
	human-L01-MIEG	Frontal	-0.1	Gray + White	CSF-MIEG
Rat	rat-L01	Lateral	-0.1	Gray	CSF-Hype
	rat-L1	Frontal	-1	Gray	CSF-Hype
	rat-F01	Frontal	-0.1	Gray	CSF-Hype
	rat-L01-sca	Lateral	-0.1	Gray	CSF-Hype
	rat-L01-MIEG	Lateral	-0.1	Gray	CSF-MIEG

.

Table 4.2.2: Computational cost of the models.

Model	CSF-Hype	CSF-lin	CSF-MIEG
Rat	1:28 h	28:23 h	> 20 days
Rat scaled	0:14 h	12:14 h	40:00 h
Monkey	0:30 h	18:30 h	125 h [5.2*days*]
Monkey scaled	0:27 h	3:20 h	27:15 h
Human	3:40 h	10 days	> 20 days

4.2.2 Analyses of the load rate

As we showed in section 4.1, the strain rate is of great importance in modeling the brain and it must be taken into account in all circumstances. For this reason the very first thing to do is to evaluate the effects of the loading rate in each case.

In the impact or deceleration regime, the loading curve will always be the one explained in subsection 3.7.2, only changing the initial velocity. In this case we will be comparing four initial velocities for the Monkey and only two for the other meshes (human and rat). Also for the human we will consider the two cases of homogeneity and heterogeneity.

The maximum values reached in each element for all the models are shown in figure 4.2.1. In order to be able to compare accurately if a linear variation of the load ends with a linear variation on the outputs, the results will be multiplied for the difference on the load, i.e. "monkey-L01" has 10 times lower velocity than "monkey-L1" so all the outputs of "monkey-L01" will be multiplied by ten. The aim of this analysis is to see how sharp is the effect of the strain rate along the models since in section 4.1 we saw the sensitivity of it.

In table 4.2.3 the relative differences between all the models with initial velocities of 0.001, 0.1 or 1 [m/s] is negligible and so we could say that the different models give the same scaled results. But this linearity of the load rate can be assumed only as we are in a similar strain rate, since these material parameters are valid only for a certain range, due to the huge strain rate dependency of the brain tissue.

As shown in figure 4.2.1b, for the loading of v_0 =5 m/s the behavior starts to change and for the case of v_0 = 10 m/s the mesh is altered completely, giving unusable results. This means that different material parameters should be used for these loads, with appropriate consideration of the strain rate. For the human in (c), a double study is done, considering the whole brain as gray matter and another by using an heterogeneous model introducing the white matter. In this geometry we can see some variance while changing the load, even if it is small. Probably it is due to the complexity of the mesh or to its size of it.

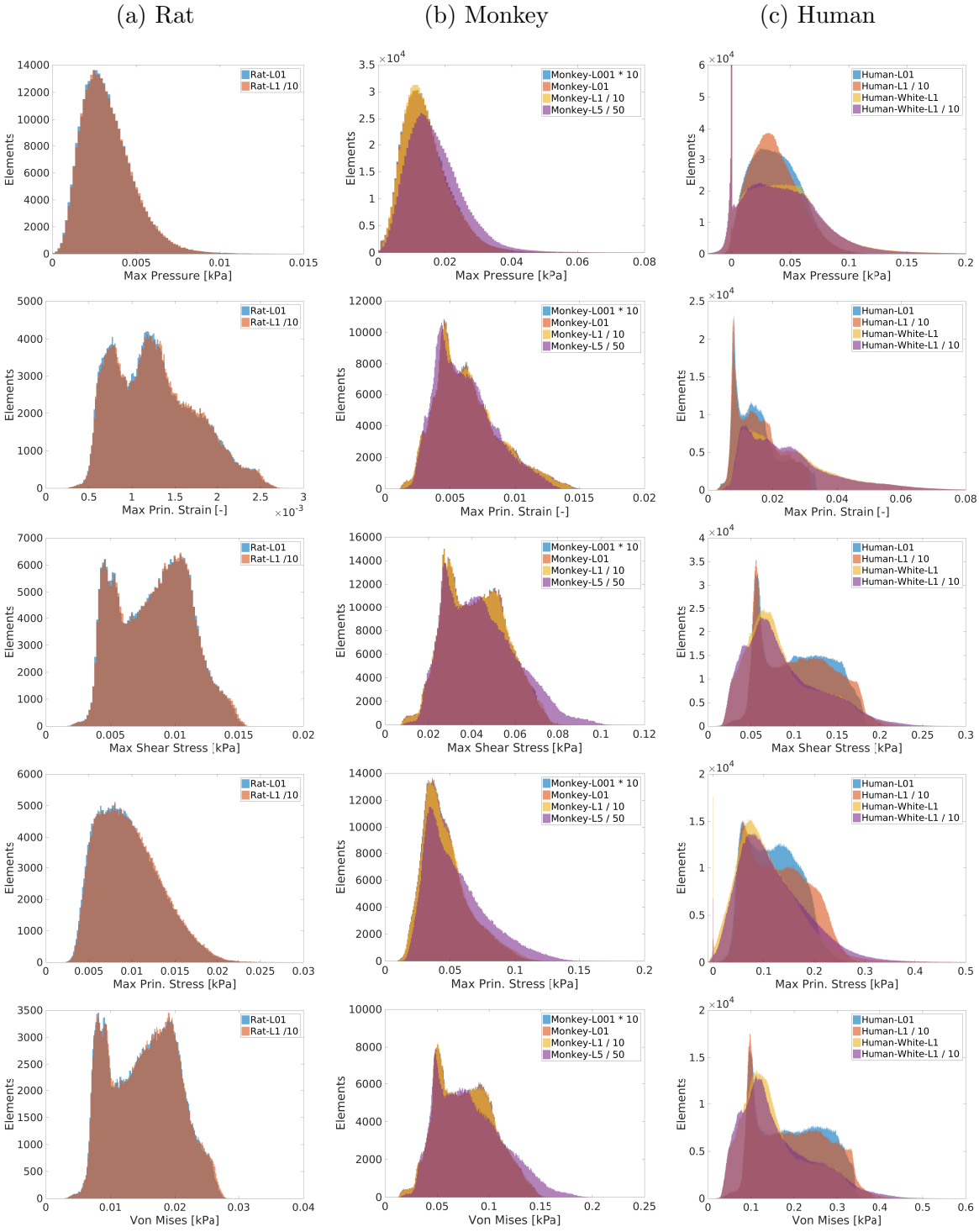

Figure 4.2.1: Maximum accumulated values for all geometries of each load rate. (a) Two cases for the rat are shown, for velocities -0.1 and -1.0 [m/s] (b) Monkey brain with four simulations, with variation of the initial velocities. (c) Four models for the human brain, two for each velocity incorporating the white matter heterogeneity.

Table 4.2.3: Average relative differences of the initial velocity change.

case	*Max. Pressure*	*Max. Principal Strain*	*Maximum Shear Stress*	*Max. Principal Stress*	
Rat	0.1 vs 1	-0.93%	-0.58%	-0.39%	1.24%
Monkey	0.01 vs 1	0.52%	0.20%	-0.24%	-1.96%
	0.1 vs 1	0.34%	0.17%	-0.24%	1.82%
	5 vs 1	18.65%	-2.70%	5.98%	15.58%
Human	0.1 vs 1	2.72%	0.05%	-1.24%	-9.19%
	0.1wh vs 1wh	3.01%	0.72%	-2.41%	-9.41%
	0.1 vs 0.1wh	-14.97%	-37.51%	21.16%	10.24%

4.2.3 Influence of the CSF Modeling

The Cerebrospinal Fluid is the part of the mammal head that cushions the brain against sudden movements, therefore its modeling is one of the most important in our case. As said in subsection 2.3, there is not a defined material for this part, so we test the different models proposed on [22, 65] and the effect that have in the results.

There are different ways of approximating the CSF part, in our case we have five materials defined in table 2.3.1. From the five sets of parameters there are two that never reached the end of the calculation in the monkey mesh.

The Mie-Grüneisen simulation that includes the viscosity term of ($\eta = 0.001$) fails at *30 ms* this is the time limit in the cluster. And comparing it up to this point with the non-viscous, it is seen that do not exist any difference in the results. The viscosity effects in the Mie-Grüneisen material will be discarded from now on.

For the analysis, a soft almost-incompressible linear material "CSF-Line2" is used, in order to test if the movement of the brain inside the skull is possible. The model failed at *35 ms* because the mesh was distorting too much. The interesting part of this analysis is that while some external load was applied the mesh was not deforming and was keeping a constant time step. But after reaching the $v_{ext} = 0\ m/s$ the time step dropped until failure. This particular behavior lets us understand that for very soft materials the stress waves are more dangerous after the load is applied.

There are, three models that reached the end of the calculation, the CSF-Mieg without viscosity, the non-linear elastic material considering it less compressible than the brain, and finally a linear elastic material with stiffer Young modulus than the one which failed.

In figure 4.2.2 can be observed that in the rat geometry, the CSF-Mieg and the elastic material have a similar behavior in all the magnitudes, as seen also in table 4.2.4 where this models relative difference is very low. On the other hand, the hyperelastic material consideration has a completely different scale.

In the histograms in figure 4.2.3 the values for the monkey are plotted. All the models have a similar behavior, with the CSF-Mieg and CSF-Line being just sligtly different than the others as can be understood from table 4.2.5.

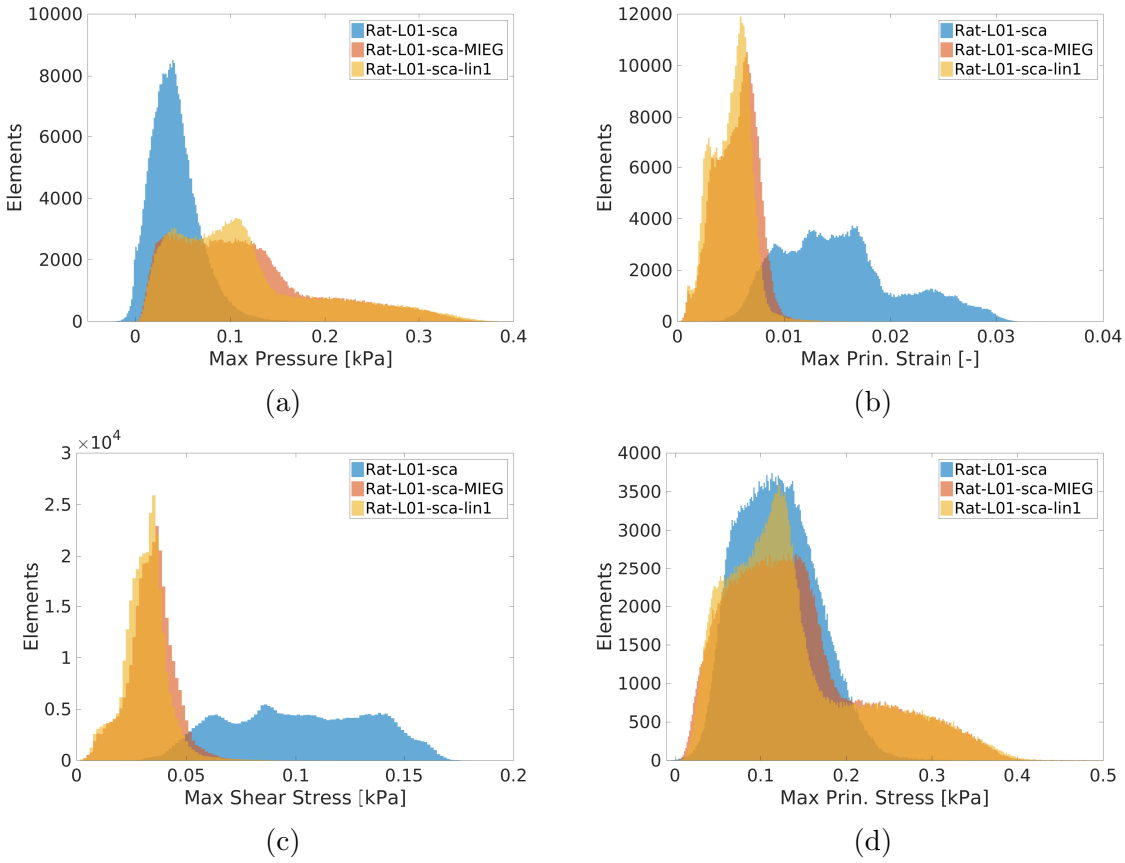

Figure 4.2.2: Maximum accumulated values on the rat geometry varying the material definition of the CSF. In (a) and (c) the values for the Line and MIEG consideration is much higher than the hyperelastic. Meanwhile in (b) and (c) the hyperelastic model have clearly much higher values than the other two.

Table 4.2.4: Average relative differences between the Rat models

case	*Max. Pressure*	*Max. Principal Strain*	*Maximum Shear Stress*	*Max. Principal Stress*
Hype vs lin1	-64.20%	204.52%	223.93%	-14.04%
Hype vs MIEG	-64.53%	177.50%	200.28%	-15.91%
MIEG vi lin1	0.94%	9.74%	7.88%	2.23%

In figure 4.2.4 it is shown a clear difference of behavior in the strain distribution between the CSF-Hype material and the other two cases. Meanwhile the linear and Mie-Grüneisen simulations show a very similar and heterogeneous display, the CSF-Hype keeps an homogeneous form with a continuous variation. On the other hand, figure 4.2.5 shows that for the principal stresses the behavior of all the models is the same but in the CSF-Hype case a contra-coup appears in the other side of the brain and the magnitude of the values is lower.

A behavior similar to the rat is observed in the monkey in figure 4.2.6, where the

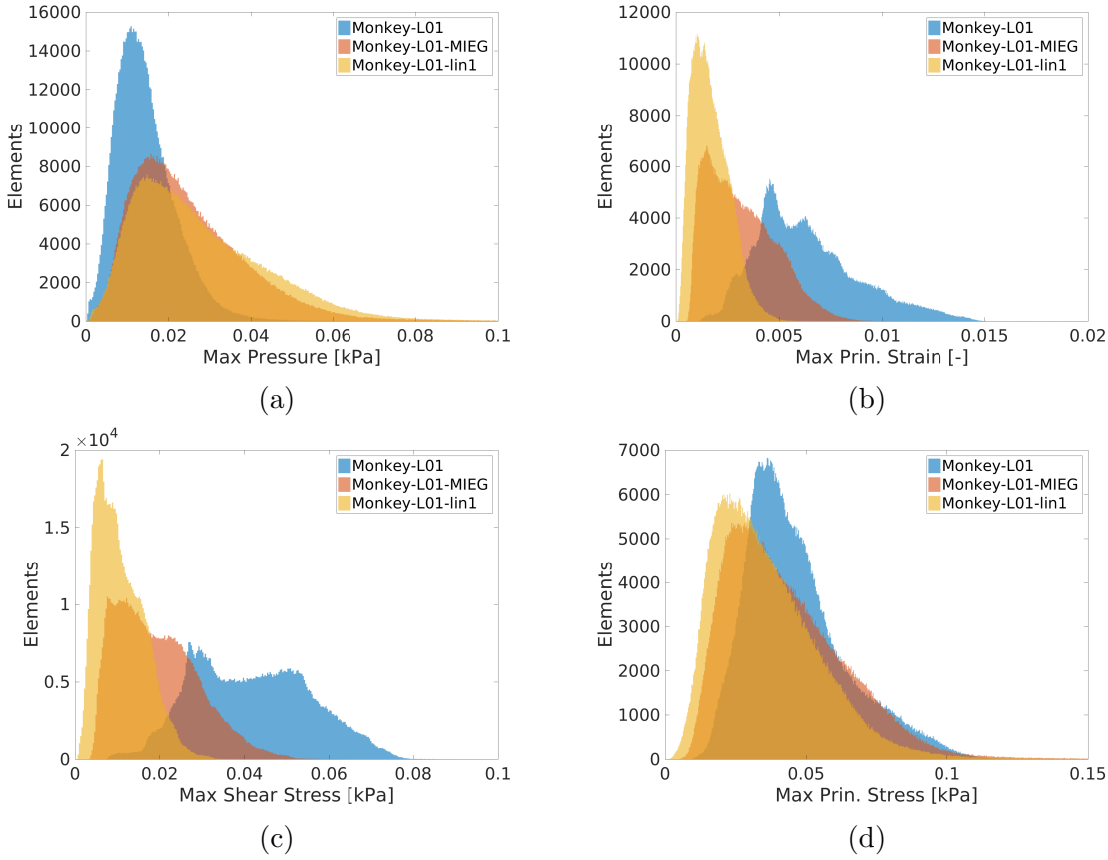

Figure 4.2.3: Maximum accumulated values varying the material definition of the CSF in the monkey. In (b) and (c) the distributions follow the same style with the CSF-Line having the lower values and the Hype the highest, while in (d) the distributions have the same behavior.

Table 4.2.5: Average relative differences between the monkey models

case	*Max. Pressure*	*Max. Principal Strain*	*Maximum Shear Stress*	*Max. Principal Stress*
Hype vs lin1	-47.92%	272.36%	286.76%	29.26%
Hype vs MIEG	-42.94%	100.38%	115.69%	8.24%
MIEG vi lin1	-8.7%	85.82%	79.32%	19.42%

CSF-Mieg and Line models have a heterogeneity with the same pints of strain concentrations while the CSF-Hype have a more homogeneous characterization. Regarding the Principal stresses in figure 4.2.7, both CSF-Line and CSF-Mieg have again a close distribution but in this case the last model (c) has a symmetric character while (b) only has it on one side. For the CSF-Hype, the observation is the same as homogeneous shape emulating the other models.

To see the behavior over time of the models, a set of 7 points for the rat and 9 for the

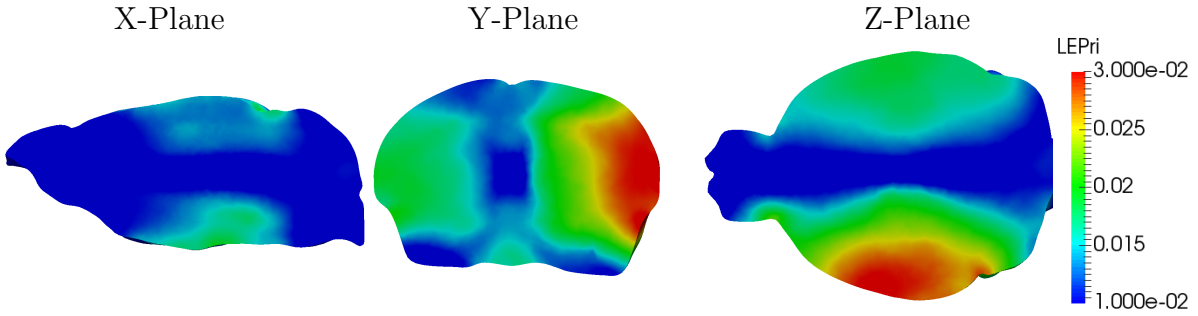

(a) Maximum principal strain [-]
Rat-L01-scaled with CSF-Hyper

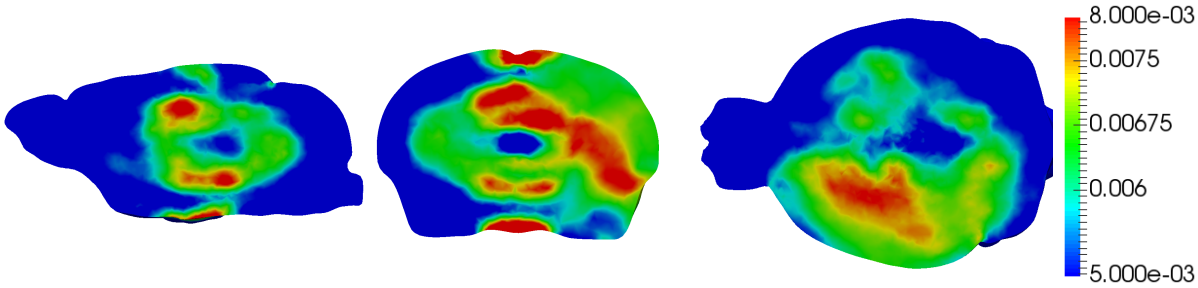

(b) Maximum principal strain [-]
Rat-L01-scaled with CSF-Lin1

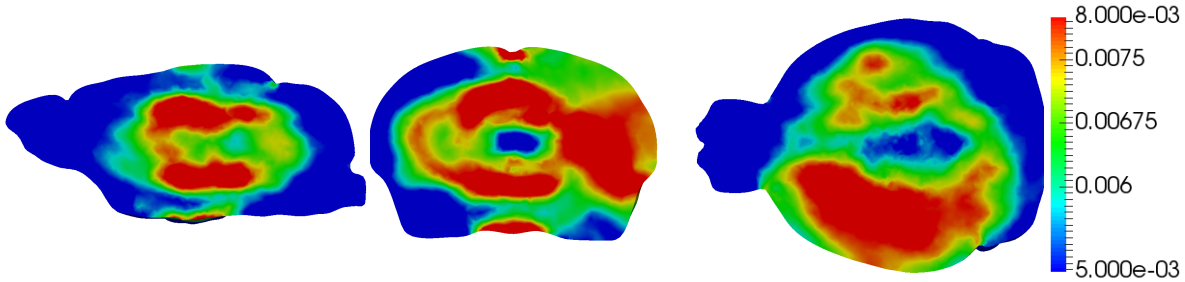

(c) Maximum principal strain [-]
Rat-L01-scaled with CSF-Mieg

Figure 4.2.4: Max. Accumulated Principal Strains in the rat scaled to have the mass of the human, (b) and (c) have a similar shape and magnitude while (a) seems to capture a contra-coup, that is a concentration of strains in the opposite side of the load.

monkey taken on each corner of the brain matter is used. For their representation, the mean value of all the points over time together with the variance is presented in figures 4.2.9 and 4.2.8.

Comparing figures 4.2.8 and 4.2.9, it can be seen that while in the monkey the CSF-Hype model reaches its maximum before the end of the load, the rat reaches its maximum after it. Another characteristic is that on the rat, the CSF-Line and the CSF-Mieg material have a much closer behavior than the monkey, this is probably because it do not have foldings on its surface, phenomena that will be studied a posteriori, it is also easy to notice that the rat have much less waves than the monkey, probably because the rat is scaled to have human mass ans thus is much bigger.

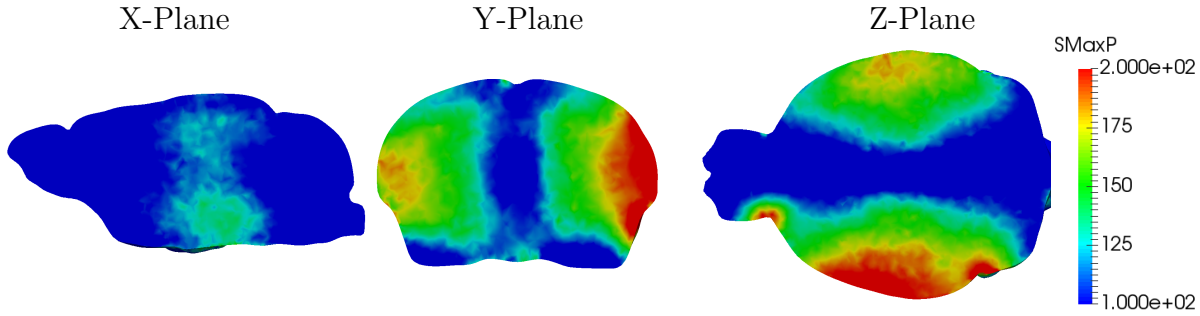

(a) Maximum principapal stress [kPa]
Rat-scaled-L01 with CSF-Hype

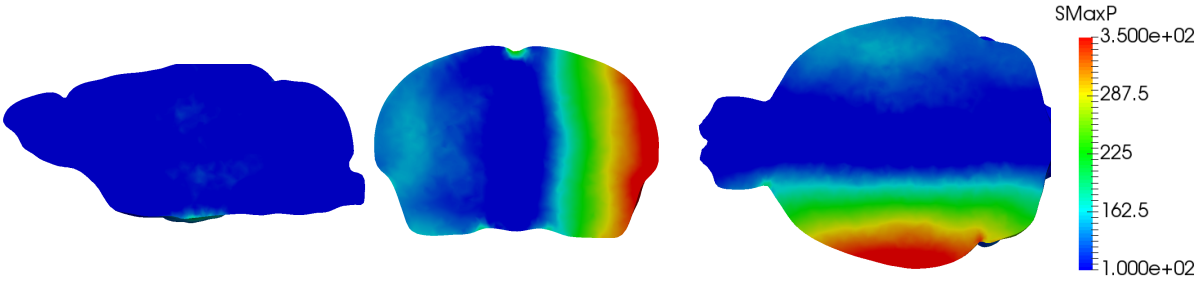

(b) Maximum principapal stress [kPa]
Rat-L01-scaled with CSF-Lin1

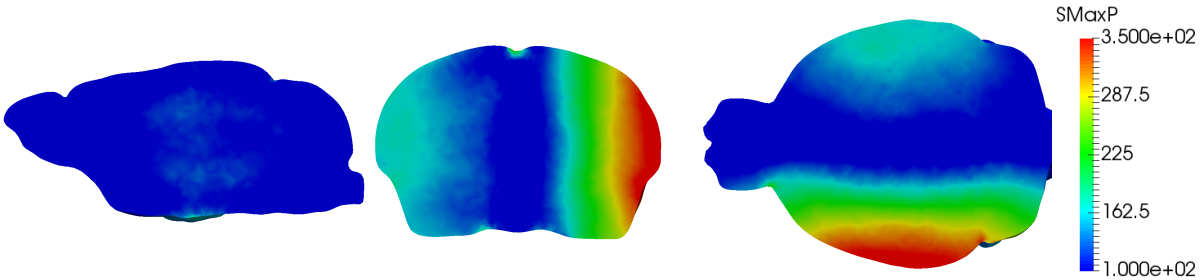

(c) Maximum principapal stress [kPa]
Rat-L01-scaled with CSF-Mieg

Figure 4.2.5: Maximum Accumulated Principal Stresses in the rat scaled to have the mass of the human. In parts (b) and (c) the distribution is the same, having (a) indicating a contra-coup, that is a concentration of stresses on the opposite part of the loading

.

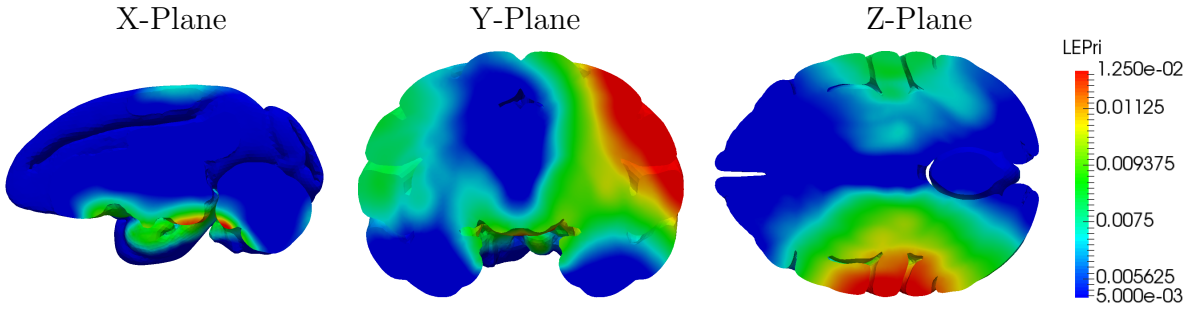

(a) Maximum principal strain [-]
Monkey-L01 with CSF-Hype

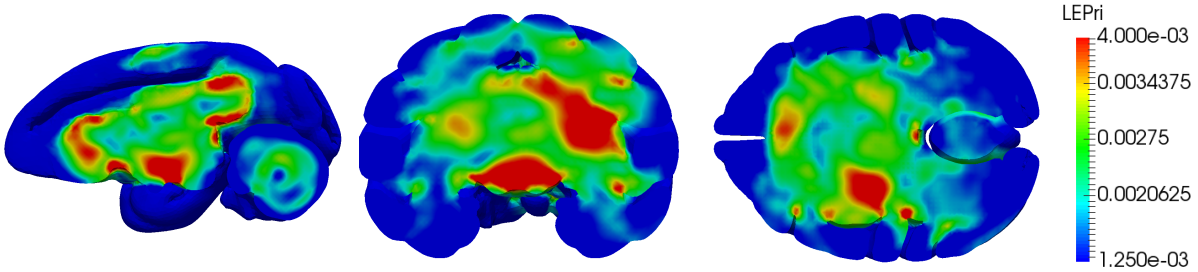

(b) Maximum principal strain [-]
Monkey-L01 with CSF-Lin1

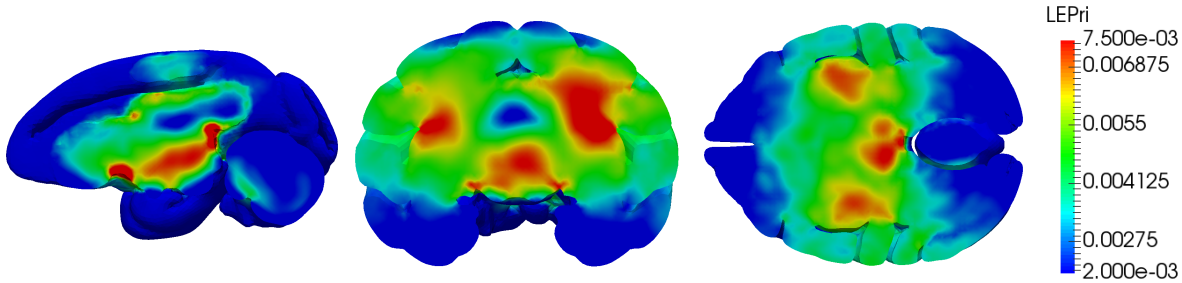

(c) Maximum principal strain [-]
Monkey-L01 with CSF-Mieg

Figure 4.2.6: Max. Accumulated Principal Strains in the monkey brain. Notice that all models have different magnitudes in the legend. In this figure (b) and (c) have a similar behavior even if the Mieg material seems more symmetric and the Line have more concentrations in one side. On (a) it is depicted with a clear concentrations of strains in one side.

.

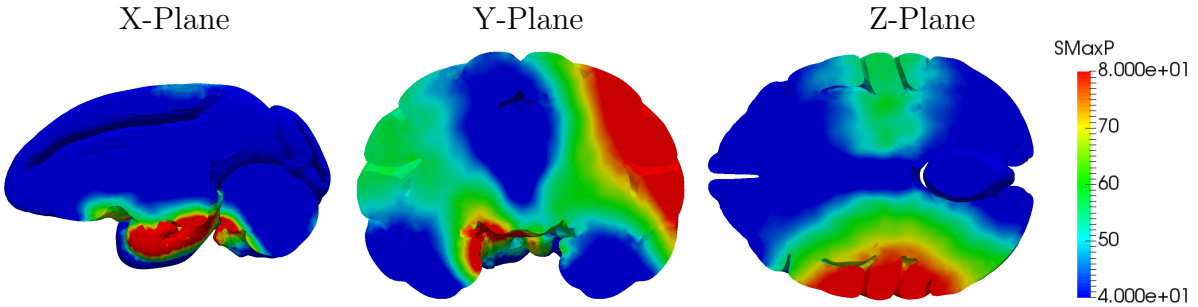

(a) Maximum principal stresses [kPa]
Monkey-L01 with CSF-Hype

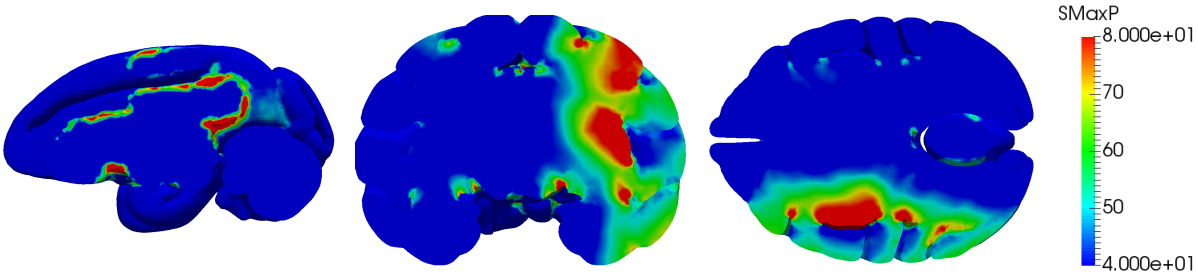

(b) Maximum principal stresses [kPa]
Monkey-L01 with CSF-Lin1

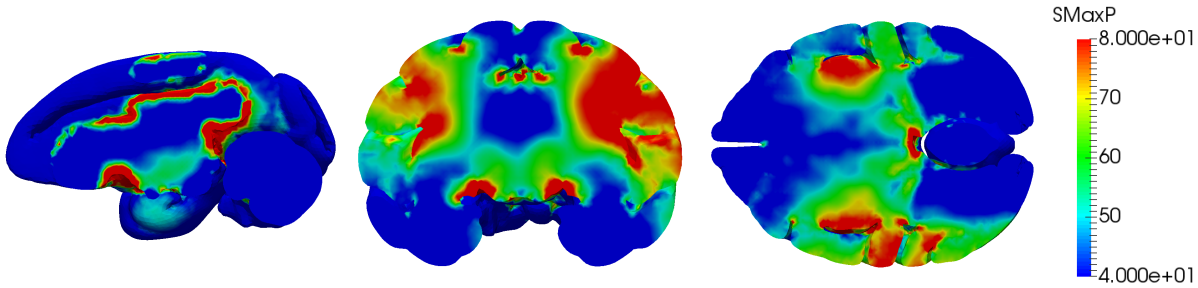

(c) Maximum principal stresses [kPa]
Monkey-L01 with CSF-Mieg

Figure 4.2.7: Maximum Accumulated Principal Stresses on the monkey brain. With all the ouputs having the same magnitude, it is seen how in figures (a) and (b) the stresses are clearly concentrated in the loading side, meanwhile in (c) have a more symmetric behavior. At the same time (b) and (c) have a heterogeneous distribution while (a) having a more homogeneous shape.

.

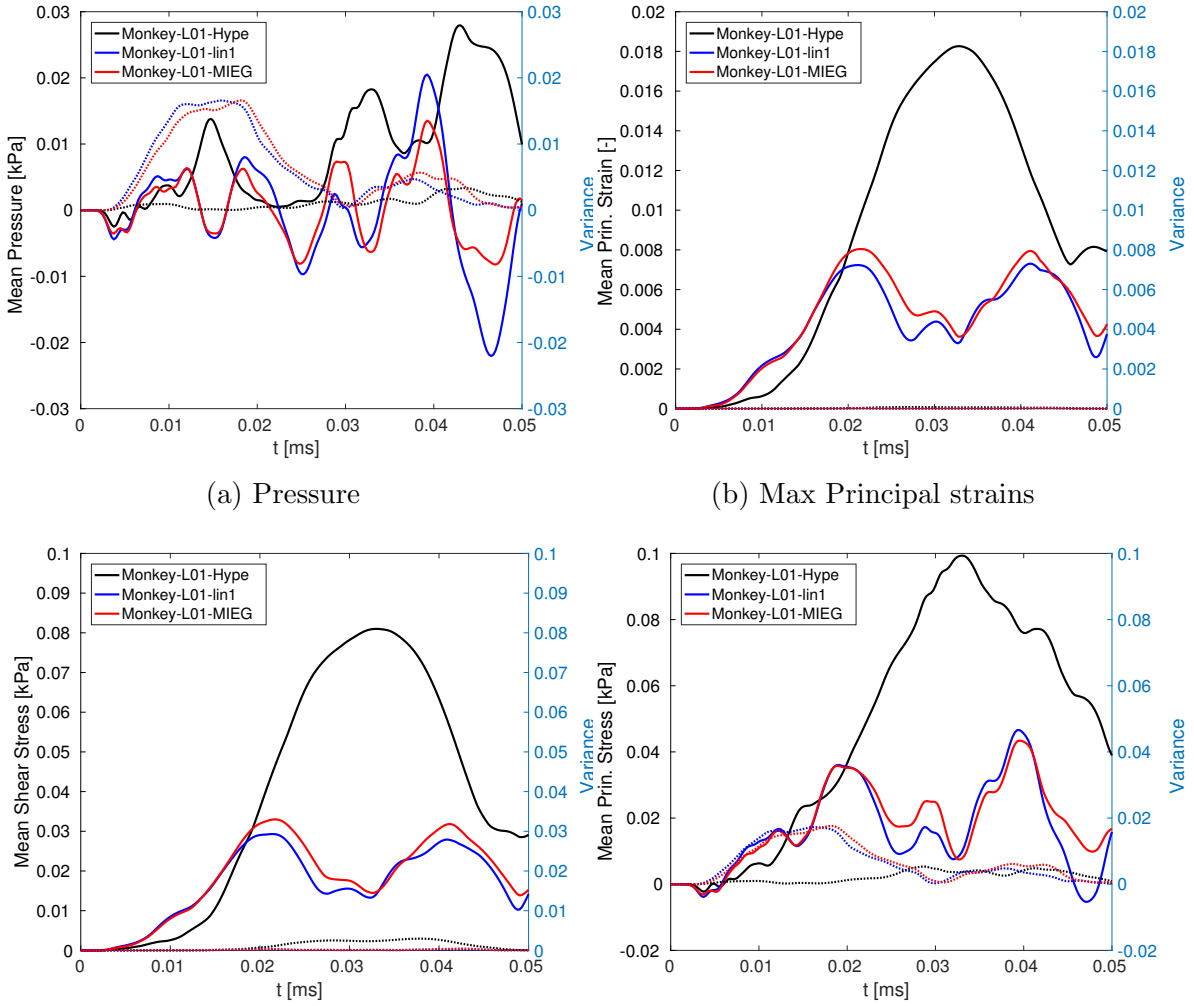

(a) Pressure

(b) Max Principal strains

(c) Max Shear Stress

(d) Max Principal Stresses

Figure 4.2.8: Average time histogram of the representative points in the rat. the pressures in (a) have a high variance while the load is still active (before 25ms) but after this time the values get in accordance. For the Principal strains, stresses and the max shear stress in (b),(c), and (d) we can see that the higher value of the Hype model appears also after the application of the load, having until some point the same shape as the other models.

.

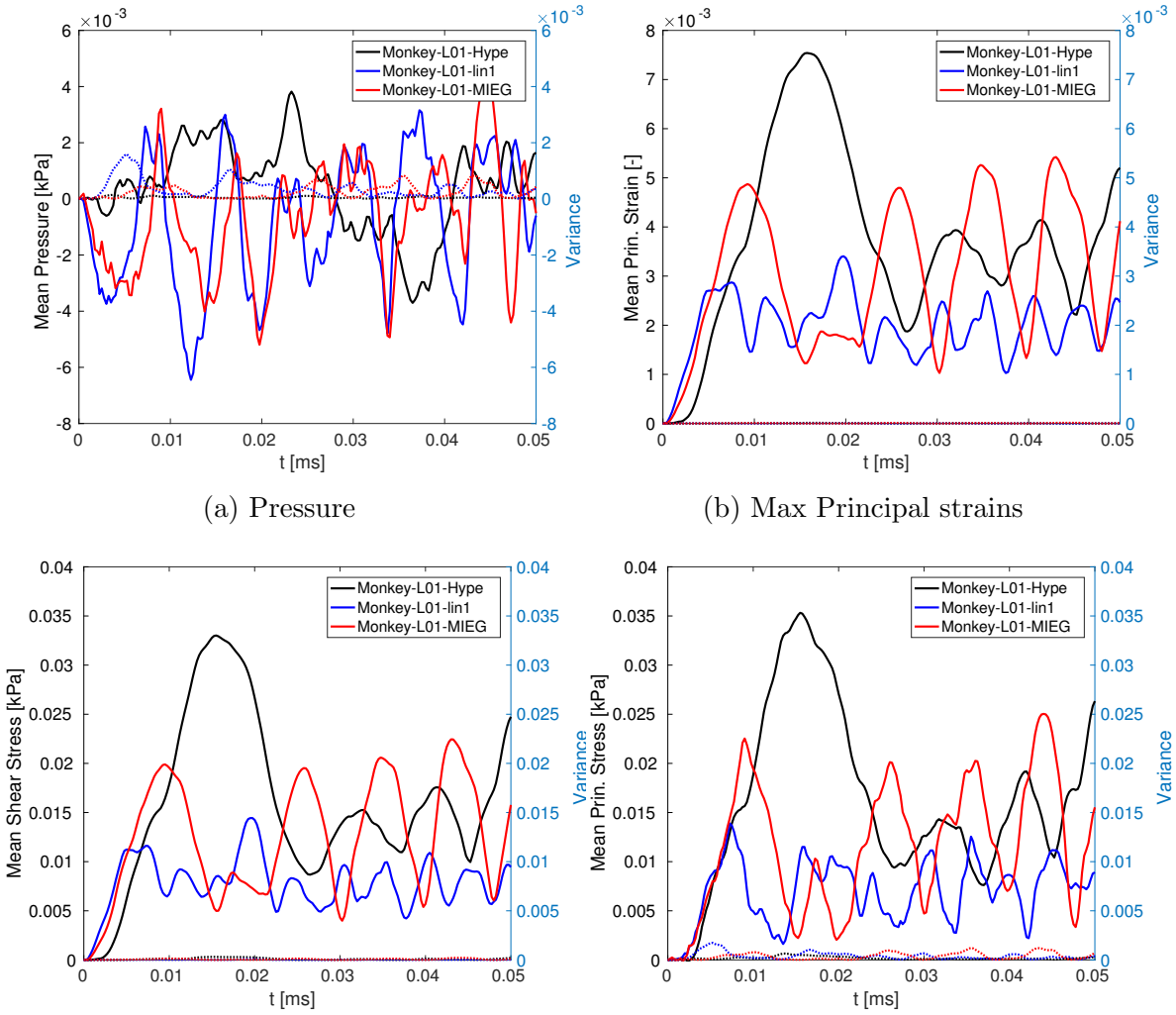

(a) Pressure

(b) Max Principal strains

(c) Max Shear Stress

(d) Max Principal Stresses

Figure 4.2.9: Average time histogram of the representative points in the monkey. Even if its not easy to extract information form the pressures in (a), it is clearly seen that the behavior of the other outputs is similar. All the maxims in the models are located in the first half of the time, and the model with less variation of the outputs is the Line.

4.2.4 Analysis of the load direction

In this subsection, the effects of the load direction will be studied. We will understand by lateral loading an impact on the side of the head, and by frontal loading an impact along the longitudinal direction.

In figure 4.2.10 a set of histograms depicts the distribution along the different loading directions. For the monkey (b), there is a concordance of the results, and it is observed that it has the sides more similar than the rat (a). In the case of the human (c) there are similarities on the shape in the models with homogeneity and heterogeneity between themselves, especially for the one that includes the white matter. But not

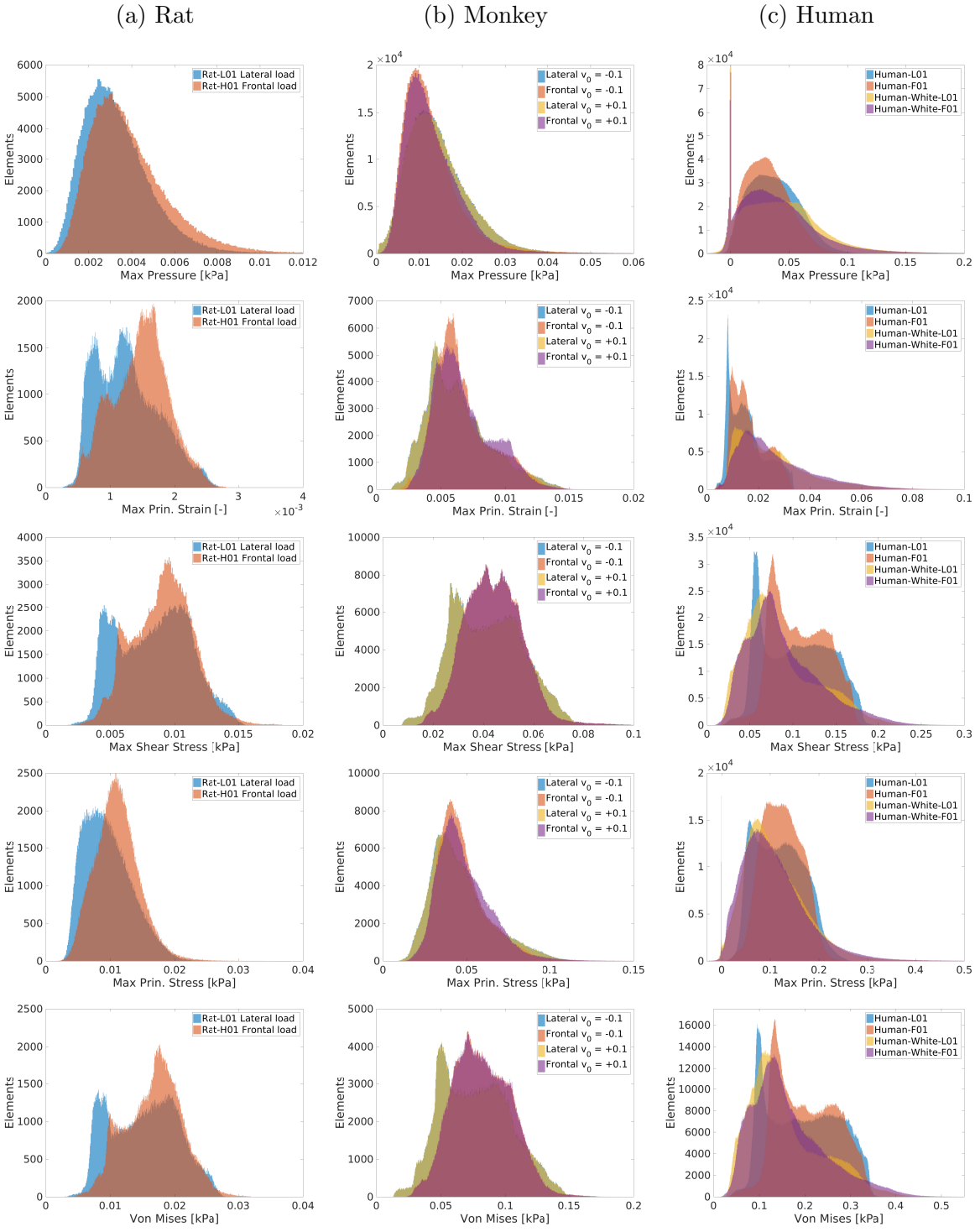

Figure 4.2.10: Histogram of the maximum accumulated values of all the geometries in each direction. For the rat and human a frontal-lateral regime is considered and for the monkey is added the effect of the sense of both directions. For the human is also taken into account adding another material with different properties.

being close enough, it is possible to state that the human head has a clear difference in behavior to the loading direction.

For the study is also taken into account the use of the CSF-Line in the monkey brain in figure 4.2.11. It is seen that for the CSF-Line model the relevance loading sense in the lateral direction is again not so important, but in this case a shallow difference on the longitudinal direction appears

In figures 4.2.11 it is taken into account if the velocity of the load is positive or negative, and in 4.2.10 b) it is observed that the variance that occurs if the load comes from one side or the other is practically zero. In frontal velocity, the difference is small also but a bit higher. This is logical because the geometry varies more in the longitudinal direction than in the transversal one. All this can be corroborated in table 4.2.6, where the relative differences between the models are displayed.

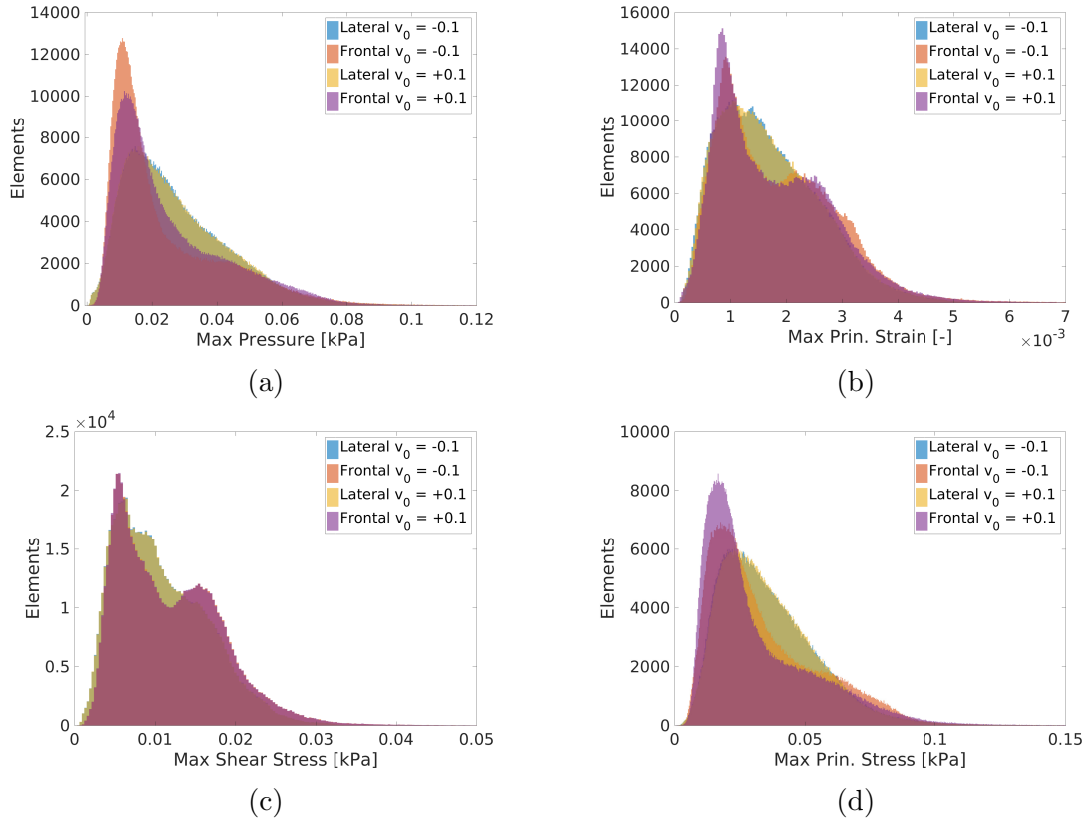

Figure 4.2.11: Histograms in the monkey of the maximum accumulated values varying the direction using the linear material for the CSF. Even if its not so clear to see, for all graphics the Lateral $v_0 = -0.1$ and $v_0 = +0.1$ give exactly the same outputs, while there is come discordance between the frontal loadings.

In figures 4.2.13 - 4.2.17 can be observed how the load is distributed along different areas. As said before, even if the difference in the magnitude of the values is not so much, the stressed areas change being similar between different species.

Table 4.2.6: Average relative differences between all the simulations considering CSF-Hyper. For the Monkey brain the "b" means that the velocity changes its sense a thus the load is applied form the other side. And the "wh" in the human means that this model has included the white matter.

	case	*Max. Pressure*	*Max. Principal Strain*	*Maximum Shear Stress*	*Max. Principal Stress*
Rat	L-F	17.97%	15.26%	8.00%	15.06%
Monkey	L-F	-11.00%	4.90%	5.50%	1.49%
	L-Lb	0.07%	0.07%	0.01%	-0.02%
	F-Fb	-1.29%	-1.73%	0.03%	-2.35%
Human	L-F	17.02%	-5.11%	-3.01%	-3.86%
	Lwh-Fwh	7.68%	-5.52%	-3.96%	-0.30%
	L-Lwh	-14.97%	-37.51%	21.16%	10.24%
	F-Fwh	-21.76%	-37.78%	19.98%	14.32%

Table 4.2.7: Average relative differences between models considering CSF-Line.

	case	*Max. Pressure*	*Max. Principal Strain*	*Maximum Shear Stress*	*Max. Principal Stress*
Monkey	L-F	14.89%	-7.37%	-8.97%	4.77%
(CSF-lin)	L-Lb	-0.11%	-0.28%	-0.17%	-0.21%
	F-Fb	-5.74%	2.85%	0.13%	7.27%

Notice that in tables 4.2.6 and 4.2.7, "L-F" means a comparison between the lateral and frontal loading, while involving "b" means a load coming from the back, i.e. "L-Lb" is the relative difference between the lateral loading and the one coming from the other side of the brain and "F-Fb" is the frontal versus the back impacts.

Looking at the figures it is clear that for the bigger mammals there is a clear passing of the strains and stresses from the base union of the head, no matter how the load is. Meanwhile the rat distribution of strains in the head has a simpler behavior.

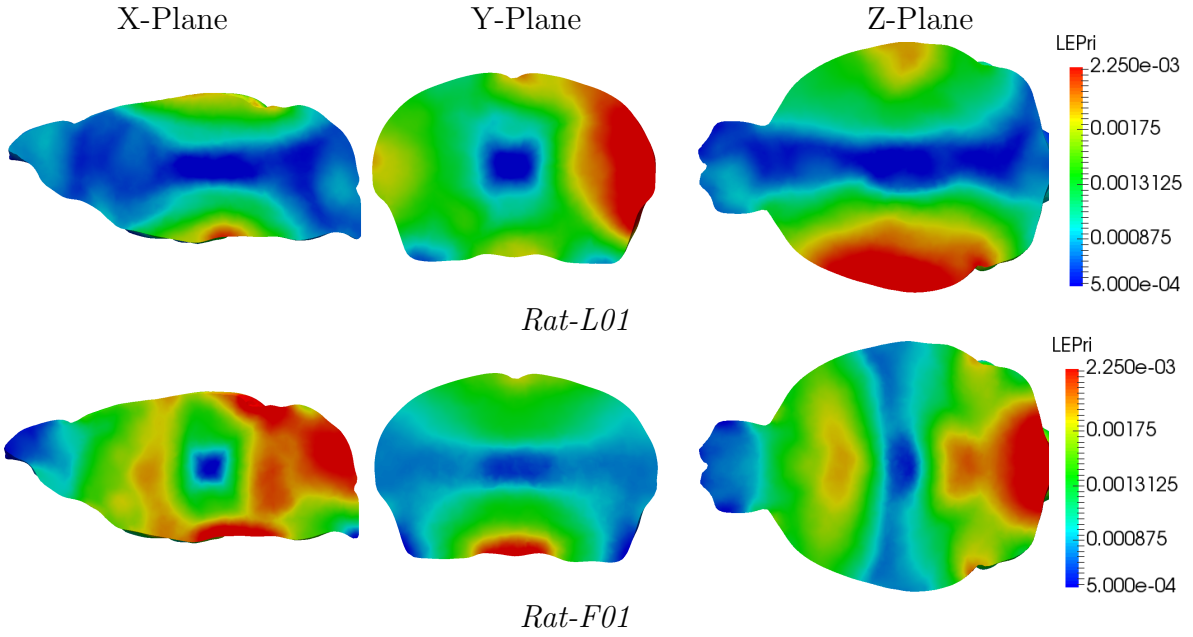

Figure 4.2.12: Maximum Accumulated Principal Strains for the rat geometry. Is it observed also that keeping the magnitude of the values constant, the main difference between the first row ant the second is the orientation of the outputs.

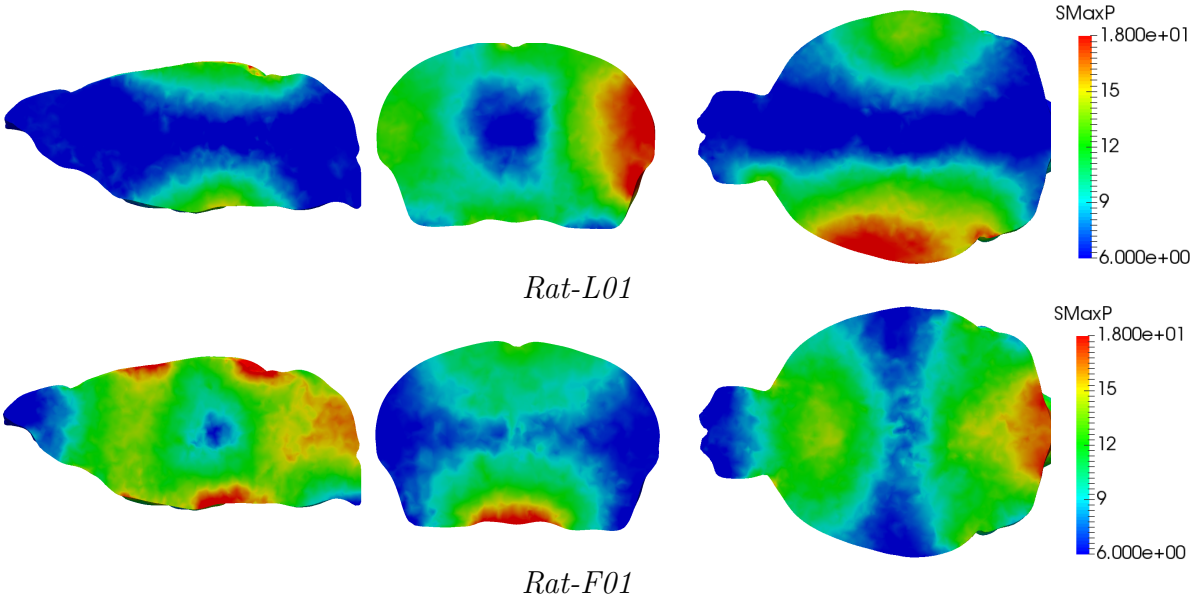

Figure 4.2.13: In the case of the Maximum Accumulated Principal Stresses for the rat, the magnitude of the outputs is kept the same with the only difference in the direction.

.

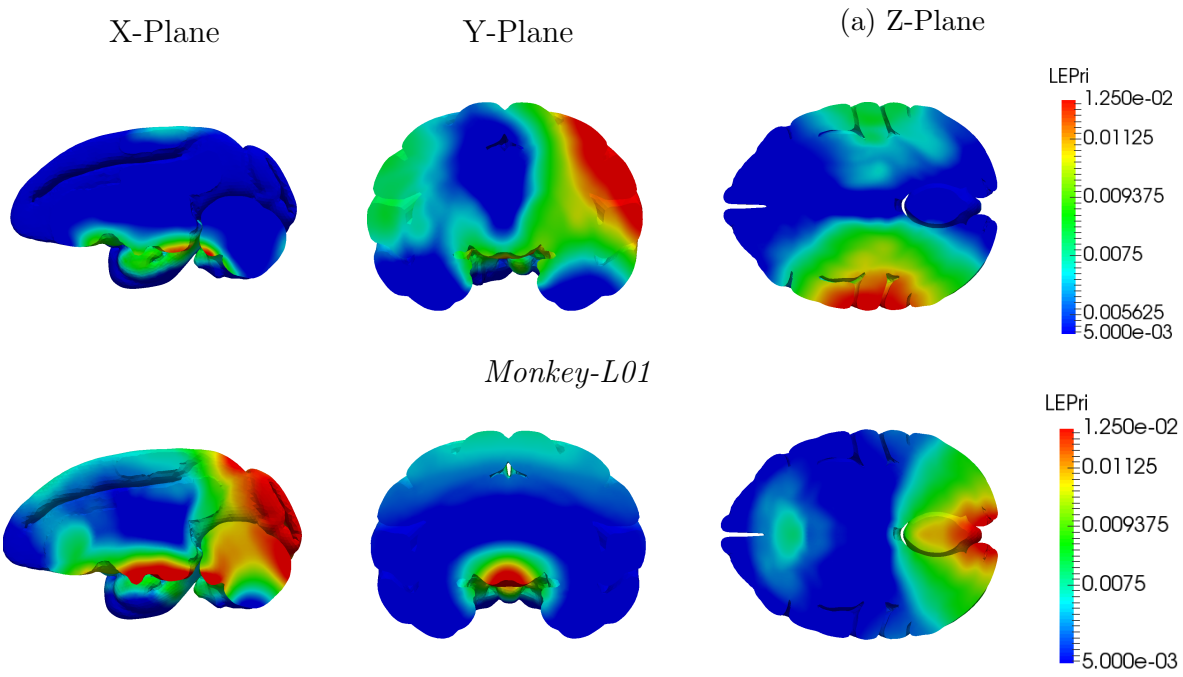

Figure 4.2.14: Maximum Accumulated Principal Strains, in the top row the concentrations are in the side of the brain where the load is applied. In the bottom row not only the side where the load is applied is highlighted but also there is a distribution in the base.

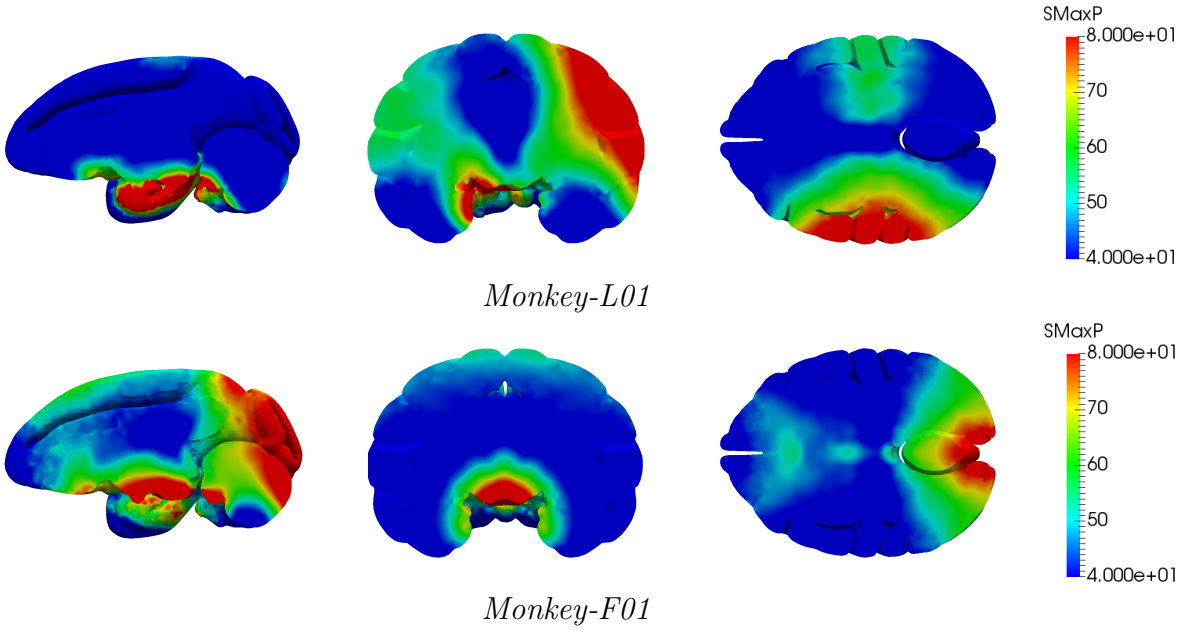

Figure 4.2.15: For the Maximum Accumulated Principal Stresses, the top row with lateral loading have stressed the side of the load, while the bottom row have an impact to the base ob the brain.

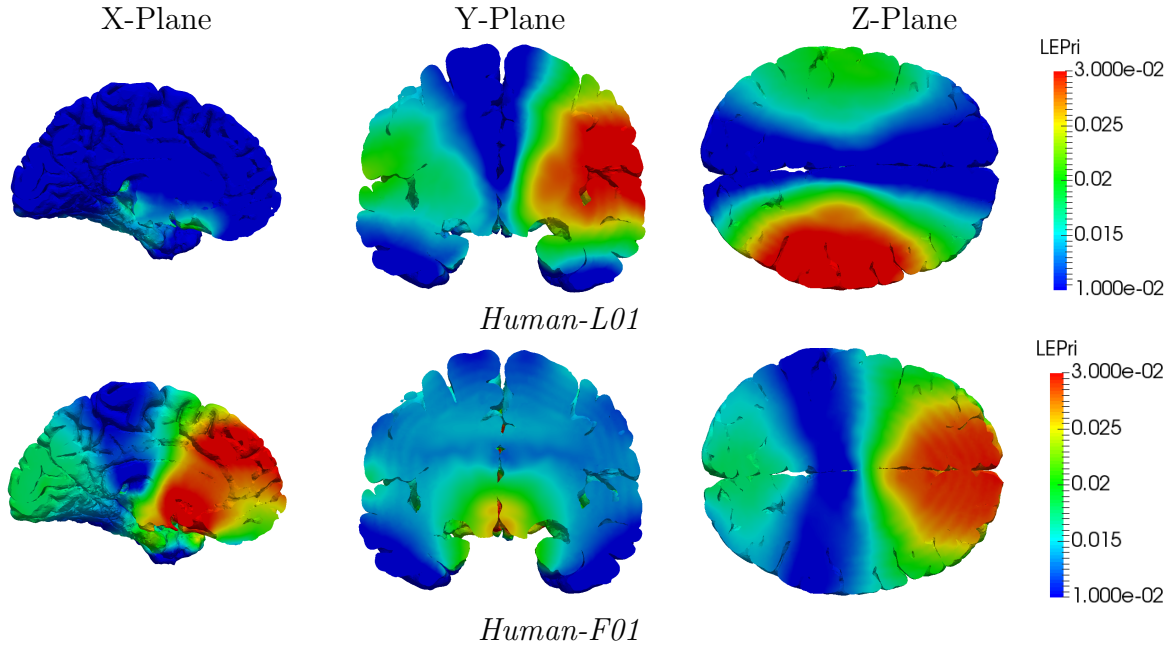

Figure 4.2.16: Maximum Accumulated Principal Strains in the human.

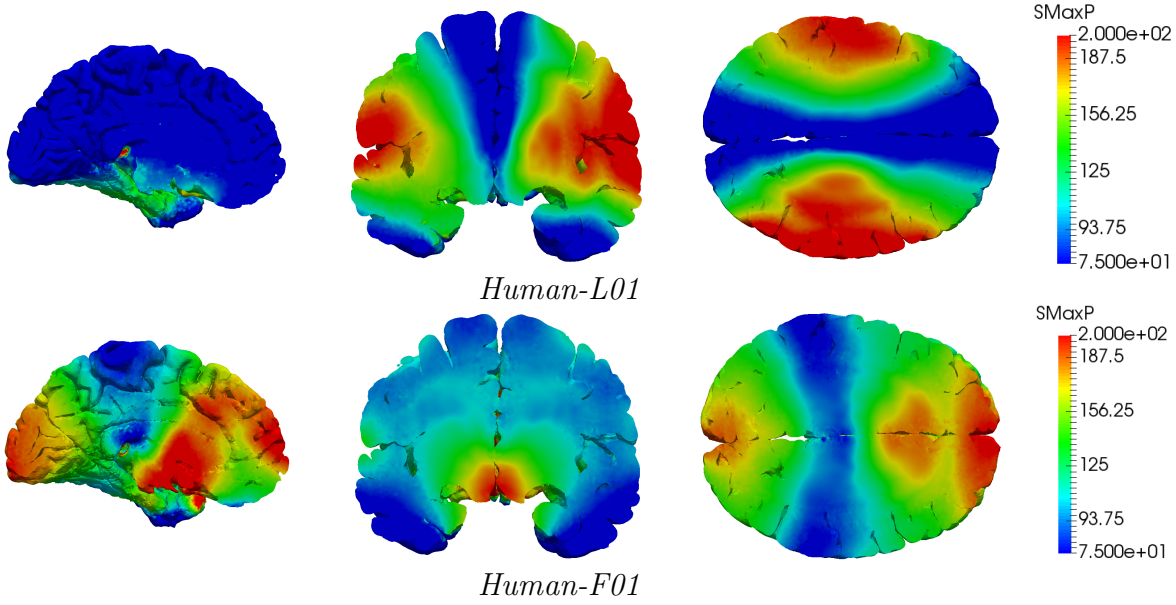

Figure 4.2.17: Maximum Accumulated Principal Stresses in the human brain.

.

4.2.5 Analysis of the Viscoelastic properties

As seen in subsection 2.3.3, three sets of viscoelastic parameters are considered in this document. The first set belongs to Kleiven [33], that we will call "monkey-L01-visc1" and is based on a fitted model with a constant time decay, assuming a long term shear stress. Whereas the second and third are Garimella et al. [22] and Makoshi et al.[38] respectively with names "monkey-L01-visc2" and "monkey-L01-visc3".

In figure 4.2.18, it is shown that the viscous effects of the maximum values of the stresses or pressures in the four models are little or none, having a look at table 4.2.8 we see that the differences are of a maximum of 50% in the pressures and a -26% in the stresses. But the huge decay of the strains is an important feature to be taken into account, specially in the first and third viscous cases. This would be the same considering the CSF-lin1 4.2.19.

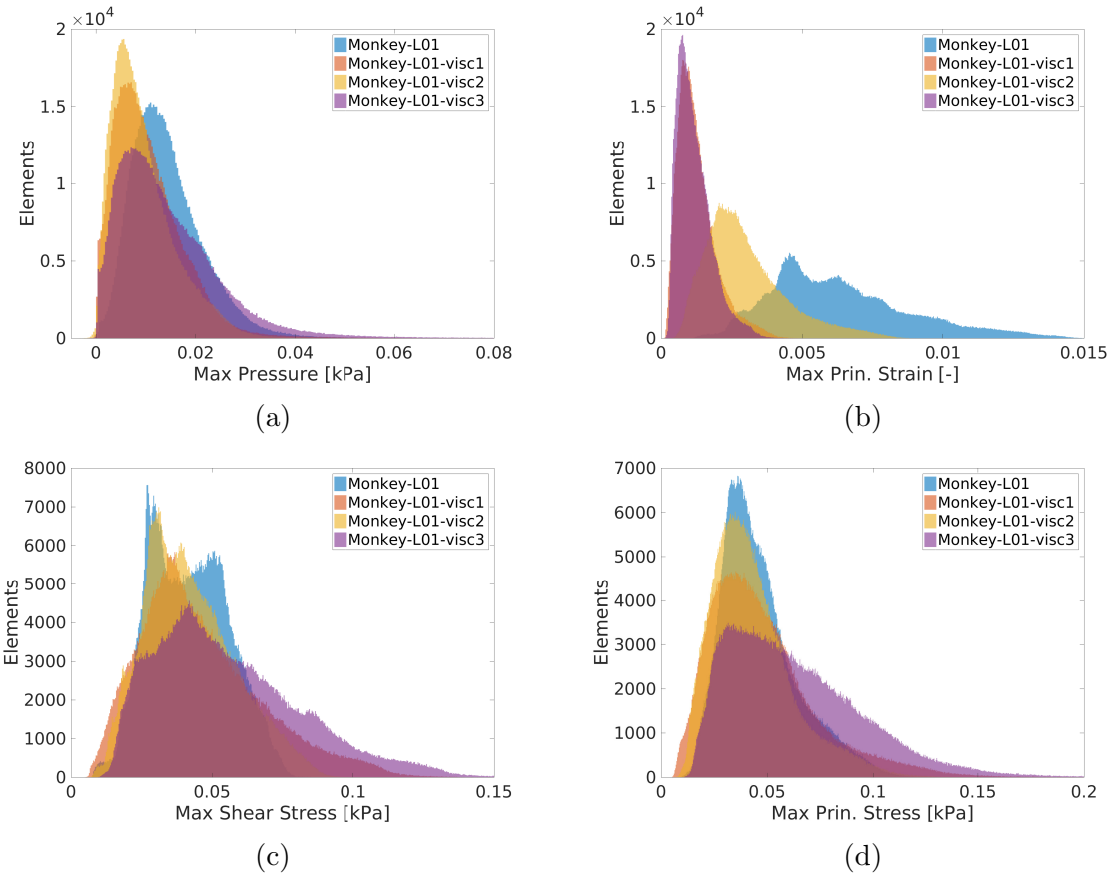

Figure 4.2.18: Maximum accumulated values varying the viscoelastic parameters in the monkey. For the pressures and shear stresses there is no considerable affection of the viscoelastic parameters. On (b) a diminish of the strains is observed upon applying the viscosity having "visc1" and "visc3" the same values. In the middle of them and the non-viscous model there is found the "visc2".

Figures 4.2.20 - 4.2.21 show the Max Principal Strains and pressures respectively. We

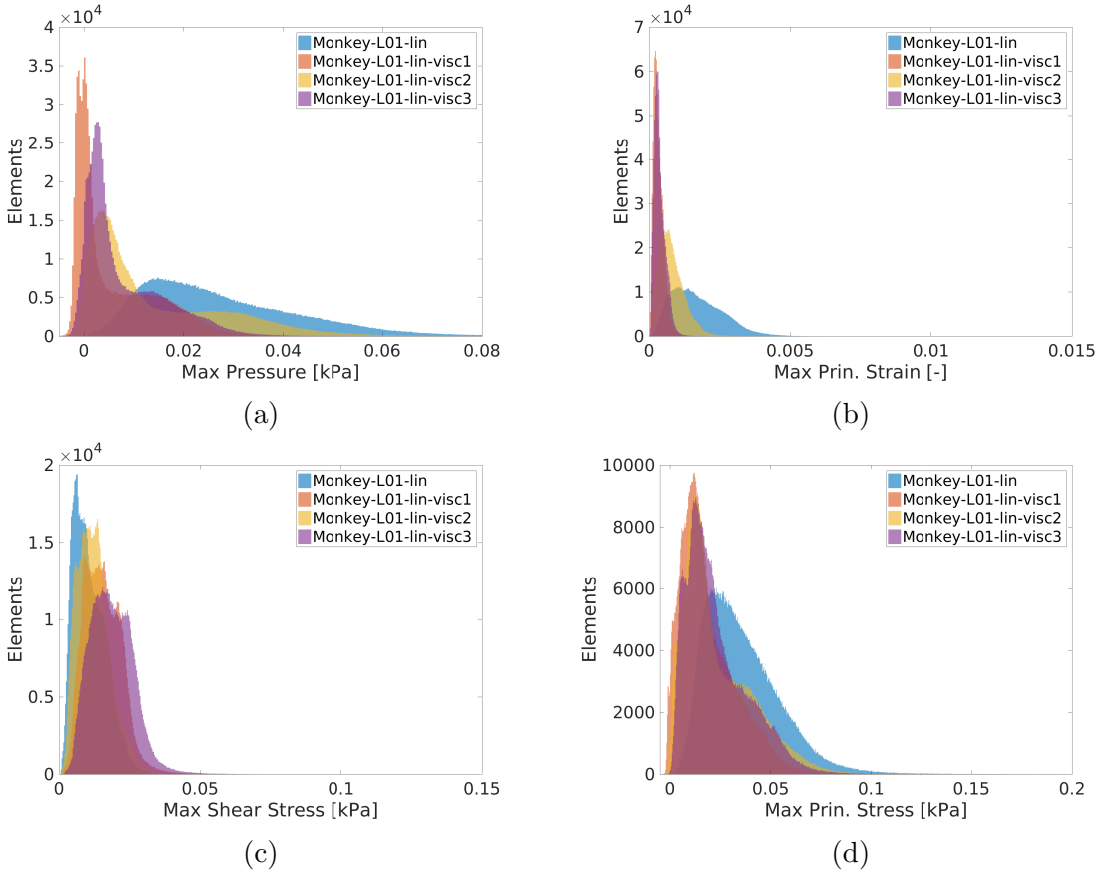

Figure 4.2.19: Maximum accumulated values varying the viscoelastic parameters of the monkey brain with CSF-lin1. In (a) the pressures of all the viscous models have a similar shape varying the magnitudes, for the principal stretches we observe that are reduced in the models which uses viscosity. For (c) and (d) the behavior of all the models is similar.

Table 4.2.8: Average relative differences between models

case	*Max. Pressure*	*Max. Principal Strain*	*Maximum Shear Stress*	*Max. Principal Stress*
no visco vs visc1	37.33%	399.80%	-9.12%	-2.72%
no visco vs visc2	50.82%	112.30%	-0.58%	8.16%
no visco vs visc3	0.40%	439.18%	-25.12%	-26.67%

can see that the overall behavior of the strain distribution does not change between the studied models, without considering the difference in numerical values.

Regarding the pressures, a similar conclusion as in the strains can be observed, but in these cases it can also be noticed that even if the affection in the numerical values is relatively low, is interesting to see how the high continuity of the distribution is lost and how some new isolated concentration areas appear around the foldings. At the

Table 4.2.9: Average relative differences between models

case	*Max. Pressure*	*Max. Principal Strain*	*Maximum Shear Stress*	*Max. Principal Stress*
no visco vs visc1	367.23%	408.22%	-30.33%	92.02%
no visco vs visc2	94.65%	112.58%	-12.54%	51.23%
no visco vs visc3	248.81%	351.03%	-42.17%	55.27%

same time we can see that the values on the areas far from the exterior boundary of the brain decrease softening the relative differences making up for the higher values. Also, between the first and the third viscous models it is seen that the response is the closest being almost equal while the second viscous model is a halfway between the model without viscosity and the other models.

And once we start looking at the time behavior, even if it is hard to see, in the viscous models we have more stable pressure and principal strains, but in the shear or principal stresses, where the third viscous model closely followed by the first has a huge variance over time especially when $v_{ext} = 0m/s$.

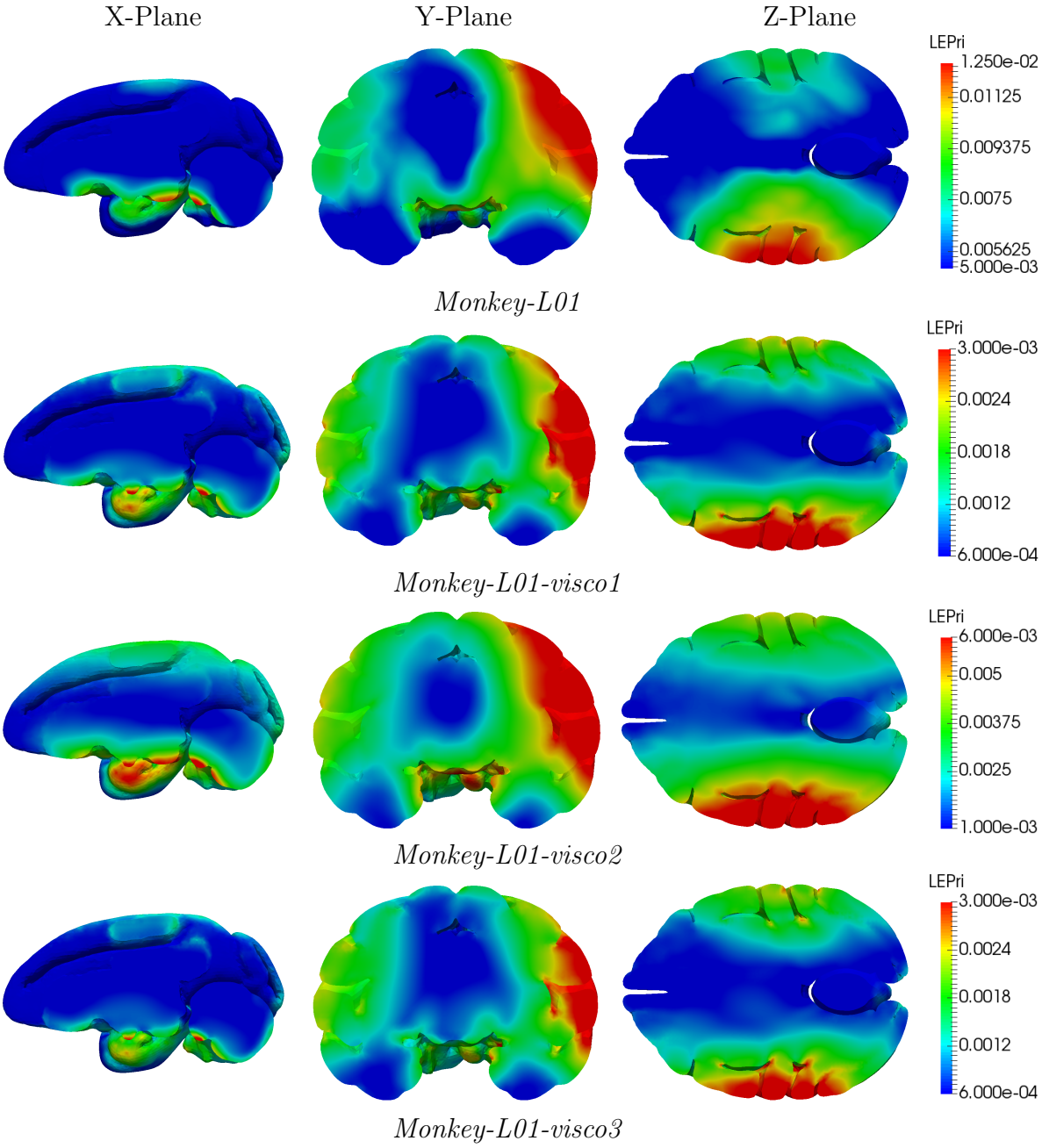

Figure 4.2.20: Maximum Accumulated Principal strains for the monkey geometry. There is no major difference on the distribution of the models mainly changing the magnitude of the strains.

.

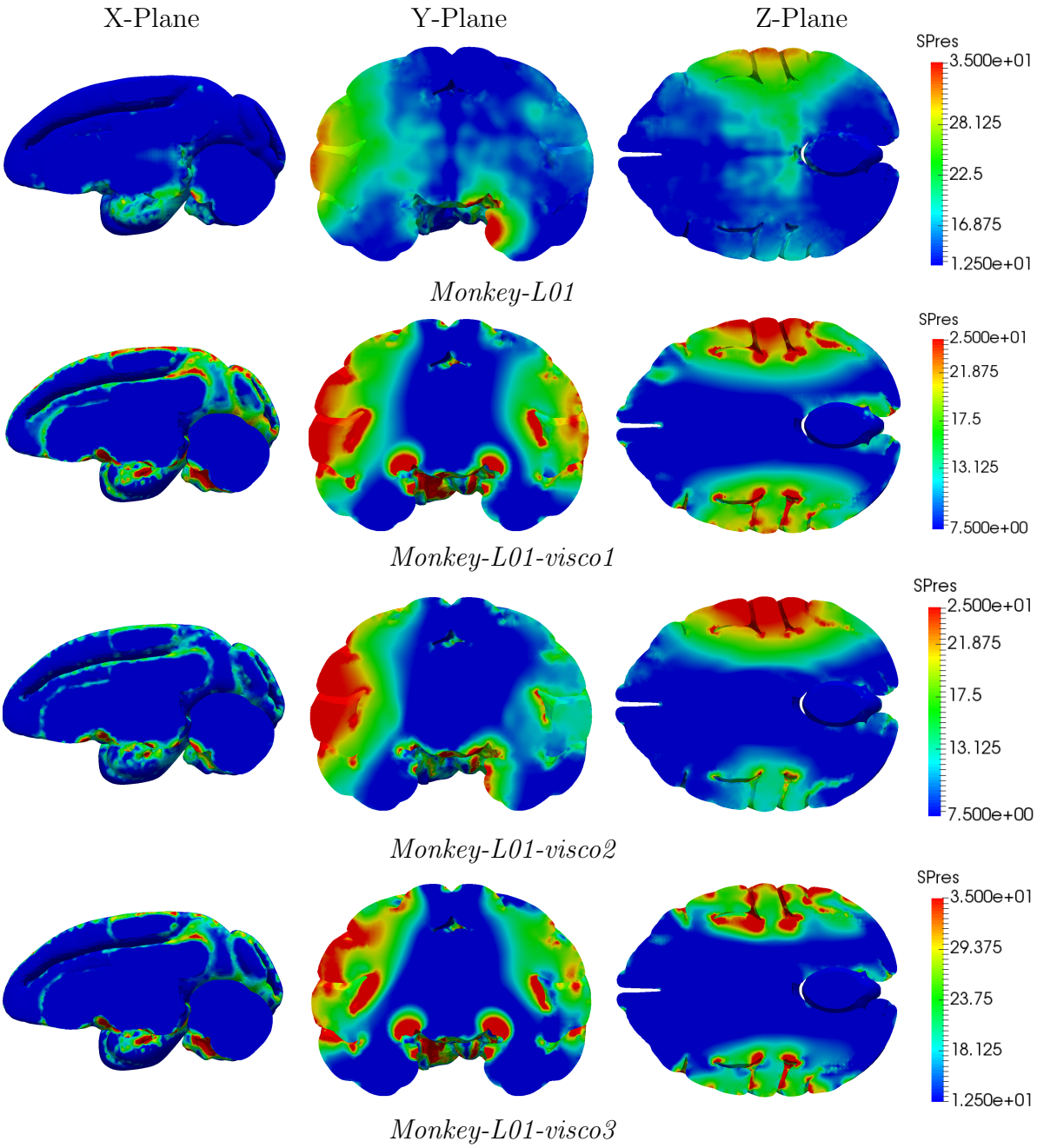

Figure 4.2.21: Maximum Accumulated Pressures in the monkey brain for different viscous models. Around the foldings it is observed in all the viscous models that some arbitrary concentration of stresses appears, especially in the second and fourth rows and on a smaller scale also in the third row.

.

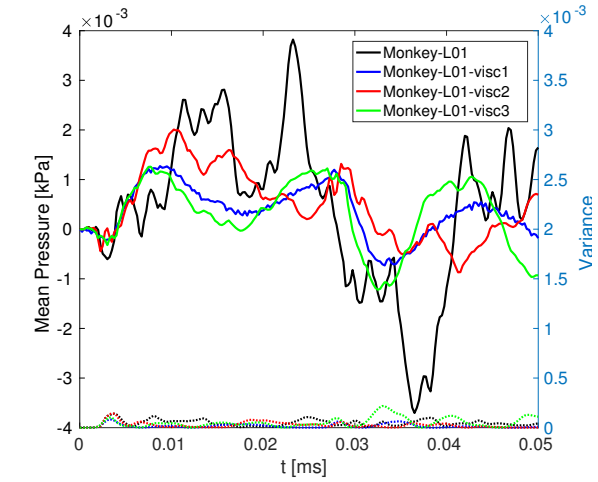

(a) Pressure

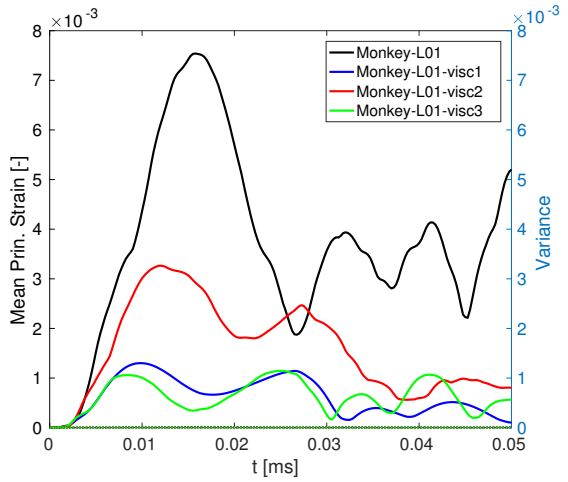

(b) Max Principal strains

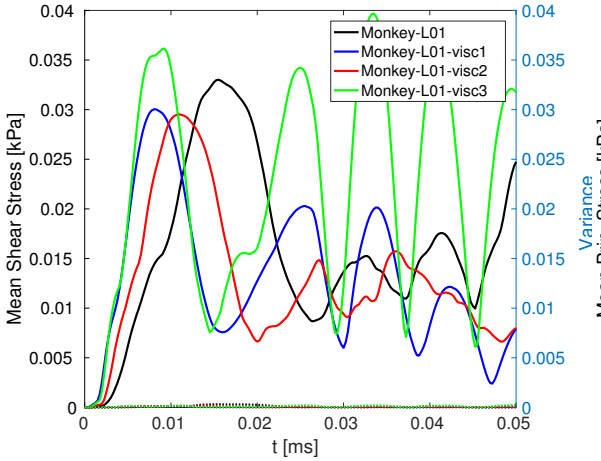

(c) Max Shear Stress

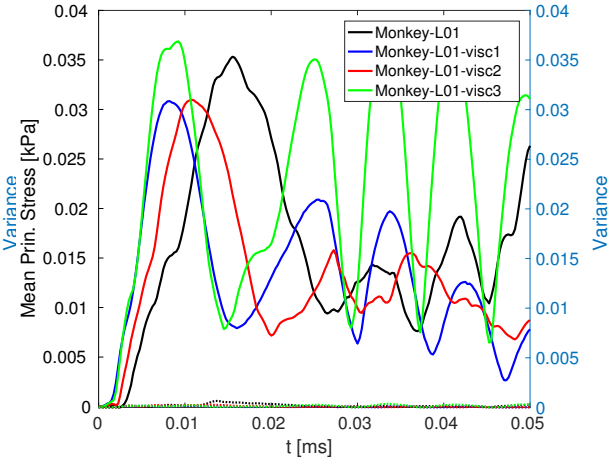

(d) Max Principal Stresses

Figure 4.2.22: Average time histogram of the representative points in the monkey brain. On the top row, the pressure of all the viscous models is similar having the non-viscous some variations, the strains are much lower on the if viscosity is applied and case "visc1" and "visc3" are very similar. On the bottom row, the behavior of both the shear and principal stresses is very close having the "visc3" a higher amplitude than the others with a similar frequency.

.

4.2.6 Analysis of mammalian brains

In this subsection we are going to compare the different geometries in the study to see if a correlation between them is possible. Also, since the meshes have a different number of elements the histogram will not be used anymore and the PDF distribution with "kernel" statistical function will be used as stated previously.

In figure 4.2.23 we see that the difference of the values is considerable, telling us that the higher the mass of the model the higher the results.

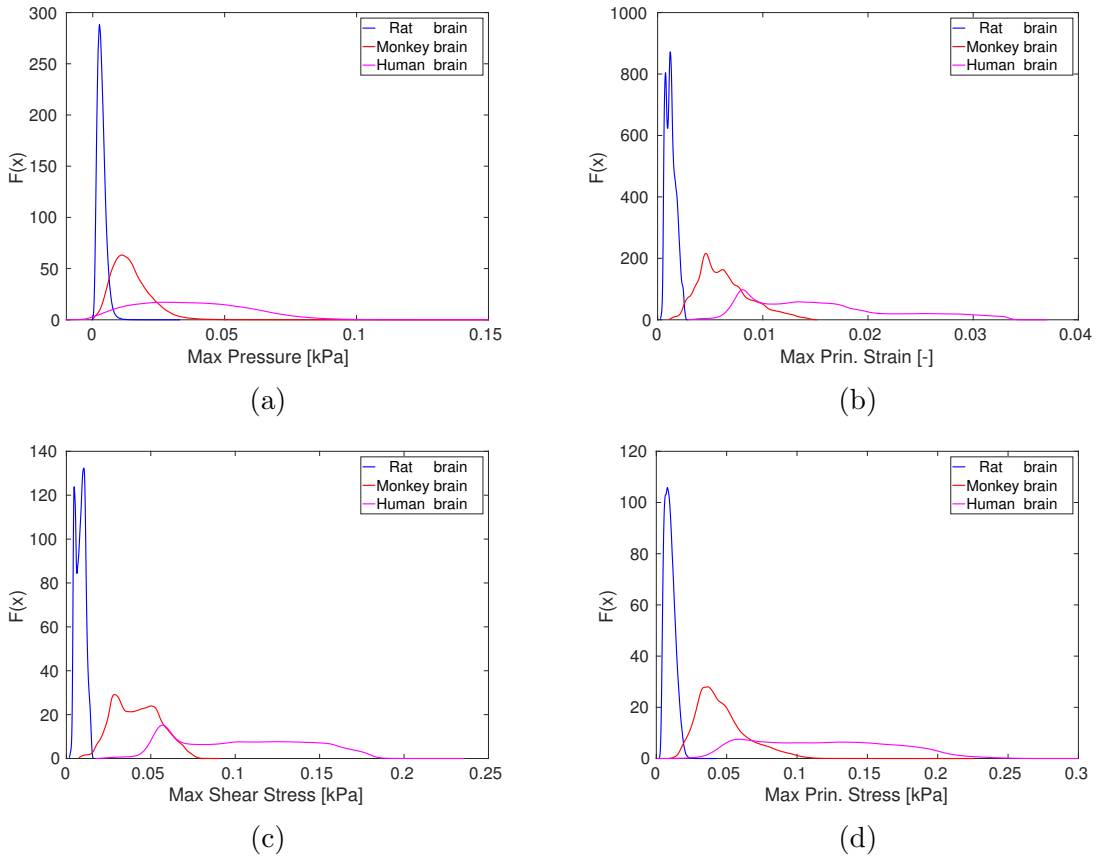

Figure 4.2.23: Probability density function (PDF) of the maximum accumulated values for the rat, monkey and human brain, all with CSF-Hype. The graphic shows how the bigger models have a distribution more spread with higher values.

4.2.7 Effect of the type of brain pattern (foldings)

The huge difference that exists in the different animals, a mass scaling of the smaller models has been done as shown in table 4.2.10. The aim of this mass scaling is to get results of the same order of magnitude and be able to perform a study of the influence of the geometry and the different types of brains, the lissencephalic one of smaller mammals and the gyrencephalic of the bigger ones with two hemispheres.

For the same reason of the previous section, the histogram will not be used and the PDF distribution with "kernel" statistical function will be used.

Also, since the human brain has defined the areas of white matter an extra case considering the proper material for it has been added in order to account for the heterogeneity that exist in the model.

Table 4.2.10: Mass scaling of the three meshes.

	Initial mass	*Times scaled*	*Final mass*
Human	1.58 Kg	-	-
Monkey	0.103 Kg	x2.485	1.58 Kg
Rat	7.06E-4 Kg	x13.05	1.58 Kg

The mass scaling is done automatically by the software, multiplying the coordinates of the nodes by a certain coefficient defined in Table 4.2.10.

Two different studies are carried in this section, first of all a comparison of the three meshes with an heterogeneous material for the brain matter, and another comparing the effects of adding the white matter in the human brain.

In the first study, figure 4.2.24 illustrates how all the models, the Rat, Monkey and Human, have a very similar dispersion of strains and stresses. These similarities are also visible in the figures 4.2.26 and 4.2.25 in the dispersion of the results and in the fact that the areas of concentration of stresses are located in the same places.

In the second comparison, it is clear in figure 4.2.24 that the heterogeneity has a big increase of the strains while changing the distribution of the stresses. The differences are more clear in figure 4.2.25, where we see that for the strains this increase is localized in a few zones and also for the stresses, and in figure 4.2.26 where the Principal stresses display a very heterogeneous dispersion very different from all the other models.

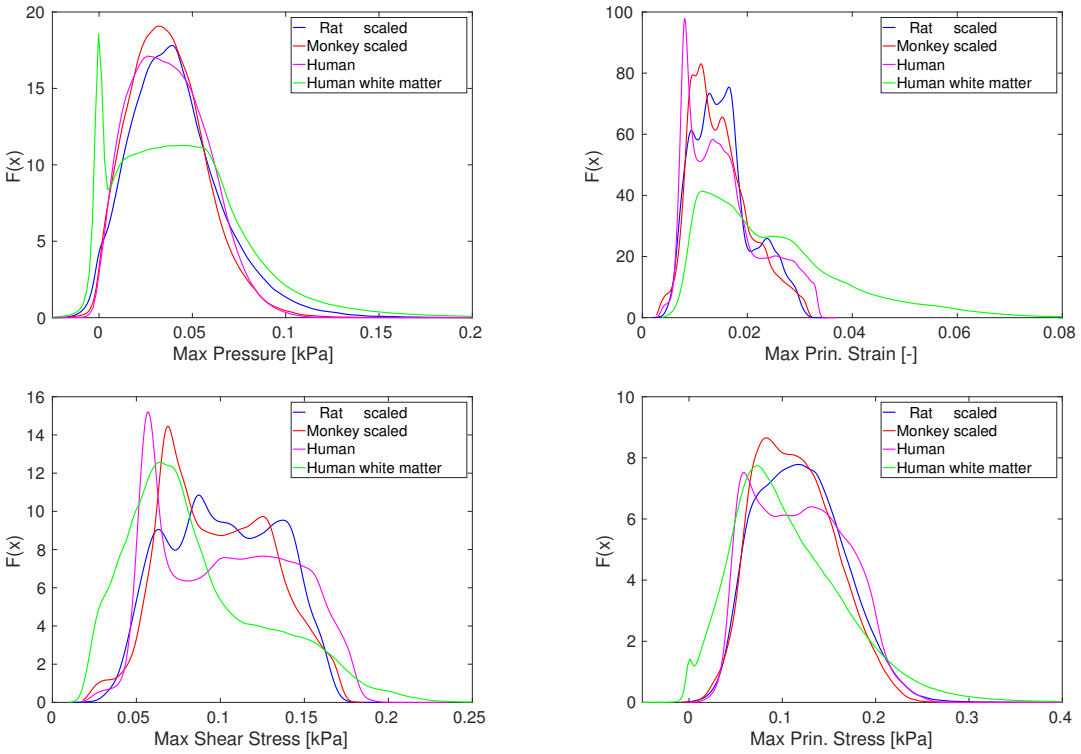

Figure 4.2.24: PDF of the maximum accumulated values for the rat and monkey brain, all of them with CSF-Hype.

Table 4.2.11: Average relative differences between models

case	*Max. Pressure*	*Max. Principal Strain*	*Maximum Shear Stress*	*Max. Principal Stress*
human vs Rat-sca	-8.98%	2.04%	2.04%	-0.45%
human vs Monkey-sca	2.34%	5.51%	5.53%	4.71%
Monkey-sca vs Rat-sca	-11.06%	-3.28%	-3.31%	-4.92%
human vs human-white	-14.97%	-37.51%	21.16%	10.24%

.

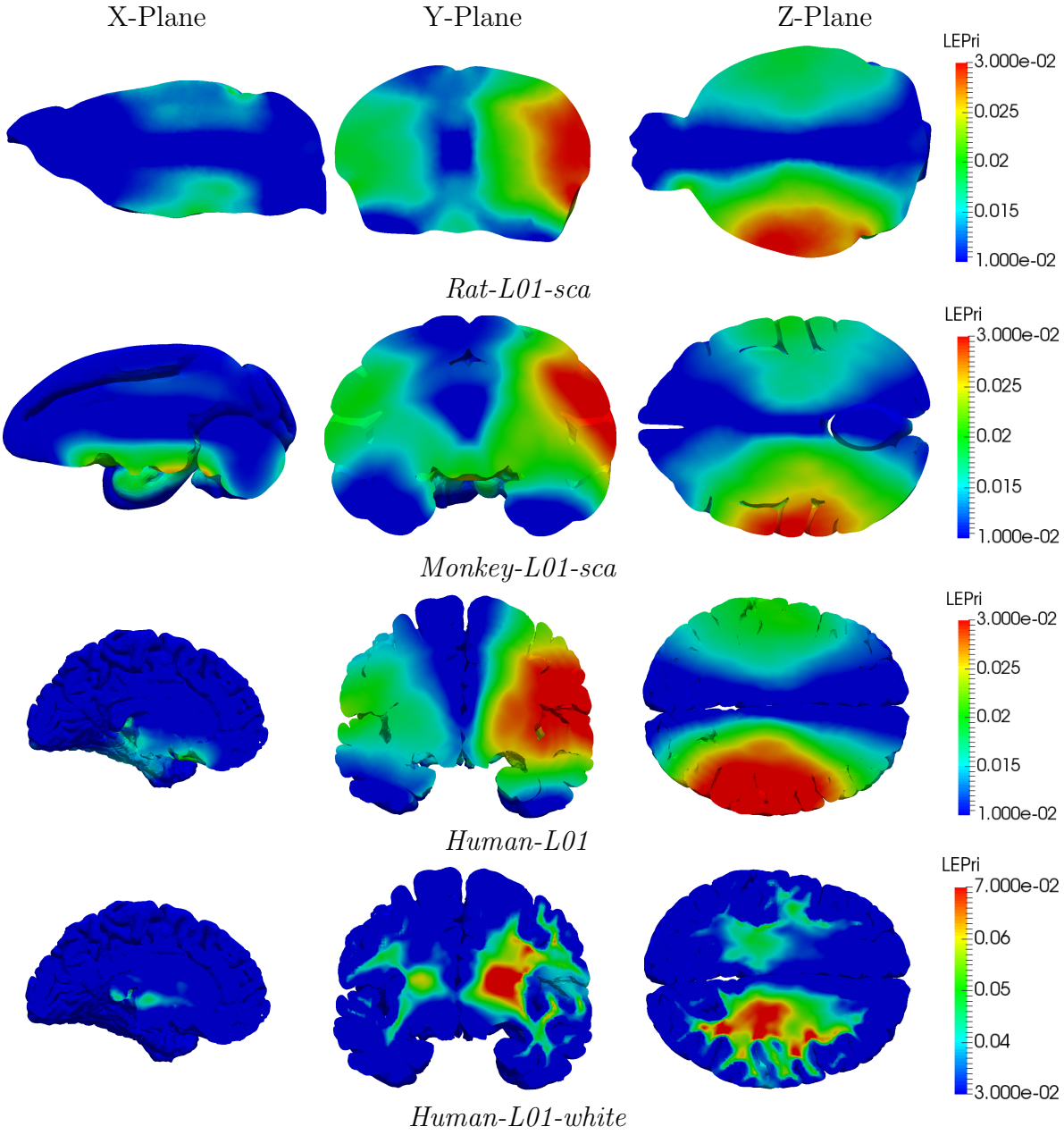

Figure 4.2.25: Maximum Accumulated Principal strains for all the models. For the first three rows the distribution is equivalent for all the geometries and can be considered that are behaving in the same way. The fourth, including heterogeneity follows somehow the same shape as the others but with concentration areas much smaller.

.

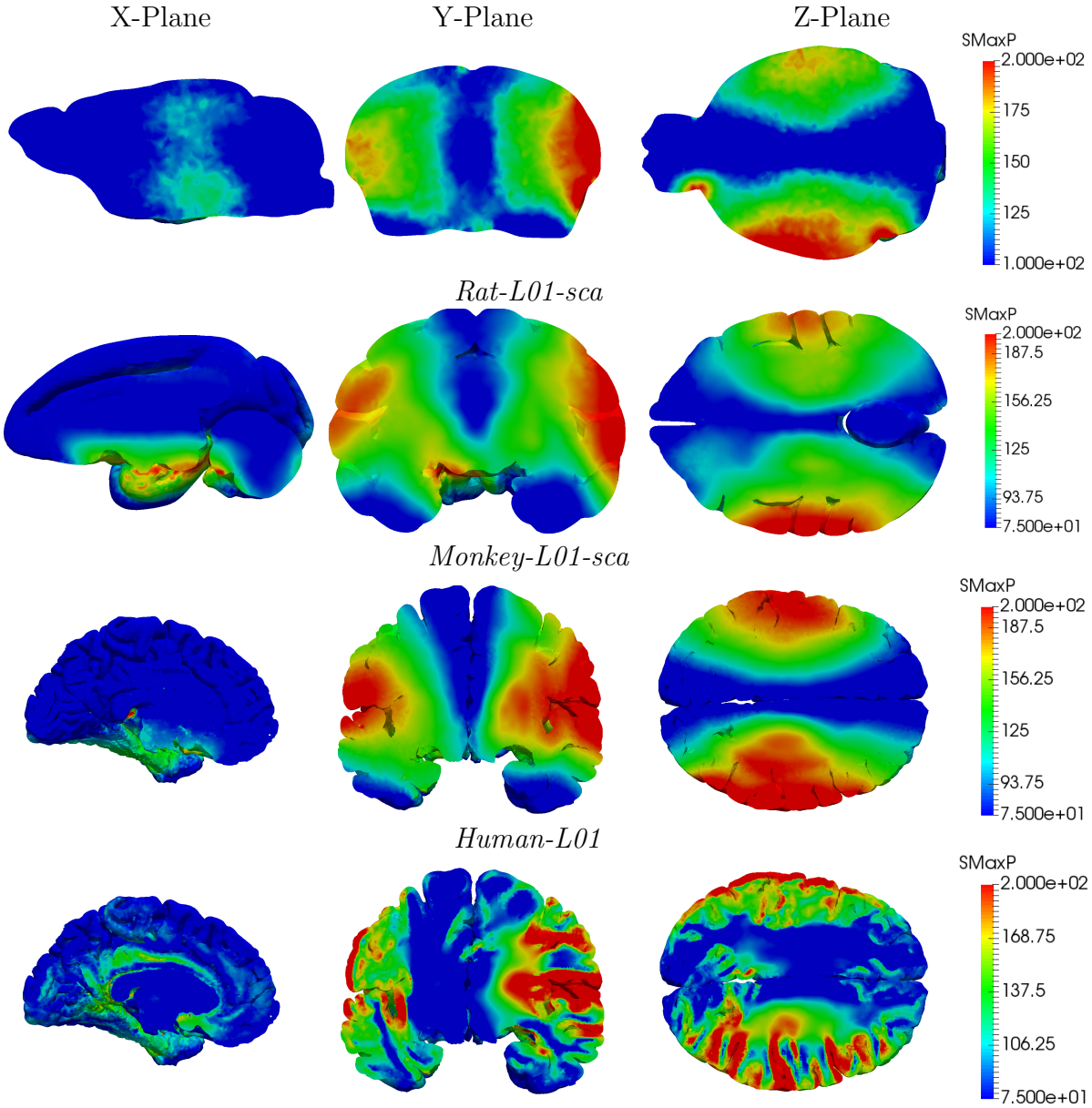

Human-L01 with CSF-Hype including Gray and White matter.

Figure 4.2.26: Maximum Accumulated Principal Stresses for the rat, monkey, and human with gray matter and including the white matter. The distribution of the first three rows can be considered perfectly scalable, meanwhile the fourth that accounts for a more heterogeneous geometry has a much more discontinuous behavior. Notice that even if the behavior is not continuous, the concentrations are located in the same areas.

.

4.3 Blast loading

In this section the effects of the blast loading will be observed on the rat and monkey brain and the loading considered is explained in subsection 3.7.1.

Another particularity of this section are the Boundary Conditions. The loading is introduced on the model as a pressure in the outer surface, and to prevent it from translating a set of string is modeled in the exterior boundary.

To compare the results, the same format as in the previous section will be used, with histograms comparing the same geometries and PDF with kernel statistical functions for different meshes.

4.3.1 Simulation cases

Table 4.3.1 summarizes all the simulations launched for this chapter, as the previous section the organization goes for the species that each mesh represents, following the name that will be used as a reference from now on, and the parameters used in each case.

Notice that in this section, unlike in the impact, it was possible to get the output at each time step, meaning that the accumulated values are more precise.

Table 4.3.1: Table of Shock Wave simulation cases.

		Parameters		
Spices	*Name*	Brain	CSF	Springs
Monkey	monkey	Gray	CSF-Hype	Base
	monkey-Wh	White	CSF-Hype	Base
	monkey-MIEG	Gray	CSF-Mieg	Base
	monkey-SprStiff	Gray	CSF-Hype	Stiffer
	monkey-SprWeak	Gray	CSF-Hype	Weaker
Rat	rat	Gray	CSF-Hype	Base
	rat-sca	Gray	CSF-Hype	Base
	rat-mieg	Gray	CSF-Mieg	Base
	rat-sca-mieg	Gray	CSF-Mieg	Base
	rat-sca-lin	Gray	CSF-Lin	Base

Table 4.3.2: Computational cost of the blast models.

Model	CSF-Hype	CSF-lin	CSF-MIEG
Rat	20:00 h	-	22:45 h
Rat scaled	3:00 h	2:40 h	5:00 h
Monkey	7:10 h	-	9:30 h

4.3.2 Influence of the CSF Modeling

It is found in the bibliography that the best material for modeling fast transient dynamics in the CSF is the equation of state Mie-Grneisen. But due to the high impact that it has on the time step, which drops one order of magnitude, it is not possible to use it for all the simulations. A study of the CSF material will be done.

In figure 4.3.1 it is depicted the brain response along all the different models of the CSF on the rat. It is observed that all the three simulations have a close distribution for all the parameters, as can be corroborated in table 4.3.3 where it shown how the relative differences in the rat are negligible.

Modeling the monkey histograms varying the CSF in figure 4.3.2, it is also seen that the models behave in a close relation even if some little differences appear on the sides. It is also computed the relative difference between them shown also in table 4.3.3 in the last row. The results let us understand that the two models can be considered equivalent.

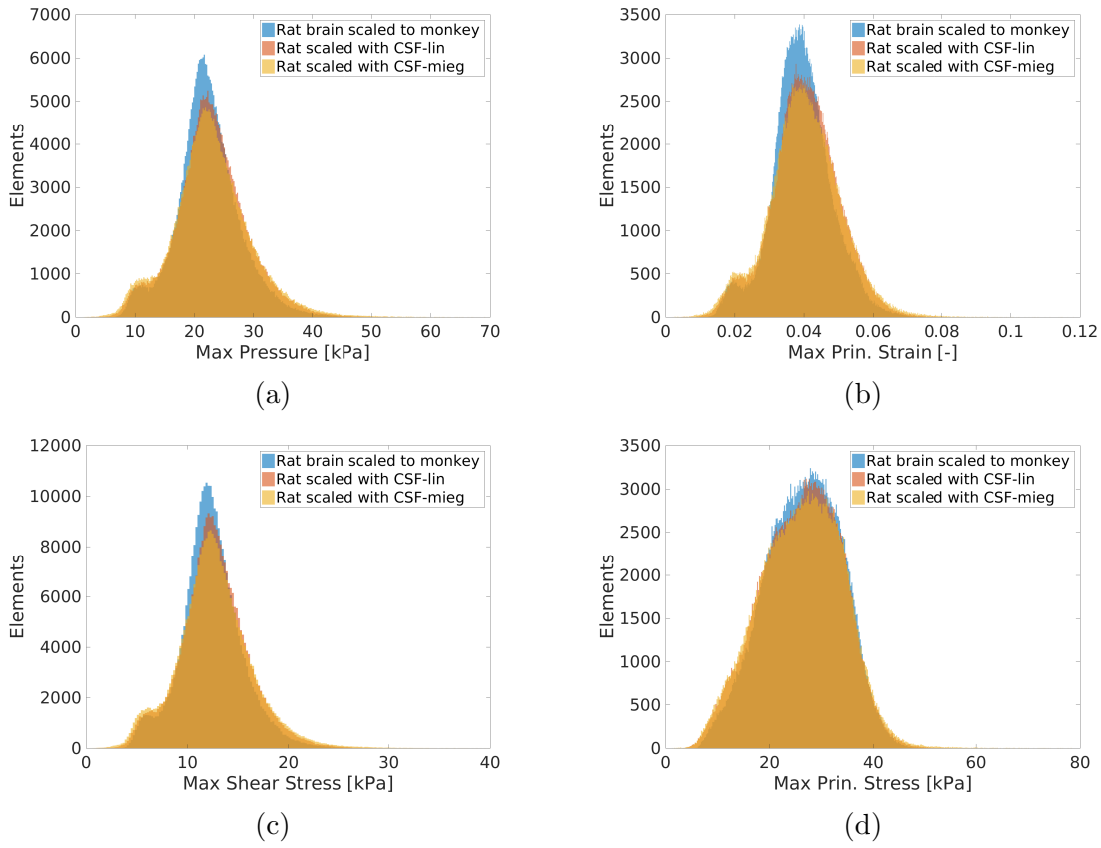

Figure 4.3.1: Maximum accumulated values for different discretization of the CSF for the rat models scaled to the monkey mass. The bin-width of this histogram is of 0.2 for the pressure and stresses and 0.0002 for the strains.

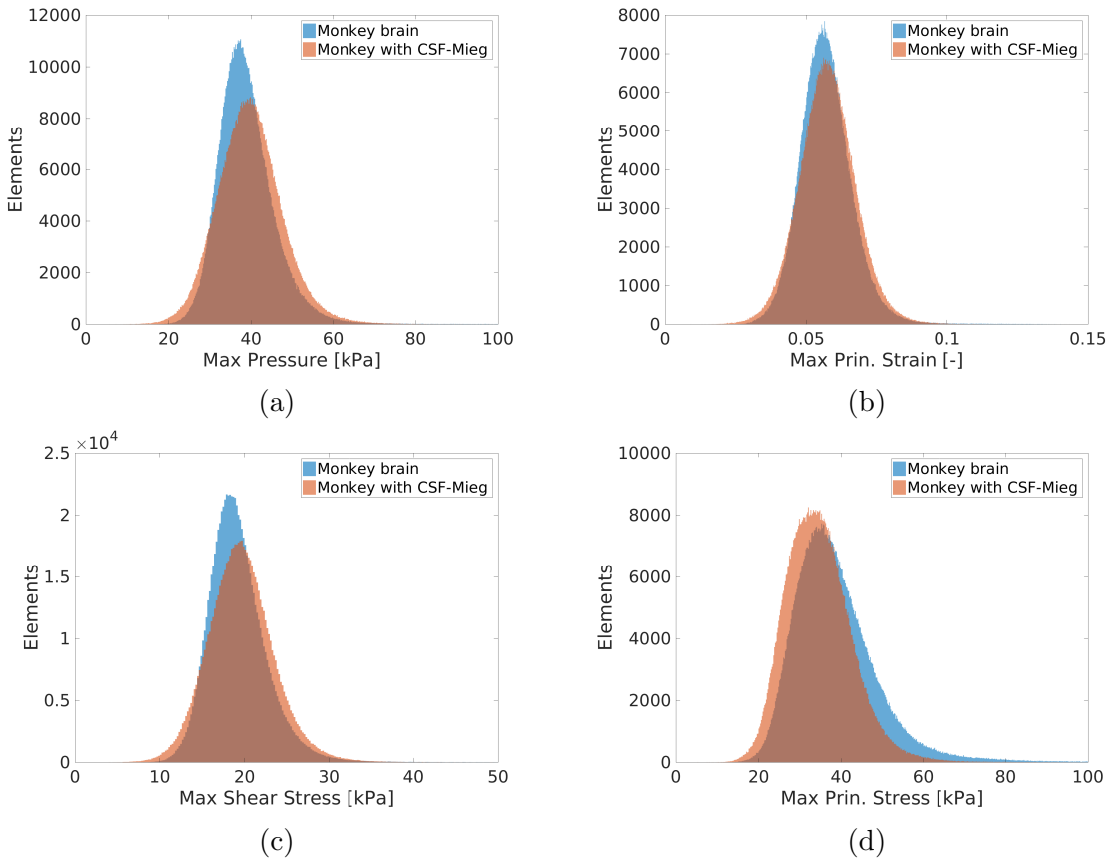

Figure 4.3.2: Maximum accumulated values for different discretization of the CSF for the Monkey. The bin-width of this histogram is of 0.2 for the pressure and stresses and 0.0002 for the strains.

Table 4.3.3: Average relative differences between models

case	*Max. Pressure*	*Max. Principal Strain*	*Maximum Shear Stress*	*Max. Principal Stress*
Rat-sca vs Rat-sca-lin	2.48%	-2.63%	-2.27%	1.60%
Rat-sca vs Rat-sca-mieg	-2.52%	-2.23%	-2.32%	1.38%
Rat-mieg vs Rat-sca-lin	0.05%	-0.35%	0.06%	0.23%
Monkey vs Monkey-mieg	-2.21%	-0.87%	-2.07%	12.05%

Regarding the distributions along the geometries, in the case of the rat they are displayed in two figures classified for the outputs presented, figure 4.3.3 for the strains and figure 4.3.4 for the pressures. It is observed that the behavior of the three models of the CSF is not only similar in the magnitude of its values but also it has an almost identical plot over the space for the strains and only a few details or concentration areas can be noticed in the pressures.

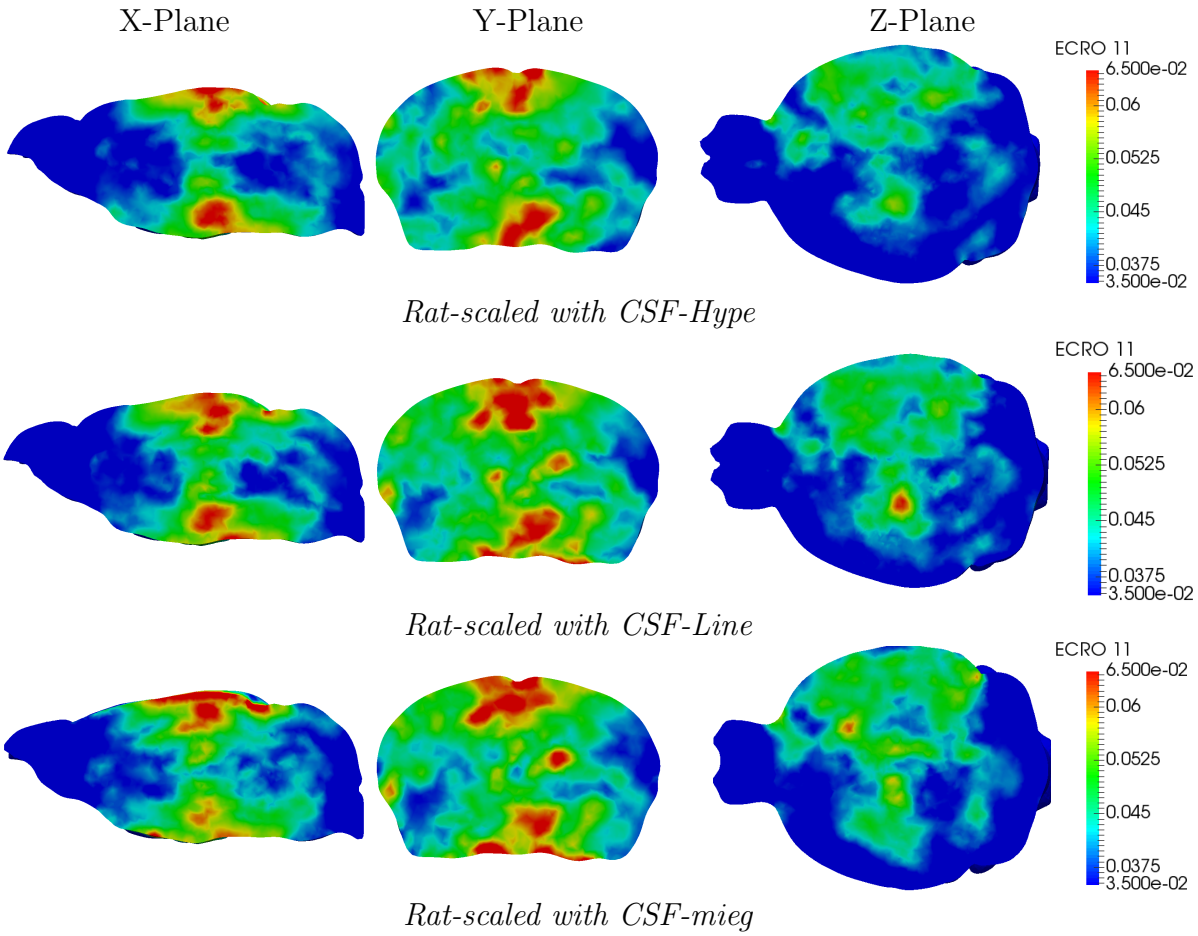

Figure 4.3.3: Distribution of the Maximum Accumulated Principal strains on the rat-scaled along the three CSF materials considered. All the models have a similar behavior, with a concentration of strains on the top and bottom part connecting this parts from the middle of the model.

For the monkey the distributions are also presented in two figures, in 4.3.5 it is depicted with a CSF-Hype, while figure 4.3.6 shows the CSF-Mieg distributions. Comparing the strains of both models having the same magnitude, we see that the hyperelastic consideration of the CSF leads to slightly higher values in the center of the model while the Mie-Grüneisen have a more spread behavior. For the pressures, leaving apart the difference of magnitude, the concentrations shown in both models are very similar without any major remark.

Also notice that taking a closer look to both rat and monkey distribution of stresses, we see that for all cases in the monkey the have specially stressed the base that serves of nexus of union of both hemispheres while the rat have a more uniform behavior.

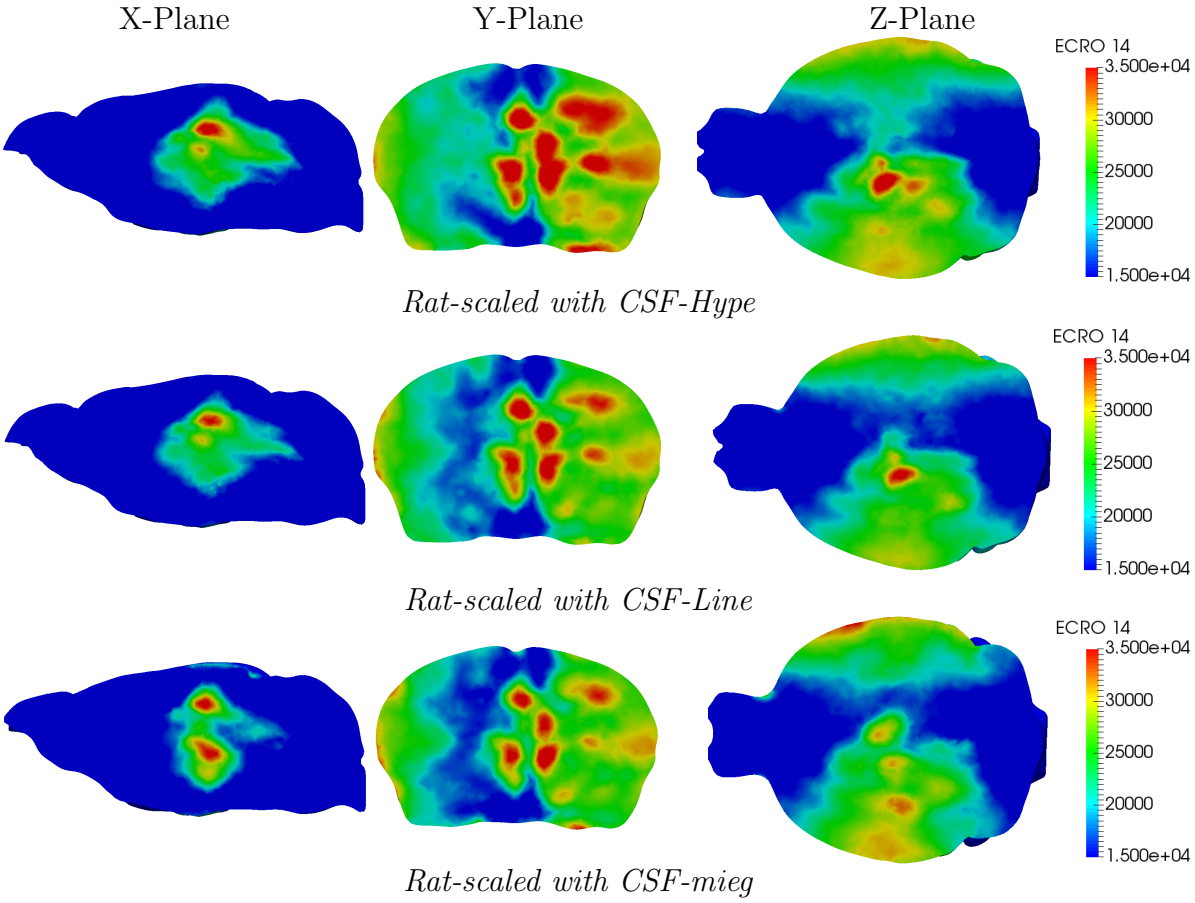

Figure 4.3.4: Distribution of the Maximum Accumulated Principal pressures on the rat geometry for the three CSF materials. The behavior has a clear concentration on both sides of the brain having the highest values on the opposite side of the load.

.

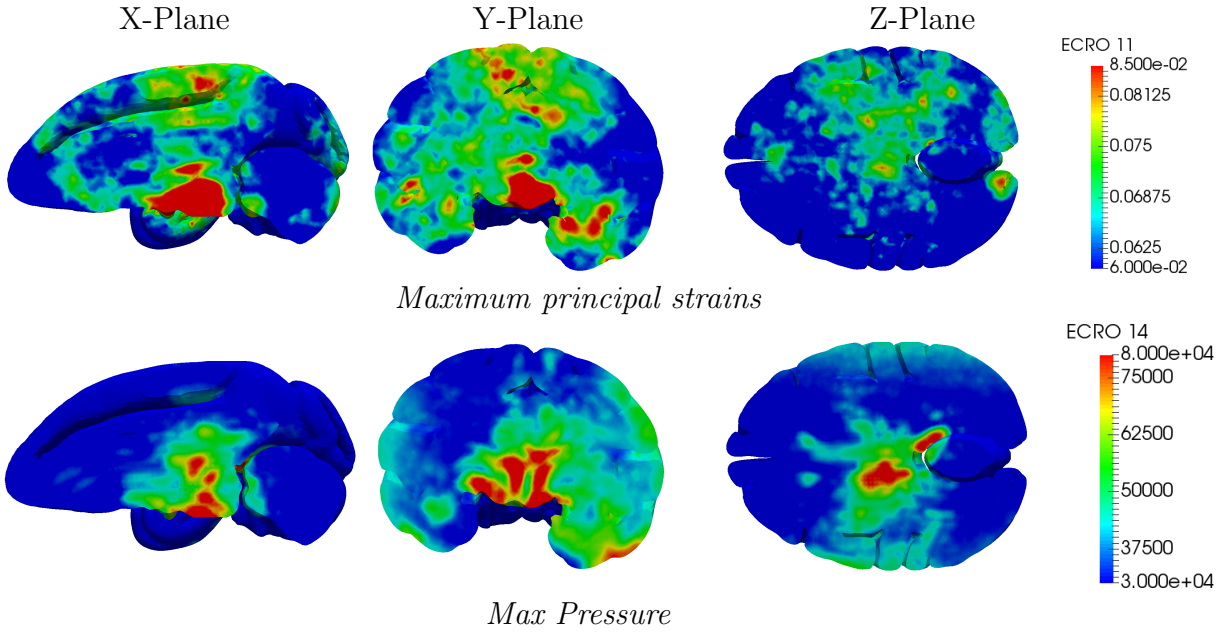

Figure 4.3.5: Distributions for the Monkey with CSF-Hype, the first row depicts the principal strains which are concentrated in the middle spreading to the rest of the brain. The second row references the maximum accumulated pressures which are concentrated in the center.

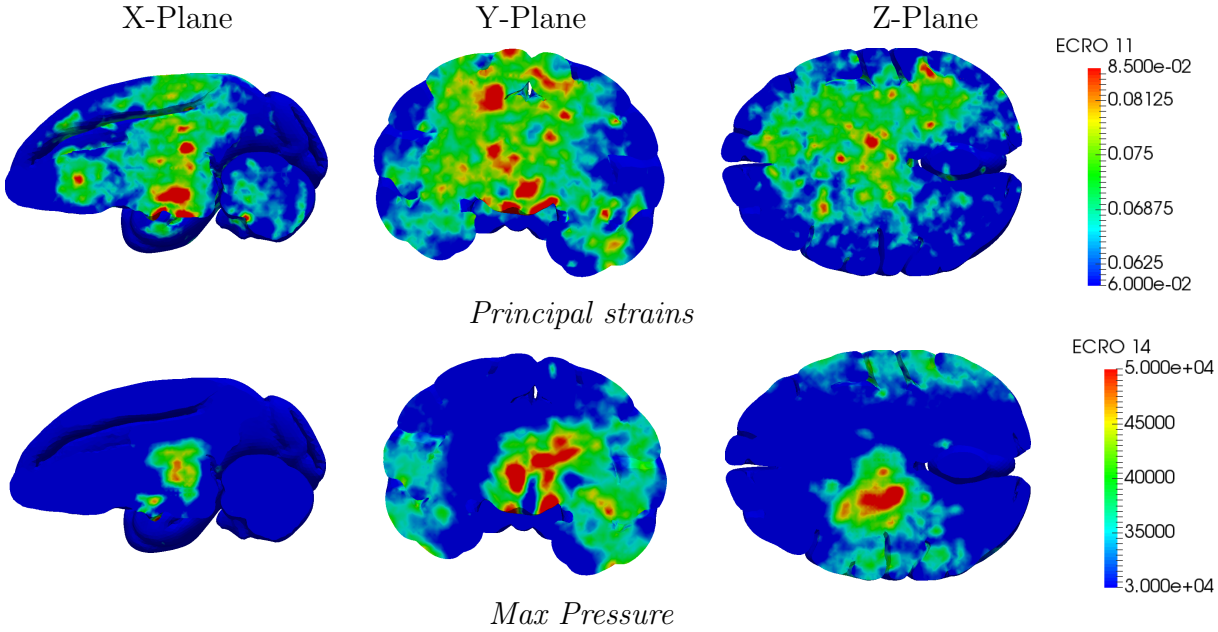

Figure 4.3.6: Distributions in the Monkey with CSF-Mieg. On the top row there are the principal strains that are widespread over the geometry, and the bottom row shows how the pressures concentrates in the center of the geometry.

4.3.3 Effect of the mammalian brain

In this subsection a comparison between the studied mammals is done. Since the meshes have a different number of elements we will not use an histogram but a "kernel" probability function.

In figure 4.3.7 we see that for all the parameters the curves are closer than in the impact regime. But once we switch to look at the distributions of the rat in figure 4.3.8 and of the monkey shown in the last subsection, figure 4.3.5, we se that the behavior is totally different. While in the rat the principal strains are concentrated on the outer boundaries, in the monkey they are gathered in the center, and a similar observation is done in the maximum pressures, that in the rat are distributed uniformly in the lateral direction in the monkey are concentrated again in the center of the geometry.

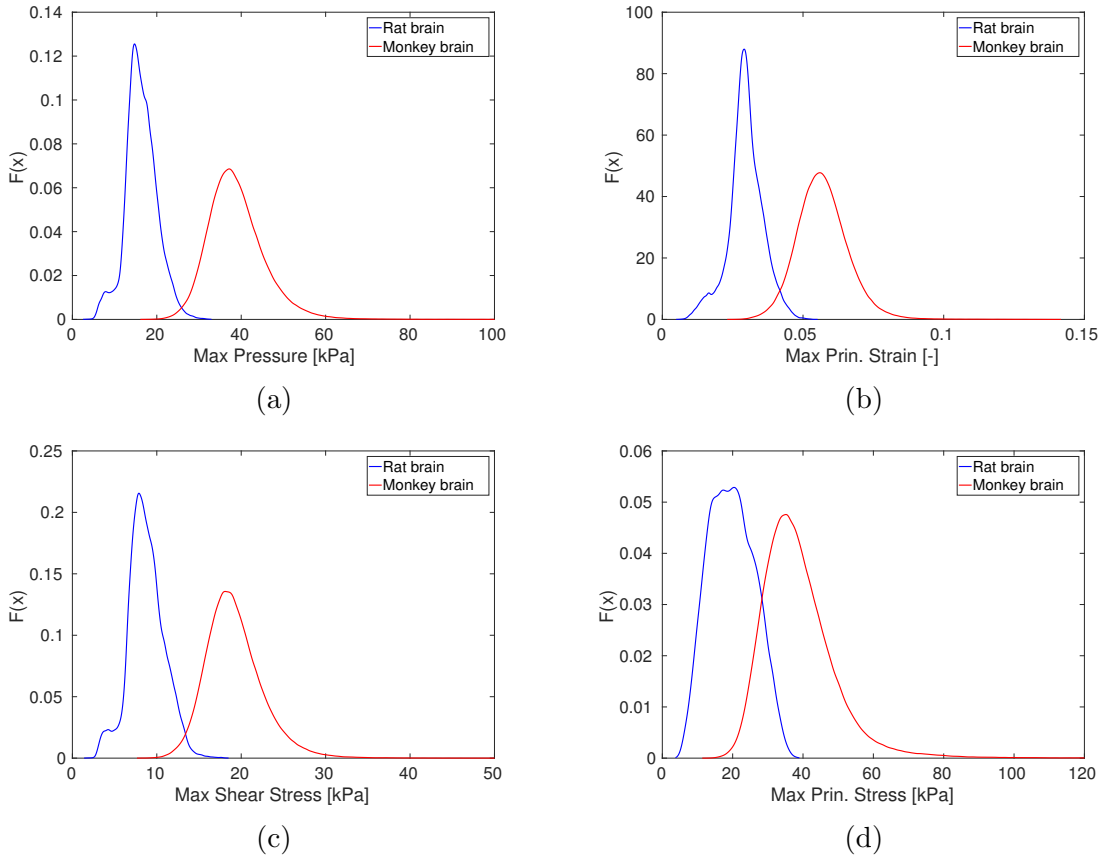

Figure 4.3.7: Probability density function (PDF) of the maximum accumulated values for the rat and monkey brain, both with CSF-Hype. The graphic shows how the monkey brain in (a,b,c) has a more spread range and is shorter than the rat, which has more concentrated values.

In this case is important to notice that the shape of the outer boundary of the CSF is important and more relevant in the results than in the impact case. This is because in the blast scenario we are applying the load as a pressure following the contour of

the mesh and thus modifying the direction of the accelerations, adding a geometrical inconvenience on comparing the previous results.

Notice also that there are differences in the distributions of the stresses seen in the rat, figure 4.3.8, and the ones from the rat scaled, figures 4.3.3 and 4.3.4 of the previous subsection. This leads to understand that scaling the rat model have changed the internal behavior of the model, even if it conserves in general ways the shape.

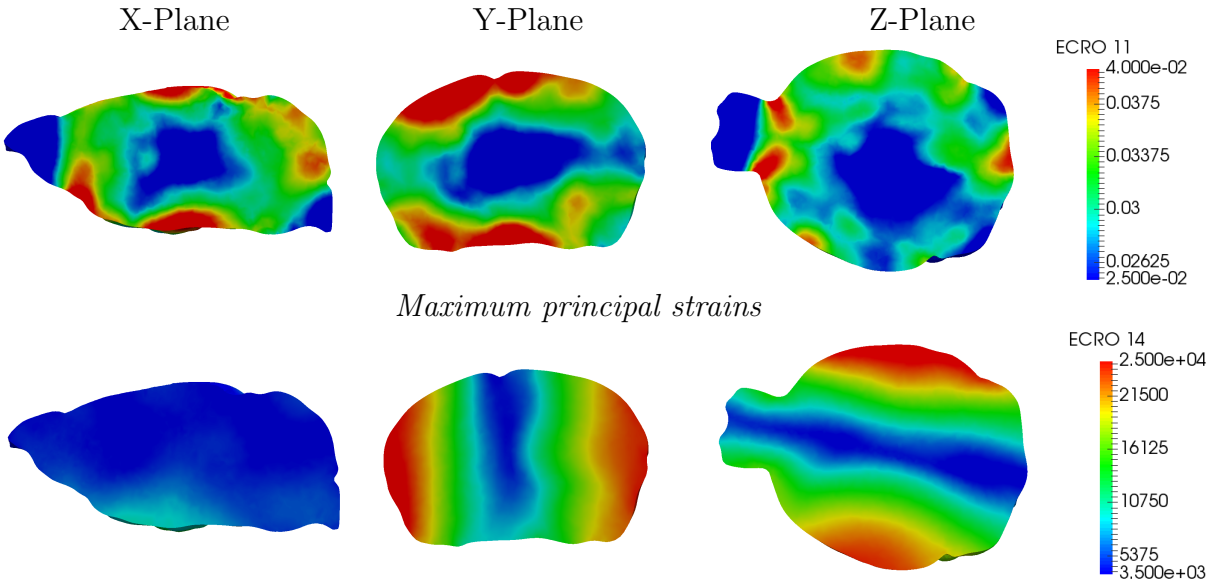

Figure 4.3.8: Distribution in the rat brain for a Hype discretization of the CSF. Here we can see how the strains accumulates around the boundary of the brain while the pressures are distributed along the lateral axis uniformly.

4.3.4 Effect of the folding pattern

Following the previous subsection, we try to use the rat mesh with the mass of the monkey with the purpose to see if we can escalate the outputs and interrelate the rat with the monkey. This is not so simple to achieve as depicted in figures 4.3.9 for the CSF-Hype and 4.3.10 for the CSF-Mieg. The differences between any of the rat models and the monkey are still considerable, being the Rat-scaled-mieg the closest one to achieve this as seen in table 4.3.4.

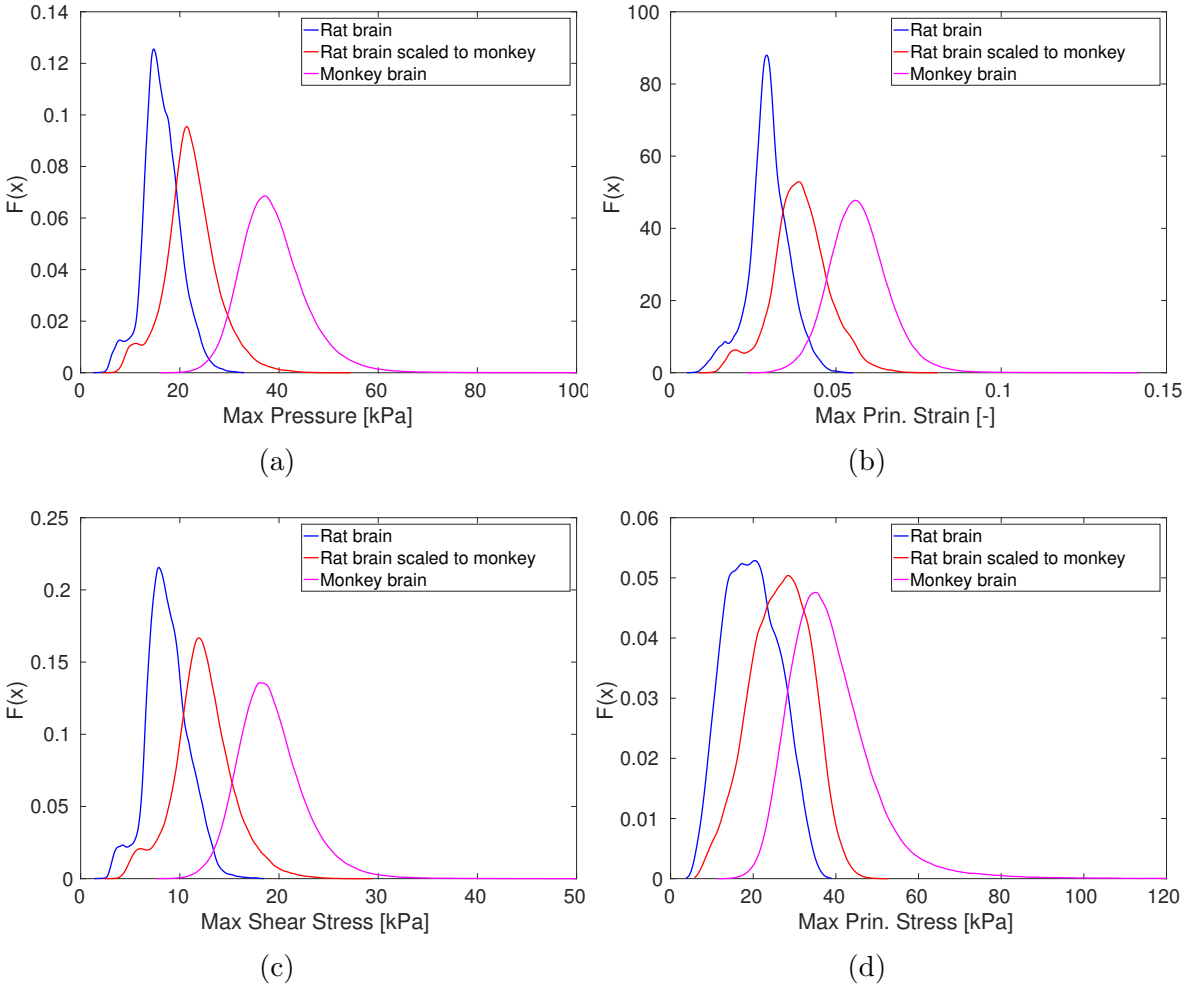

Figure 4.3.9: PDF of the maximum accumulated values for the rat, rat scaled to monkey and monkey all models with CSF-Hype. We observe that the values form the rat scaled get closer to the ones of the monkey.

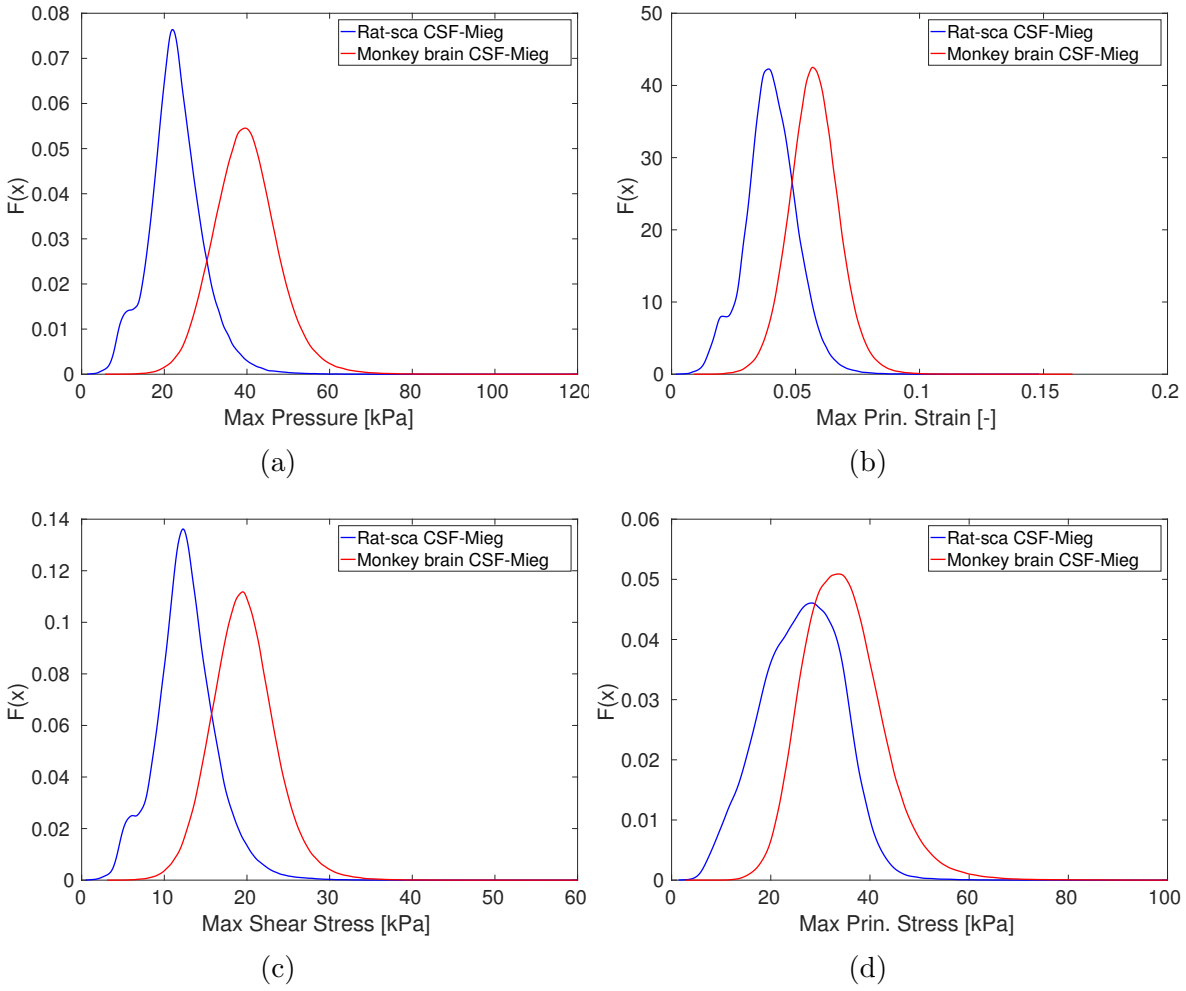

Figure 4.3.10: PDF of the maximum accumulated values for the rat scaled and the monkey with CSF-Mieg, there is no value of the rat without scaling due to the large computational cost.

Table 4.3.4: Average relative differences between models

case	*Max. Max. Principal Pressure*	*Strain*	*Maximum Shear Stress*	*Max. Principal Stress*
Monkey vs Rat	138.16%	92.49%	119.38%	96.47%
Monkey vs Rat-sca	74.45%	45.18%	55.37%	46.08%
Rat vs Rat-sca	-26.75%	-24.58%	-29.18%	-25.65%
Monkey-mieg vs Rat-sca-mieg	73.90%	43.10%	54.96%	32.16%

.

4.3.5 Parametric Boundary conditions

Another factor also important in the study is the effect of the blast depending on the stiffness of the springs used as boundary conditions that are trying to emulate the neck. For this purpose the parameters of the strings have been calibrated taking into account the total mass of the model and supposing a movement tolerance that would be acceptable for the brain. But the question of how this factor it would affect the results this factor remains and it is analyzed in this subsection.

In order to test the parametric response of the strings, two extra models were prepared, one with the double of Young modulus and the other with half of it, and the results depicted in figure 4.3.11 show that the affecting of these changes in the strains or the shear stresses are not relevant, but regarding the pressure or von misses stress a not expected behavior is found. While the values of both the parametric models can be taken as equals, the only different model was the one set as default.

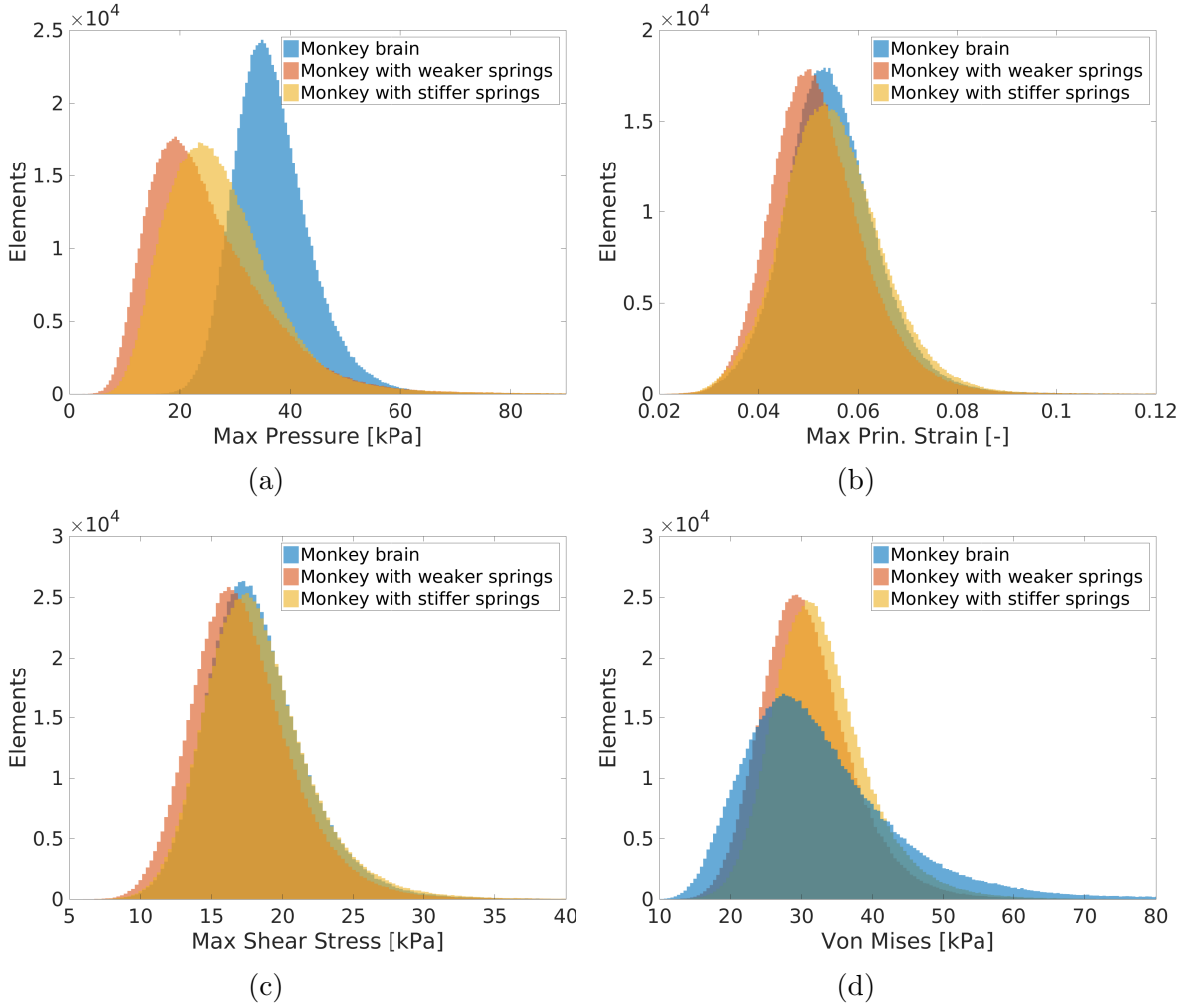

Figure 4.3.11: Different stiffness of the springs on the Monkey

Chapter 5

Discussion

We are still far from the goal of having a complete human head model. The main problem is the lack of data and the ethical problems that suppose this kind of experiments. The comparison of different animal models has great importance in the study of the brain because, being able to scale the results of different investigations could help in reducing the experimentation of animals and use it to unveil the mechanics of the human brain.

The principal focus on the literature has been to model passive response of the brain, but in some studies they worked on the viscoelastic part. We demonstrate that the viscoelasticity does not have major affection on the distribution, but it have importance in the accumulated values for the stretches.

Changing the material modeling of the CSF for different approximations given in the bibliography (hyperelastic, linear elastic or Mie-Grüneisen) [65, 66, 22, 23, 38] ends with huge differences in the final response of the brain. On blast loading conditions the effect of this difference CSF models shows a perfect correlation between all the materials analyzed. Once we switch to the impact, the effect of the CSF material model change with respect to the, especially between the hyperelastic and the other two. This is thought to be because the Mie-Grüneisen material and the linear elastic are much stiffer than the hyperelastic brain material increasing the frequency of the stress waves into the soft brain material and causing a more complex distribution pattern along the geometry.

In the case of little variations as performed in section 4.2.2 the effects are considered negligible. In the case of the impact we considere also the direction of the load and we do not find major incidence of this characteristic, apart from rotating the results in the geometries.

The size and the shape of the brain are the parameters which, in our case, define the geometry of each particular animal. These parameters have a large affection on the results since models with bigger masses show higher deformations and stresses. For larger, or mass scaled, models the stress wave dissipates along the space and do not have reflections inside the head. Regarding the folding pattern, it has important effects in the stresses and strains distribution on the brain.This is important because

the FE models of the human brain would need to account for the complex folding pattern of the brain.

Chapter 6

Conclusions

We have performed a dynamic analysis of different mammalian brains in fast transient dynamics and made a study of the effects of size, shape, boundary conditions and material.

After the analysis we have concluded that all the parameters have relevance in the mechanical behavior of the brain, including the folding pattern.

The CSF modeling has big influence since it is the medium from which the loads will be transfered to the brain matter, and the results depending on the material model are very different. The size and shape of the brains have the utmost importance. The size of the model is an important parameter since it does not only account for the magnitude of the results, but also it affects on the reflected stress waves inside the brain. It is also very important to take into account the complex geometry of the mammalian brains.

In contrast, the parameters that are not considered so important are the direction of the load and the viscoelastic effects. The first one just keeps the magnitudes of the results while rotating the distribution on the model. And the viscoelastic effects that, after computing the maximum accumulated values of the model the viscoelastic effect is showed not to be so important.

As future work three points are left: The anisotropy is an important parameter in the study of the behavior of the brain. A model which is ready to use this approach was prepared during the elaboration of this thesis, but due to internal problems in the software Europlexus on understanding the huge tractography data, no results could be produced in this period.

We also need to validate the model with the rat experiment of Calabrese et al. [4] using medical imaging techniques. For the numeric point of view there is laking a strain rate dependent material modeling of the brain tissue, that would prove crucial if the dynamic effects are considered.

Bibliography

[1] Abaqus User's Manual, on-line version: http://bobcat.nus.edu.sg:2080/v6.14/index.html

[2] Agoston D.V. and Kamnaksh A. Modeling the Neuro-behavioral Consequences of Blast-Induced Traumatic Brain Injury Spectrum Disorder and Identifying Related Biomarkers. Brain Neurotrauma: Molecular, Neuropsychologival, and Rehabilitation Aspects. International Standard Book Number-13: 978-1-4665-6599-9 (eBook - PDF) pp. 309-327

[3] Budday S, Nay R, Rooij R, Steinmann p, Wyrobek T, Ovaert TC, Kuhl E. Mechanical properties of gray and white matter brain tissue by indentation. journal of the mechanical behavior of biomedical materials 46 (2015) 318 330

[4] Calabrese E, Du F, Garman R.H, Johnson G.A, Riccio C, Tong L.C, and Long J.B. Diffusion Tensor Imaging Reveals White Matter Injury in a Rat Model of Repetitive Blast-Induced Traumatic Brain Injury. Journal of neurotrauma 31:938-950 (May 15, 2014), DOI: 10.1089/neu.2013.3144

[5] Casadei F, Saez P, Díez P, Larcher M, Valsamos G. Scoping calculations for simulation of human head impact with EUROPLEXUS. JRC Technical Report, in publication.

[6] Casadei F, Saez P, Díez P, Larcher M, Valsamos G. Simulation of rat head deceleration with EUROPLEXUS. JRC Technical Report, in publication.

[7] Casadei F, Saez P, Díez P, Larcher M, Valsamos G. Simulation of rat and monkey head slice deceleration with EUROPLEXUS. JRC Technical Report, in publication.

[8] Casadei F, Valsamos G, Larcher M, Duñó C, Saez p, and Díez P. Simulation of monkey and human head under blast loading with EUROPLEXUS Paper under preparation.

[9] Casadei F and Halleux JP. Binary spatial partitioning of the central-difference time integration scheme for explicit fast transient dynamics. Int. J. Numer. Meth. Engng 2009; 78:14361473. DOI: 10.1002/nme.2533

[10] Chatelin S, Deck C, Renard F, Kremer S, Heinrich C, Armspach JP, Willinger JP. Computation of axonal elongation in head trauma finite element simulation. Journal of the mechanical behavior of biomedical materials 4 (2011) 19051919

[11] Chatelin S, Deck C. An anisotropic viscous hyperelastic constitutive law for brain material finite element modeling. Bioreheology. December 2012. DOI: 10.1007/s12573-012-0055-6

[12] Chafi MS, Ganpule S.G, Gu L, Chandra N. Dynamic response of Brain subjected to Blast loadings: Influence of frequency ranges. Mechanical & materials engineering faculty publications. Paper 60.

[13] Chopra A.K. Dynamics of Structures: Theory and Applications to Earthquake Engineering (2nd Edn.), Prentice-Hall, Englewood Cliffs, NJ (2001)

[14] Dommelen J.A.W, Sande T.P.J, Hrapko M, Peters G.W.M. Mechanical properties of brain tissue by indentation: Interregional variation. Journal of the mechanical behavior of biomedical materials 3, 2010, 158-166.

[15] Feng Y, Okamoto RJ, Namani R, Genin GM, Bayly PV. Measurements of mechanical anisotropy in brain tissue and implications for transversely isotropic material models of white matter. Journal of the mechanical behavior of biomedical materials, 2013, 117-132

[16] Feng Y, Abney TM, Okamoto RJ, Pless RB, Genin GM, Bayly PV. Relative brain displacement and deformation during constrained mild frontal head impact. Journal of the royal society interface 7, 2010, 1677-1688

[17] Ferradás, González E., D´az Alonso, F., Doval Miñarro, M, Miñana Aznar, A., Ruiz Gimeno, J., & Sanchez Pérez, J. F. (2008). Consequence analysis by means of characteristic curves to determine the damage to humans from bursting spherical vessels. Process Safety and Environmental Protection, 86, 121129.

[18] Franceschini G. THE MECHANICS OF HUMAN BRAIN TISSUE. PHD THESIS

[19] Fu YB, Ogden RW. Nonlinear Elasticity: Theory and Applications. ISBN 0 521 79695 4 paperback

[20] Fung YC, Fronek K, Patitucci P. Pseudoelasticity of arteries and the choice of its mathematical expression. Am J Physiol. 1979 Nov;237(5):H620-31. DOI: 10.1152/ajpheart.1979.237.5.H620

[21] Fung YC. 1993 Biomechanics: mechanical properties of living tissues, 568. New York, NY:Springer.

[22] Garimella H.T., Kraft R.H. Modeling the mechanics of axonal fiber tracts using the embedded finite element method. Int J Numer Meth Biomed Engng. 2017;33:e2823. DOI: 10.1002/cnm.2823 https://doi.org/10.1002/cnm.2823

[23] Giordano C, Kleiven S. 2014 Connecting fractional anisotropy from medical images with mechanical anisotropy of a hyper-viscoelastic fiber-reinforced constitutive model for brain tissue. J. R. Soc. Interface 11:20130914. http://dx.doi.org/10.1098/rsif.2013.0914

[24] Giordano, C. & Kleiven, S. Evaluation of Axonal Strain as a Predictor for Mild Traumatic Brain Injuries Using Finite Element Modeling. Stapp car crash journal, 2014, 58, 29-62

[25] Bernal R, Pullarkat PA, Melo F. Mechanical properties of axons. Phys Rev Lett. 2007 Jul 6;99(1):018301. Epub 2007 Jul 3.

[26] Giordano C, Zappal S, Kleiven S. Anisotropic finite element models for brain injury prediction: the sensitivity of axonal strain to white matter tract inter-subject variability. Biomech Model Mechanobiol. DOI: 10.1007/s10237-017-0887-5

[27] Gupta R.K., and Przekwas A. Mathematical models of blast-induced TBI: current status, challenges, and prospects. Frontiers in Neurology, doi: 10.3389/fneu.2013.00059.

[28] Gu L, Chafi MS, Ganpule S, Chandra N. The influence of Heterogeneous Menings on the Brain mechanics under Primary Blast Loading. Mechanical & materials Engineering Faculty Publications. Paper 83 (2012)

[29] Hagemann, A., 2001, A Biomechanical Model of the Human Head with Variable Material Properties for Intraoperative Image Correction. PHD dissertation, Logos Verlag Berlin, ISBN 3-89722-665-0.

[30] Holzapfel G.A. Nonlinear Solid Mechanics A Continuum approach for engineering (2000)

[31] Karami G, Grundman N, Abolfathi N, Naik A, Ziejewski M. A micromechanical hyperelastic modeling of brain white matter under large deformation. Journal of the mechanical behavior of biomedical materials 2 (2009) 243-254

[32] Kaster T, Sack I, Samani A. Measurement of the hyperelastic properties of ex vivo brain tissue slices. Journal of Biomechanics 44, 2011, 1158-1163

[33] Kleiven S. Predictors for Traumatic Brain Injuries Evaluated through Accident Reconstructions. Stapp Car Crash Journal, Vol. 51 (October 2007), pp.

[34] Koliatsos, V.E., I. Cernak, L. Xu, Y. Song, A. Savonenko, B.J. Crain et al. 2011. A mouse model of blast injury to brain: Initial pathological, neuropathological, and behavioral characterization. J Neuropathol Exp Neurol. 70:399416

[35] Larcher M, Forsberg R, Bjrnstig U, Holgersson A & Solomos G (2016) Effectiveness of finite-element modeling of damage and injuries for explosions inside trains, Journal of Transportation Safety & Security, 8:sup1, 83-100, DOI: 10.1080/19439962.2015.1046619

[36] Leibovici, D., Gofrit, O. N., Stein, M., Shapira, S.C., Noga, Y., Heruti, R. J., & Shemer, J. (1996). Blast injuries: Bus versus open-air bombings A comparative study of injuries in survivors of open-air versus confined space explosions. Journal of Trauma - Injury, Infection and Critical Care, 41(6), 10301035.

[37] Li G.Y, He Q, Mangan R, Xu G, Mo C., Luo J, Destrade M, Cao Y. Guided waves in pre-stressed hyperelastic plates and tubes.

[38] Makoshi JA, Davinson J, Risling M, Eijima S, Ono K. Validation of Local Brain Kinematics of a Novel Rat Brain Finite Element Model under Rotational Acceleration. International Journal of Automotive Engineering 5 (2014) 31-37.

[39] Manley, G.T.,G.Rosenthal, M.Lam,D.Morabito,D.Yan,N.Derugin et al. 2006. Controlled cortical impact in swine: Pathophysiology and biomechanics. J Neurotrauma. 23:128-39.

[40] Mannan, S. (2005). Lees loss prevention in the process industries; Vol. 2: Hazard identification, assessment and control. Amsterdam, The Netherlands: Elsevier.

[41] Martin RH (2016) Soft targets are easy terror targets: Increased frequency of attacks, practical preparation, and prevention. Forensic Res Criminol Int J 3(2): 00087. DOI: 10.15406/frcij.2016.03.00087

[42] Mehdi S.C.; Shailesh G.; Linxia G.; and Namas C., Dynamic Response of Brain Subjected to Blast Loadings: Influence of Frequency Ranges (2011). Mechanical & Materials Engineering Faculty Publications. Paper 60. http://digitalcommons.unl.edu/mechengfacpub/60

[43] Melvin JW., 1970. Development of a Mechanical Model of the Human Head Determination of Tissue Properties and Synthetic Substitute Materials. 14th Stapp Car Crash Conf, Society of Automotive Engineers, SAE Paper No. 700903.

[44] Miller K, Joldes G, Lance D and Wittek A. Total Lagrangian explicit dynamics finite element algorithm for computing soft tissue deformation. Commun. Numer. Meth. Engng 2007; 23:121134. DOI: 10.1002/cnm.887

[45] Miller K, Joldes G, Wittek A. New Finite Element Algorithm for Surgical Simulation. Intelligent Systems for Medicine Laboratory

[46] Mihai LA, Chin L, Janmey PA, Goriely A. A comparison of hyperelastic constitutive models applicable to brain and fat tissues. J. R. Soc. Interface 12:20150486. http://dx.doi.org/10.1098/rsif.20150486

[47] Nakagawa, A., G.T. Manley, A.D. Gean, K. Ohtani, R. Armonda, A. Tsukamoto et al. 2011. Mechanisms of primary blast-induced traumatic brain injury: Insights from shock-wave research. J Neurotrauma. 28:110119.

[48] Ogden, R.W. 1972. Large deformation Isotropic Elasticity - On the correlation of theory and experiment for incompressible rubberlike solids. Proc. R. Soc. Lond. A, 326, 565-584

[49] Ogden R.W. Incremental statics and dynamics of pre-stressed elastic materials.

[50] Ogden R.W. Non-linear Elastic Deformations. Courier Corporation, 1997 - 532 pages. ISBN 0-486-69648-0

[51] Omens JH, Fung YC. Residual strain in rat left ventricle. Circ Res. 1990 Jan;66(1):37-45.

[52] zkaya N, Nordin M, Leger D. Fundamentals of Biomechanics: Equilibrium, Motion, and Deformation. Springer Science & Business Media, 1999 - 393 pginas.

[53] Patton, D.; Mcintosh, A. & Kleiven, S. The Biomechanical Determinants of Concussion: Finite Element Simulations to Investigate Tissue-Level Predictors of Injury During Sporting Impacts to the Unprotected Head Journal of applied biomechanics, 2015, 31, 264-268

[54] Pervin F, Chen W.W. Dynamic mechanical response of bovine gray matter and white matter brain tissues under compression. Journal of Biomechanics 42 (2009) 731735

[55] Povlishock, J.T. 2013. The window of risk in repeated head injury. J Neurotrauma. 30:1.

[56] Prange MT, Margulies SS. Regional, directional and age-dependentproperties of the brain undergoing large deformation. J. Biomech Eng Trans Asme,2002) 124(2):244-252. doi:10.1115/1. 1449907

[57] Prevost TP, Jin G, Moya MA, Alam HB, Suresh S., Socrate S. Dynamic mechanical response of brain tissue in indentation in vivo, in situ and in vitro. Acta Biomaterialista 7, 2011, 4090-4101

[58] Rashid B, Destrade M, Gilchrist M. Mechanical Characterisation of Brain Tissue in comparison at Dynamic Strain Rates.

[59] ROY A. Construction of a physics-based brain atlas and its applications. A phd thesis submitetted for the degree of doctor of philosophy.

[60] Rooij R, Kuhl E. Constitutive Modelling of Brain Tissue: Current Perspectives. Applied Mechanics Reviews, 2016, 010801-1

[61] Rooij R, Kuhl E. Constitutive Modeling of Brain Tissue: Current Perspectives.doi:10.1115/1.4032436

[62] Rubovitch, V., M. Ten-Bosch, O. Zohar, C.R. Harrison, C. TempelBrami, E. Stein et al. 2011. A mouse model of blast-induced mild traumatic brain injury. Exp Neurol. 232:2809.

[63] Saatman, K.E., A.C. Duhaime, R. Bullock, A.I. Maas, A. Valadka, and G.T. Manley. 2008. Classification of traumatic brain injury for targeted therapies. J Neurotrauma. 25:71938.

[64] Simo J.C. "On fully three-dimensional finite strain viscoelastic damage model: Formulation and computational aspects". Comput. Meth. In Appl. Mech. Eng.. Vol. 60. 153-173. 1987.

[65] Tse K.M., Lim S.P., Tan V.B.C., LeeH.P. A Review of Head Injury and Finite Element Head Models. American Journal of Engineering, Technology and Society. Vol. 1, No. 5, 2014, pp. 28-52.

[66] Weickenmeier J, Saez P, Butler C.A.M, Young P.G, Goriely A, Kuhl E. Bulging Brains. In book: Multiscale Soft Tissue Mechanics and Mechanobiology, pp.197-212. DOI: 10.1007/978-94-024-1220-8_10

[67] Wright RM, Ramesh KT. An axonal strain injury criterion for traumatic brain injury. Biomech Model Mechanobiol, 2012; 11:245-260.

[68] Wright RM, Post A, Hoshizaki B, Ramesh KT. A Multiscale Computational Approach to Estimating Axonal Damage under Inertial Loading of the Head. Journal of neurotrauma, 2013; 30:102-118.

[69] *https://biosphera.org/*"